Material Science and Technology Division

Propulsion Materials Program
Quarterly Progress Report for
April through June 2010

D. R. Johnson
Technical Project Manager

Prepared for
U.S. Department of Energy
Assistant Secretary for Energy Efficiency and Renewable Energy
Office of Vehicle Technologies Program
VT 05 04 000

Prepared by the
OAK RIDGE NATIONAL LABORATORY
Oak Ridge, Tennessee 37831-6066
Managed by
UT-Battelle, LLC
for the Department of Energy
Under contract DE-AC05-00OR22725

CONTENTS

Project 18516 – Materials for Electric and Hybrid Drive Systems

Agreement 16305 – Materials by Design – Solder Joints of High Performance Electronics **(ORNL)**

Agreement 16306 – Power Electronics Materials Compatibility **(ORNL)**

Agreement 16307 – Environmental Effects on Power Electronic Devices **(ORNL)**

Agreement 19201 – MBD Non-Rare Earth Magnetic Materials **(ORNL)**

Project 18517 – Combustion System Materials

Agreement 11752 – Materials for HCCI Engines **(ORNL)**

Project 18518 – Materials for High Efficiency Engines

Agreement 13329 – Mechanical Reliability of Piezo-Stack Actuators **(ORNL)**

Agreement 15050 – Evaluation of Materials via ACERT Engine **(ORNL)**

Agreement 16303 – Materials for High Pressure Fuel Injection Systems **(ORNL)**

Agreement 16304 – Materials for Advanced Engine Valve Train **(ORNL)**

Agreement 17257 – Materials for Advanced Turbocharger Design **(ORNL)**

Agreement 17894 – NDE for ACERT Engine Components **(Argonne)**

Agreement 18570 – Engine Materials Compatibility with Alternative Fuels **(ORNL)**

Agreement 18571 – Materials Issues Associated with EGR Systems **(ORNL)**

Agreement 19202 – Friction and Wear in Ti Components **(ORNL)**

Project 18519 – Materials for Exhaust and Energy Recovery

Agreement 10461 – Durability of Diesel Engine Particulate Filters **(ORNL)**

Agreement 10635 – Catalysts vs First Principles **(ORNL)**

Agreement 19214 – Impact of Biofuels on Diesel Particulate Filters **(ORNL)**

Agreement 20091 – Electrically Regenerated DPF Material **(ORNL)**

<u>Project 18865 – Materials by Design</u>

Agreement 9105 – Characterization of Catalyst Microstructures **(ORNL)**

Agreement 14957 – Thermoelectric Mechanical Reliability **(ORNL)**

Agreement 16308 – MBD - Thermoelectrics Theory and Structure **(ORNL)**

Agreement 17895 – Durability of ACERT Engine Components **(ORNL)**

Agreement 20370 – Life Cycle Modeling of Propulsion Materials **(ORNL)**

Agreement 16305: Materials by Design – Solder Joints of High Performance Power Electronics

G. Muralidharan, Ralph Dinwiddie, Andrew Kercher, and Burak Ozpineci
Oak Ridge National Laboratory

Objective/Scope

Advanced hybrid and electric propulsion systems are required to achieve the desired performance and life targets set for future automobiles. As specified in the OFCVT objectives, a target lifetime of 10-15 years has been projected for hybrid and electric propulsion systems meant for operation in harsh automotive environments. Power electronic components and systems are integral components of advanced automotive hybrid and electric propulsion systems. The trend in automotive power electronics is for using higher operating temperatures which has a detrimental effect on the stability of materials used in such systems. The objective of this task is to evaluate the effects of the higher temperatures on critical metallic materials that are used in power electronic devices and systems and to use the Materials-by-Design approach to identify appropriate combinations of materials that would decrease inopportune failures and maximum lifetime and reliability.

Based on the trend for using higher temperatures in power electronic components, there is a significant need to study failures of electronic packages induced by metallurgical changes of solder joints used as die attaches, and in wire bonds exposed to high temperatures (up to 200°C in contrast to the current 125-150°C exposure) anticipated in such applications. These failures can be induced in solder joints and other components by combination of temperatures, stresses, and current. Coarsening of solder joint microstructure along with the formation of intermetallic compounds takes place during high temperature exposure. Wire bonds are also known to be a key location of failures for packages meant for high temperature use. An understanding of the failures in solder joints and wire bonds will empower us to develop a computation-oriented method for the design of materials for packaging applications.

The approach used in this work would be to study failures in simple package designs so that the emphasis is on materials rather than package design thus avoiding complexities of package design issues that may overshadow materials issues. Packages will be subject to extremes of operational stress levels/temperature levels to the study the origin of failures. Steady-state exposure at high temperatures and cyclic exposures (thermal fatigue) all affect microstructure of the materials, their properties, and hence the failure of joints. X-ray radiography along with acoustic and infrared imaging (as is necessary) will be used to characterize voids present in the solder joints. Knowledge from the failures would enable the selection/development of more appropriate materials that would ensure required lifetimes of 10 to 15 years expected of modules in EVs and Hybrid systems.

Technical Highlights

As reported earlier, in collaboration with Powerex Inc., progress has been made in preparing Au-Sn and Sn-Ag solder joints for thermal cycling testing and high temperature exposure. Silicon dies measuring 2.5 mm x 2.5 mm were mounted on a

metallized AlN DBC substrate with the metallization consisting of a medium phosphorus (6-12%) nickel layer followed by a thin Au layer on the surface. To understand the initial void content in the solder joint, high resolution X-ray radiography was carried out on all the specimens.

Thermal cycling results showed that joints between Au-Sn and Si resulted in cracking of the silicon die during thermal cycling. Ag-Sn joints between silicon and DBC substrates have been tested to 3000 cycles. In this quarter, thermal cycling of Au-Sn joints between SiC and DBC substrates were continued. It was observed **that thermal cycling also resulted in cracking of the SiC dies**, although after a larger number of cycles when compared to the silicon dies.

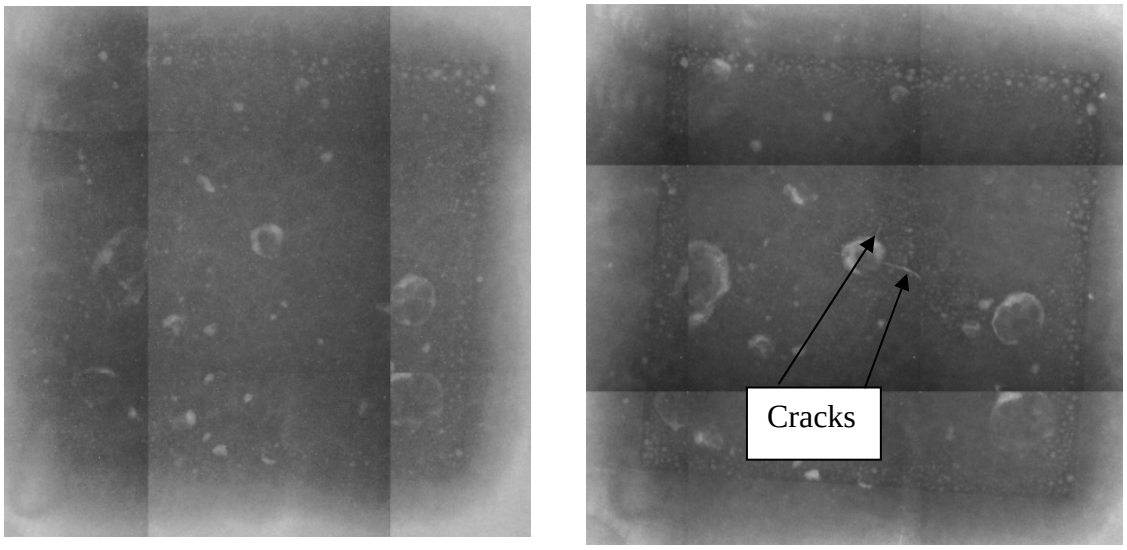

(a) (b)

Figure 1. Effect of thermal cycling on SiC dies bonded with Au-Sn solders. (a) 0 thermal cycles, and (b) 1820 cycles

Status of FY 2010 Milestones

Work is on schedule to meet the following milestone: Complete fabrication and evaluate reliability of sintered joint using one thermal cycling condition. **(9/2010)**

Communications/Visits/Travel

Communications are on-going with a vendor on the design and fabrication of a system for preparation of sintered joints

Problems Encountered

Design and fabrication of system to perform sintered solder joints was more complex than anticipated and has delayed the acquisition of the system.

Presentations/Publications/Awards

Presentation

G. Muralidharan, K. Kurumaddali, A. Kercher, and Scott Leslie, “Reliability of Sn-3.5 Ag solder joints in high temperature packaging applications,” Electronic Components and Technology Conference 2010, June 1- June 4, 2010, Paris Las Vegas, Las Vegas, NV

Publications

G. Muralidharan, K. Kurumaddali, A. Kercher, and Scott Leslie, “Reliability of Sn-3.5 Ag solder joints in high temperature packaging applications,” Proceedings of Electronic Components and Technology Conference 2010, pp. 1823-1829.

References

None

Agreement 16306: Materials Compatibility of Power Electronics

B. L. Armstrong, D. F. Wilson, C. W. Ayers, S. L. Campbell, and S. J. Pawel
Oak Ridge National Laboratory

Objective/Scope

The use of evaporative cooling for power electronics has grown significantly in recent years as power levels and related performance criteria have increased. As service temperature and pressure requirements are expanded, there is concern among the Original Equipment Manufacturers (OEMs) that the reliability of electrical devices will decrease due to degradation of the electronic materials that come in contact with the liquid refrigerants. Potential forms of degradation are expected to include corrosion of thin metallic conductors as well as physical/chemical deterioration of thin polymer materials and/or the interface properties at the junction between dissimilar materials in the assembled components. Initially, this project will develop the laboratory methodology to evaluate the degradation of power electronics materials by evaporative liquids.

Technical Highlights

During this quarter, work was performed on ribbon bonds. Due to the current limitation of the power system, ribbons were removed from the manufactured cards to allow for testing at the same current level used previously for the wire. Testing was performed at 39 amperes per ribbon with 2 seconds on and 2 seconds off cycle. Figure 1 shows that the microstructure of the as-received wire consisted of fine grains aligned along the length of the wire. In contrast, after cyclic testing, the microstructure displays grains of increasing size on moving from the bond region toward the crown of the ribbon. This behavior is very similar to that reported previously for circular cross-section wires. Cyclic pulsing of the ribbons and microstructural evaluation of cross sections are continuing.

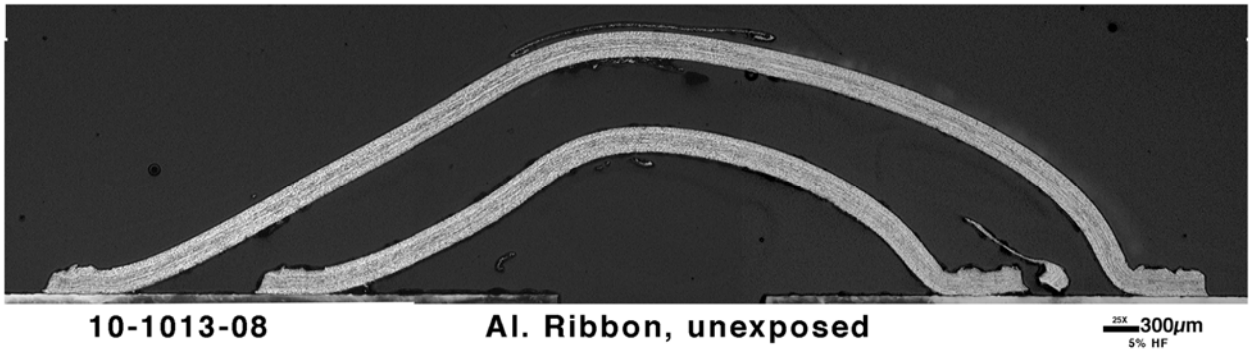

Figure 1. Cross-section of unexposed aluminum ribbon showing similar grain structure throughout its length.

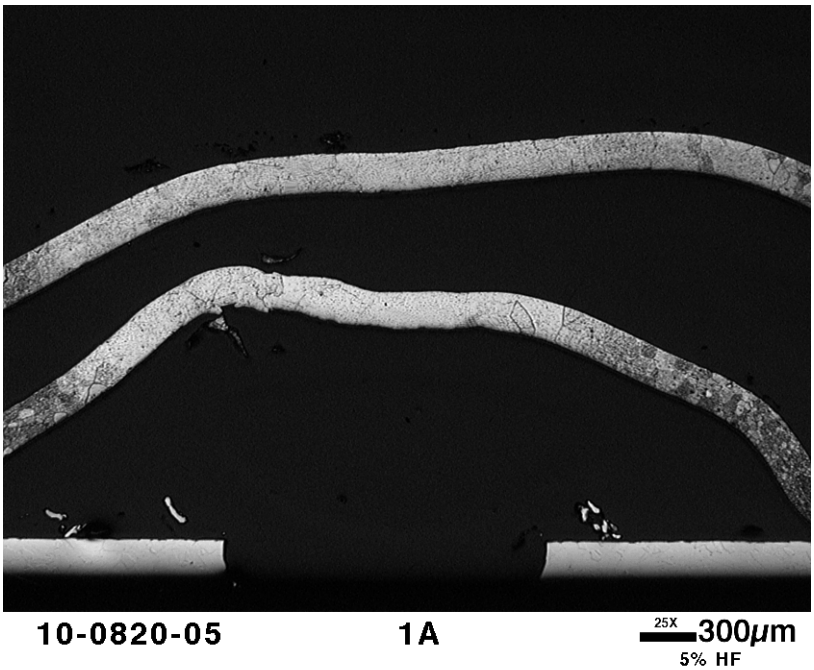

Figure 2. Cross-section of cycled aluminum ribbon showing increasing grain sizes from the bond end to the crown of the ribbon.

Results of the chemical analyses of the wires that were sent to an industrial laboratory were received. The data confirms the high purity of the aluminum wire. While there were ppm levels of various elements, none of these elements possess boiling points low enough to form gases at the test temperature. Hence, the possibility of pore formation at the crown due to gas formation is ruled out.

Status of FY 2010 Milestones

Validate the proposed methodology for examining the interaction of the electrical components with evaporative coolant. **(09/09)** On track.

Communications/Visits/Travel

A poster was presented and reviewed at the 210 Annual Merit Review & Peer Evaluation Meeting, June 7-11, 2010, in Washington, D.C.

Problems Encountered

None.

Publications/Presentations/Awards

None.

References

None to report.

Agreement 16307: Modeling/Testing of Environmental Effects on PE Devices

A. A. Wereszczak, P. J. Ritt, H.-T. Lin, and H. Wang
Oak Ridge National Laboratory

Objective/Scope

Understand the complex relationship between environment (temperature, humidity, and vibration) and the performance and reliability of the material constituents within automotive power electronic (PE) devices and in supportive systems. There is significant interest in developing more advanced PE devices (PED) and systems for transportation applications (e.g., hybrid electric vehicles, plug-in hybrids) that are capable of sustained operation to 200°C. Thermal transfer and expansion are two environmental aspects associated with temperature that can affect PED reliability. Advances in packaging materials and technology can achieve this but only after their service limitations are better understood via modeling and testing.

Technical Highlights

The primary effort this quarter involved the continuation of the examination of using the flash diffusivity method to determine thermal properties of multilaminate power electronic devices.

Direct copper bonded (DCB) ceramic substrates from Curamik are under evaluation. Apparent thermal diffusivity is studied as a function of copper cladding and the ceramic thicknesses. The ceramic was either aluminum oxide (Al_2O_3) or aluminum nitride (AlN). Six DBC substrates are considered and their basic characteristics are shown in Table. I.

Table I. Dimensions of evaluated DBCs.

DBC Ceramic	Manuf Reported Ceramic Thickness (in)	Manuf Reported Copper Thickness (in)	Manuf Reported Total Thickness (in)	Manuf Reported Ceramic Thickness (mm)	Manuf Reported Copper Thickness (mm)	Manuf Reported Total Thickness (mm)
Al_2O_3	0.015	0.008	0.031	0.38	0.20	0.79
Al_2O_3	0.040	0.008	0.056	1.02	0.20	1.42
Al_2O_3	0.040	0.012	0.064	1.02	0.30	1.63
AlN	0.025	0.008	0.041	0.64	0.20	1.04
AlN	0.025	0.012	0.049	0.64	0.30	1.24
AlN	0.040	0.012	0.064	1.02	0.30	1.63

Thermal diffusivity samples with a 12.7-mm diameter were core-drilled from each of the six substrates shown in Table 1. To counteract the reflective nature of the copper, a

graphite coating was applied to the underside of each sample, or the side that would be subjected to the xenon energy source. The graphite coating was a spray coating and applied in a fumigated hood. The six samples were loaded consecutively into a 24-capacity, aluminized sample holder from Anter. Three laser pulse shots were taken on each sample at 20 and 200°C. An illustration of the repeatability of the thermal diffusivity responses is shown in Fig. 1. Spring-loaded detector pins on the top of the sample determined the change in voltage through the sample during the shot. Once three shots have been fired on a sample, the sample holder rotated automatically to the next sample.

Thermal diffusivity differences were observed among the six DBCs. A comparison of the temperature transients for each at 20 and 200°C are shown in Figs. 2-3, respectively. The longer the time it takes to get to maximum temperature at 200°C will manifest itself in a lower thermal diffusivity.

The transient temperature data were analyzed using the classical Parker thermal diffusivity (α) equation

$$\alpha = \frac{0.1388 d^2}{t_{1/2}},$$

where d is the sample thickness, and $t_{1/2}$ is the one-half time for the sample to reach a maximum voltage after the laser shot. The average thermal diffusivities for each of the six DBCs are summarized in Table II. An increase in temperature from 20 to 200°C causes the thermal diffusivity in all to go down in temperature.

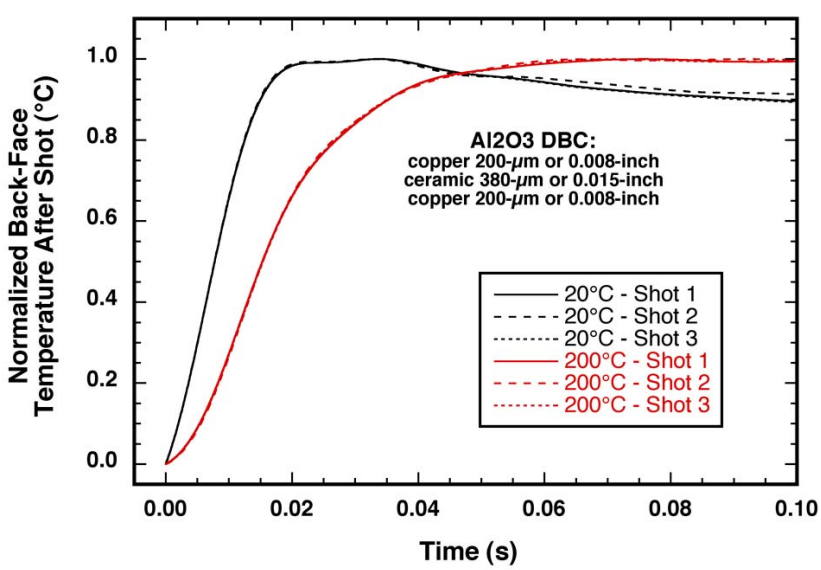

Figure 1. The thermal diffusivity responses in all six samples were repeatable. An example of this is shown for one of the six samples at 20 and 200°C.

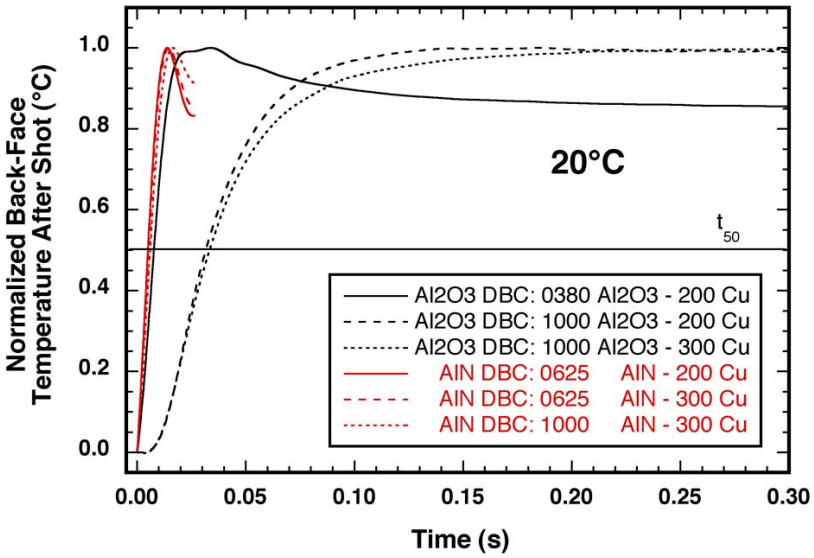

Figure 2. Thermal diffusivity response of DBCs at 20°C.

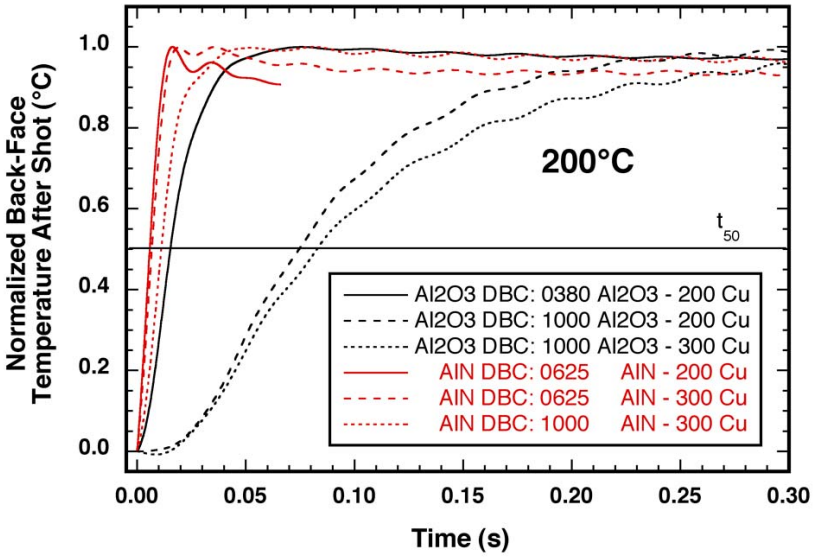

Figure 3. Thermal diffusivity response of DBCs at 200°C.

Table II. Dimensions of evaluated DBCs.

DBC Ceramic	Manuf Reported Ceramic Thickness (mm)	Manuf Reported Copper Thickness (mm)	Manuf Reported Total Thickness (mm)	Temperature (°C)	Measured Total Thickness (mm)	Thermal Diffusivity Average (cm^2/s)
Al_2O_3	0.38	0.20	0.79	20	0.779	0.1089
				200		0.0549
Al_2O_3	1.02	0.20	1.42	20	1.591	0.1113
				200		0.0469
Al_2O_3	1.02	0.30	1.63	20	1.551	0.0998
				200		0.0403
AlN	0.64	0.20	1.04	20	1.012	0.2843
				200		0.2442
AlN	0.64	0.30	1.24	20	1.209	0.3852
				200		0.2974
AlN	1.02	0.30	1.63	20	1.564	0.5680
				200		0.3050

These results are now being analyzed further through the use of an ANSYS transient thermal diffusivity finite element model. The thicknesses of the copper and ceramic layers will be considered and thermal transients will be predicted assuming there are no interfacial thermal losses. This will then be compared with the shown measured responses, and the contributing role of the interfaces on thermal diffusivity in these DBCs can then be interpreted.

Status of FY 2010 Milestones

Develop a test coupon, method, and model that will estimate and measure the apparent thermal diffusivity of a PED's die-solder-DBC laminate. (09/10) *On schedule.*

Communications/Visits/Travel

Wereszczak had numerous meetings with VT APEEM PIs L. Marlino, F. Wang, and Z. Liang to discuss collaborative efforts. Wereszczak traveled to Albuquerque to give a presentation at the IMAPS High Temperature Electronics conference in May.

Problems Encountered

None.

Publications/Presentations/Awards

A presentation and companion paper entitled "Edge-Controlled Mechanical Failure of Si and SiC Semiconductor Chips" co-authored by A. A. Wereszczak, O. M. Jadaan, and T. P. Kirkland was given at the IMAPS conference High Temperature Electronics (HiTEC 2010), May 11-13, 2010, Albuquerque, NM.

References

None.

Agreement 19201: Non-Rare Earth Magnetic Materials

Michael A. McGuire and David J. Singh
Oak Ridge National Laboratory

Objective/Scope

We will examine rare-earth-free chemical systems which hold promise for the discovery of new high-temperature ferromagnets with the large magnetic moments and strong anisotropies required for technologically useful permanent magnet materials. This research will focus on the development of new rare-earth free permanent magnet materials. Understudied chemical systems which are likely to contain materials with properties required for useful ferromagnets (large moments, high Curie temperatures, strong magnetic anisotropy) will be synthesized and characterized. First principle calculations will be performed to aid in the identification of promising target materials and to guide chemical tuning of magnetic properties through element substitutions and alloying. The focus will be on materials based on elements, such as Mn, Fe and Co, suitable for application in vehicles.

The primary challenge in this work is to obtain high magnetic anisotropy without rare-earth elements, while maintaining high saturation magnetization. The two main sources of anisotropy are magneto-crystalline anisotropy and shape anisotropy. Magneto-crystalline anisotropy is an intrinsic property determined by energy required to rotate a magnetic moment relative to the crystal lattice. Shape anisotropy is an extrinsic property related to the domain structure of individual crystallites. We are targeting new materials with large magneto-crystalline anisotropy, which could then be further enhanced by materials processing to optimize magnetic domain configurations.

Technical Highlights

In this Quarter, work focused primarily on the investigation of melt-spun M_2Co_{11}-based materials (M = Zr, Hf). We examined the effects three chemical manipulations in this system: (1) the addition of small amounts of B to the samples, (2) full replacement of Hf with Zr, and (3) partial replacement of Co with other transition metals (Fe and Mn). Samples were prepared by arcmelting and then melt-spinning using a 0.7mm orifice and a surface velocity of 16 m/s. Results are presented in the form of demagnetization curves in Figure 1, and summarized in the following.

(1) *Addition of boron to Hf_2Co_{11}*: A sample was prepared which contained several atomic percent of boron, with the nominal composition $Hf_2Co_{11}B$. The meltspun ribbon showed increased coercivity over that of Hf_2Co_{11}. The significant increase in the coercive field (~40 %) suggests that interstitial B may prove to play an important role in enhancing the permanent magnet properties of these materials. Little change in the remnant magnetization was observed upon B addition. However, due to the decreased “squareness” of the demagnetization curve compared to Hf2Co11, the maximum energy product $(BH)_{max}$ is essentially unchanged.

(2) *Zr substitution in $Hf_2Co_{11}B$*: Hf was replaced by Zr to obtain a sample with nominal composition $Zr_2Co_{11}B$. Magnetization measurements on the melt-spun ribbon show an enhanced remnant magnetization, as was expected from our earlier work on Zr_2Co_{11} and Hf_2Co_{11}. The coercive field is decreased, however, and the curve again lacks squareness, resulting in a degradation of the energy product. A mixture of Zr and Hf may prove to be best in this system.

(3) *Partial replacement of Co*: Cobalt was partially replaced by iron and manganese, giving nominal compositions $Hf_2Co_{10}Fe$ and $Hf_2Co_{10}Mn$. This proved to have a surprisingly strong and detrimental effect on the demagnetization behavior. Both the remnant magnetization and the coercive field were significantly reduced. Understanding these effects will require electron microscopy to determine how chemical phases and crystallite morphologies are affected.

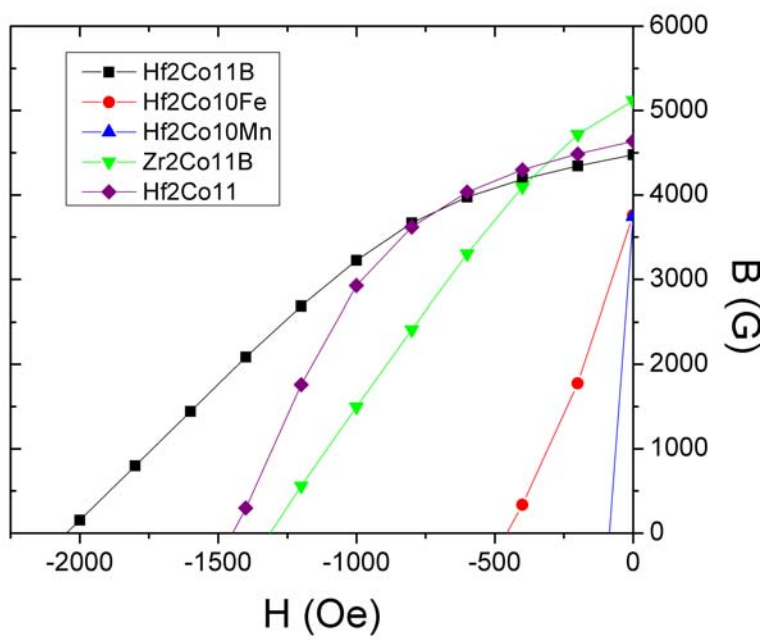

Figure 1. Demagnetization curves for meltspun Hf_2Co_{11} based materials. The measurements were taken with the applied field along the long direction of the melt-spun ribbons.

Other work has involved the investigation of the Hf-Mn system, where ferromagnetism is expected near the stoichiometric compound $HfMn_2$. Several samples near this composition have been synthesized. Vaporization of Mn results in a deviation of final stoichiometry from that targeted. However, a single phase $HfMn_2$ sample was obtained from a starting composition near $HfMn_{2.6}$. Magnetization measurements suggest that this compound is ferromagnetic, but with a very low Curie temperature (~5 K).

Status of FY 2010 Milestones
We are progressing toward our milestone of discovering new ferromagnetic materials that do not contain rare-earth elements.

Communications/Visits/Travel
April 27, 2010. An overview of this project was presented to representatives from GE Global Research, including Krishan Luthra, manager of all Global Research materials work, during a visit to ORNL.

Problems Encountered
No significant problems have been encountered.

Publications/Presentations/Awards
None to report for this quarter.

References
None

Agreement 11752: Advanced Materials Development through Computational Design for HCCI Engine Applications

Govindarajan Muralidharan, Rick Battiste, and Bruce G. Bunting
Oak Ridge National Laboratory

Objectives/Scope

To identify and catalog the materials operating conditions in the HCCI engines and utilize computational design concepts to develop advanced materials for such applications.

Highlights

Technical Progress

Materials-by-Design of Advanced Materials:

In this quarter, work was continued on Ni-based alloys for valve applications. As reported earlier, using thermodynamic modeling, microstructure evaluation, and mechanical property evaluation, high temperature fatigue was identified as a property of critical interest in Ni-based alloy valve materials for the next generation automotive engines. In order to develop relationships between the microstructures of the alloys and their mechanical properties, high-temperature fatigue property data were obtained on all down-selected alloys as a part of the project. Using the approximate correlation between the fatigue lives obtained using the rotating beam and fully reversed fatigue testing techniques several alloys with required microstructures have been identified as candidates for high temperature valve applications.

Using the microstructures of these alloys as a guide, computational thermodynamics was used to identify additional alloys with microstructure similar to the commercial alloys with desirable properties. In contrast to the commercially available alloys with Ni-contents in the range of 50 wt. % to 60 wt. %, the Ni-content in these alloys ranges from about 30 wt. % to 45 wt. % with the potential to achieve comparable properties. This implies that the alloys will be of lower cost but comparable mechanical properties.

Based upon the alloys developed last quarter, one alloy has been down-selected and prepared in the form of a large plate. Rotating beam specimens and fatigue specimens have been machined and heat-treatment has been completed. Figure 1 shows the large plate that was prepared for the purpose of fatigue testing.

Figure 1. A large plate of downselected alloy that was cast and thermomechanically processed for preparation of fatigue specimens.

In this quarter, a publication entitled, “Effect of Microstructure on the High Temperature Fatigue Properties of Two Ni-based Superalloys,” was completed and was submitted for publication in the proceedings of 7th International Symposium on Superalloy 718 & Derivatives to be held in Pittsburgh, PA, October 10-13, 2010. It was reported in this publication that the high temperature, high cycle fatigue properties of two nickel based alloys, Waspaloy and alloy 751, followed their high temperature tensile strengths. This paper has been accepted for publication after review.

Milestones

The following milestone has been completed: Complete selection of one commercial alloy and one newly developed alloy for high temperature valve application. **(9/2010)**

Agreement 13329: Design Optimization of Piezoceramic Multilayer Actuators for Heavy Duty Diesel Engine Fuel Injectors

H.-T. Lin, H. Wang, T. Matsunaga, A. Mottern, and A. A. Wereszczak
Oak Ridge National Laboratory

J. Carmona-Valdes and R. Stafford
Cummins Inc.

Objective/Scope

Enable confident utilization of piezo stack actuator in fuel injectors for heavy vehicle diesel engines. The use of such actuators in diesel fuel injectors has the potential to reduce injector response time, provide greater precision and control of the fuel injection event, and lessen energy consumption. Though piezoelectric function is the obvious primary function of lead zirconate titanate (PZT) ceramic stacks for fuel injectors, their mechanical reliability can be a performance and life limiter because PZT is brittle, lacks high strength, and is susceptible to fatigue. However, that brittleness, relatively low strength, and fatigue susceptibility can be overcome with the use of appropriate probabilistic design methods.

Technical Highlights

1. Mechanical Test and Characterization on EPCOS Stacks

Figure 1 is the part of the cross section of an EPCOS stack that has been fatigued to 10^8 cycles under the corresponding mechanical preload of 17 MPa. At the end of cycling, it has been observed that both the mechanical strain and charge density at the measurement field level (2 kV/mm) decreased 10-20%. The damage across the section is quite visible and involves the fracture of PZT layers, delamination of interfaces between the PZT and internal electrode and bonding layer. This kind of damage is partly responsible for the induced degradation of PZT stack's performance, and has the potential to result in the catastrophe failure.[1] Flexure testing has been proven to be an effective approach to evaluating the response of components of interest that includes biaxial flexure of plate specimen and four-point bend bar. They are designed to reveal the properties of PZT layer and interface, respectively.

However, the access to single-layer PZT plates has not been shown to be easy at this moment. Multilayer PZT plates were thus used in this project as an alternative [Fig. 2 (a)]. Stacks of ANOX8500b were used. Each stack had dimensions of 6.8 mm x 6.8 mm x 30 mm and consisted of a specified number of multilayer plates or actuators (MLAs). Each plate was sized 6.8 mm x 6.8 mm x 0.76 mm and further consisted of 10 PZT layers each 80 μm thick. These plates were obtained through chemically dissolving plate-to-plate bonding layers of stacks using a chemical solution (DYNASOL 750,

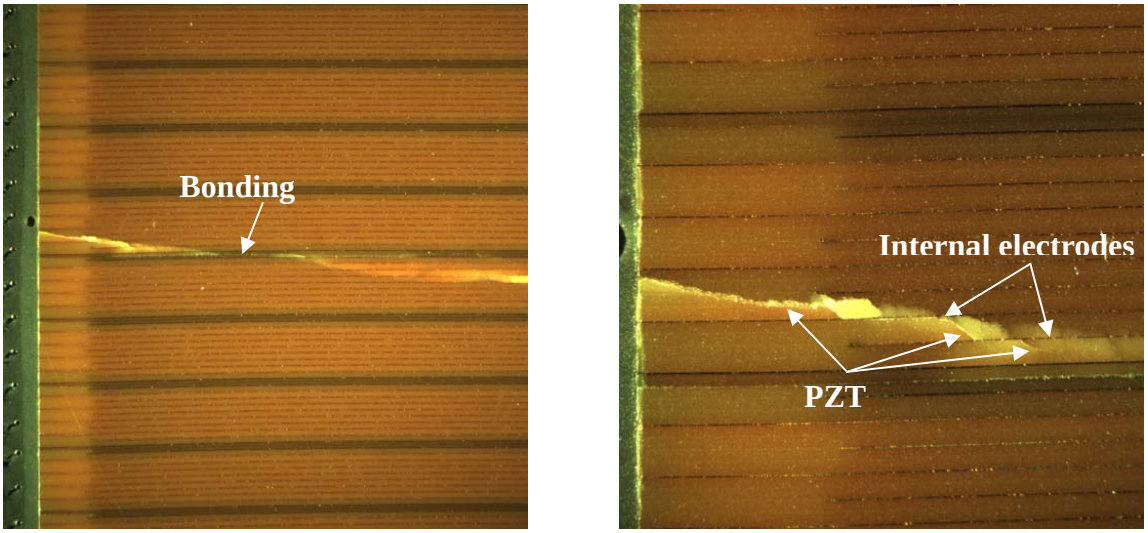

(a) (b)

Fig. 1. (a) An extended fracture developed in a fatigued PZT stack No 5 to 10^8 cycles and (b) enlarged area showing PZT layers, internal electrodes, bonding layer involved with the fracture.

Dynaloy, Indianapolis, IN) heated at 130°C. Because the Curie temperature of PZT-5*A* is around 350°C, the heating process is not considered to introduce any significant effect on the performance of PZT material. Also, the representativeness of PZT is not believed to be sacrificed by using a multilayer plate as it approaches more the working condition of PZT.

Bar specimens [Fig. 2 (b)] were prepared by splitting longitudinally a supplied PZT stack (ANOX8500b, uncapsulated) into four slender bars. A thin diamond blade (150 μm thick, Saint-Gobain, Worcester, MA) was modified and used to slice the stack at first. The obtained bars were then ground to remove influencing zones and reach the required surface finish as regulated by ASTM standards C1161 and C1495. A 45° chamfer was also made around all corners of cross section.

Mechanical Strength of Multilayer Plates: Parent stacks for obtaining individual multilayer plates were from the stacks that had been tested in previous stage of the project. All the stacks were dielectrically broken down during these tests. Table 1 lists the breakdown conditions. It is worthwhile noting that stack No 1 experienced more cycling than other two during the trial and error tests.

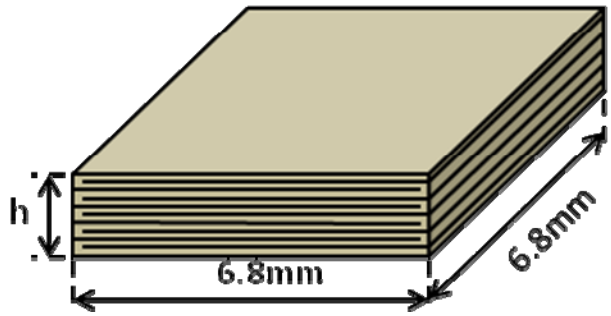

(a)

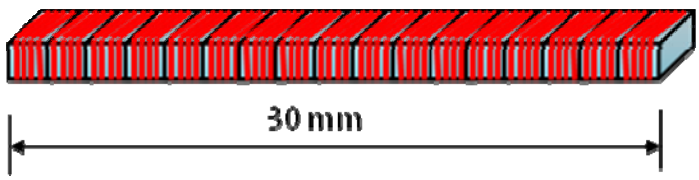

(b)

Fig. 2. Two geometries of specimens were studied: (a) multilayer plate and (b) stack bar

Table 1. Dielectric breakdown conditions of EPCOS PZT stacks (AN0X-8500b)

No	Size (mm^3)	C (μF)	Mechanical Load (N)	Electric Load (Vp, Hz)	Note
1	6.5x6.8x30	2.9	16	480, 20	2008 Purchase
2	6.5x6.8x30	2.9	16	400, 40	2008 Purchase
3	6.5x6.8x30	2.9	766	400, 40	2008 Purchase

Ball-on-ring (BoR) set up was used in testing and evaluation. A part of plates from stack No 1 were test in room temperature using 6.35 mm diameter Si_3N_4 ball and 5.12 mm diameter polymer ring. This was conducted in a house-built indentation system with the high precision alignment control in a displacement control mode, 0.01 mm/s. A 100-lb load cell was used for measuring the mechanical force during the test.

Tests under high temperature were carried out on INSTRON universal testing machine (Norwood, MA). A self-alignment fixture was modified for the ball-on-ring loading and this was achieved by using an alumina double-tube structure. A protruded inner tube served as the support ring. The end of the tube was carefully machined to provide the required

contact curve, and the obtained ring was sized with 4.88 mm diameter. A 12.7 mm diameter alumina sphere was used as loading ball. The temperature environment was provided by INSTRON furnace SFL. The controller can ramp the temperature to 200°C in 10 minutes. For stabilization of system, a 20 minute soak-time was generally provided before the mechanical loading. The cross-head rate was set at 0.6 mm/min or 0.01 mm/s, and1 kN load cell was used. The load cell channel was monitored during the heating process to avoid any unnecessary preload due to the thermal expansion of system.

Fifteen of multilayer plates from stack No 1 were tested in RT (room temperature) BoR with polymer support ring, nine in RT BoR with alumina ring, and three in 200°C with alumina ring. As shown in Fig. 3 (a), results are comparable in the case of RT for both support rings. Therefore, given the parent stack from which plates were extracted, flexure strengths obtained with polymer and alumina support rings were statistically comparable. The double-tube structure has been demonstrated to be robust and its protruded edge provides an effective approaching to simulating the required support ring. It is interesting to see that the multilayer plates exhibited a quasi-plastic deformation in the case of alumina support ring. Specifically, their loading curves were mostly with a yielding point and some of them had a strain hardening. This yielding was pronounced also at 200°C. This quasi-plasticity is related perhaps to the contact condition because that was not observed in loading curves with polymer supporting ring. However, the failure load can be identified by the yielding point from loading curves.

Plates from stacks No.2 and 3 were tested in three temperature conditions: RT (22°C), 100, and 200°C. Each included twenty-two specimens. It was observed that mechanical strength of plates decreased with increasing temperature within the tested range as shown in Fig. 3 (b). A comparison of RT results from stack No 1 and No 2 and 3 indicated that the flexure strength was related to the degree of damage of parent stacks introduced by pre-fatigue tests. It is realized that the effect of transverse shear was not considered in estimating the flexure strength. At the same time, the current preformed surface of support ring has a narrow flat due to the limit of machining that needs to be smoothed in future.

The failure origin was observed to be closely related to the outer PZT half-layer and outmost internal electrode. On failure origin was shown in Fig. 4.

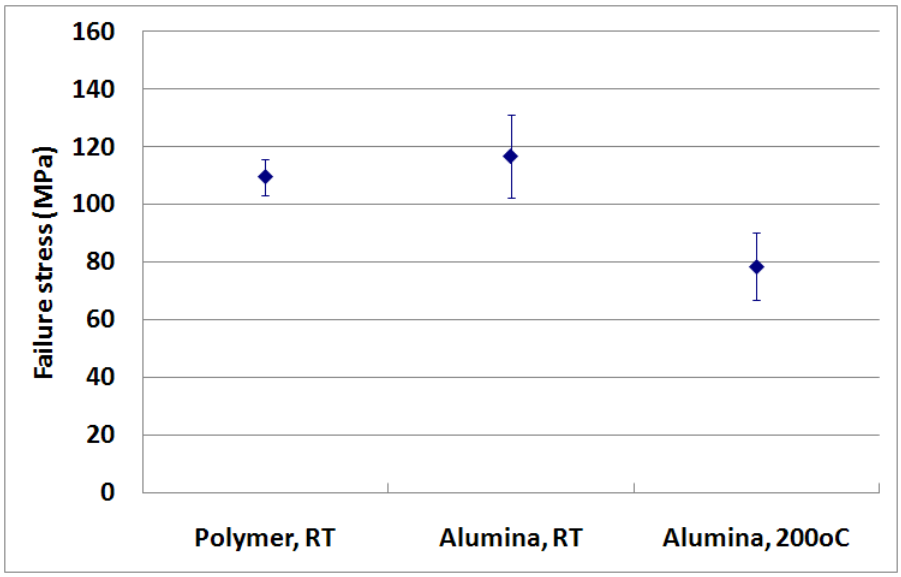

(a)

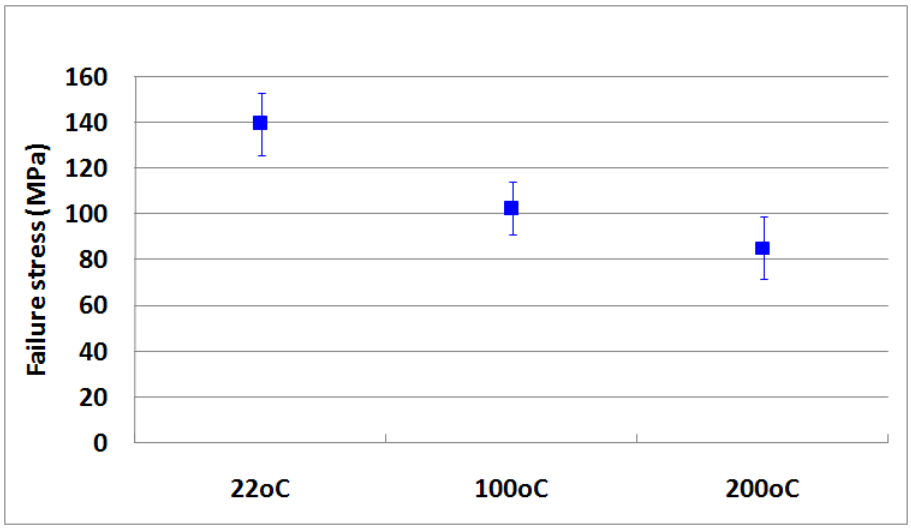

(b)

Fig. 3. (a) Flexure strength of multilayer plates from stack No 1, and (b) flexure strength of plates from stacks No 2 and 3.

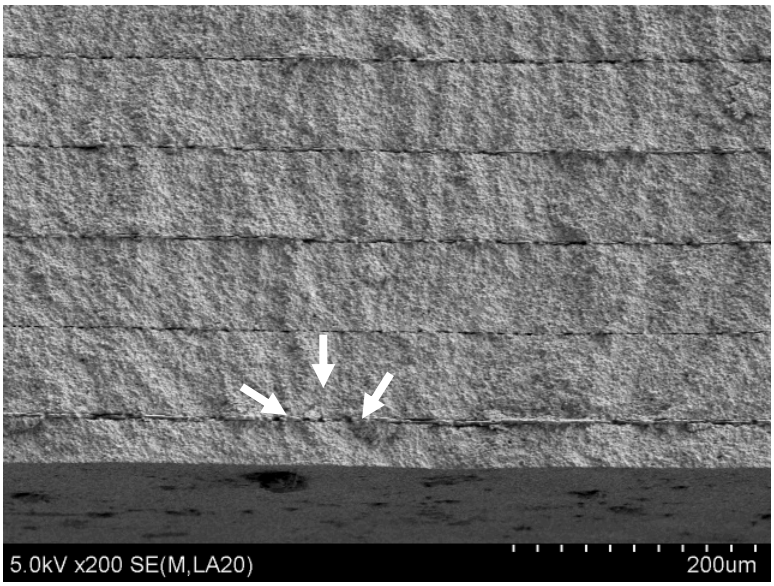

Fig. 4. SEM micrograph showing the fracture surface of a failed multilayer plate where the failure origin is marked.

Mechanical Strength of Stack Bars: Eight bars were prepared from two supplied stacks. A semi-articulated four-point bend setup was used with 6.35 mm inner and 25.4 mm outer supporting span. Tests were conducted in the house-built indentation system in a displacement rate of 0.001 mm/s. The lowered rate was used in order to catch the required data point as the available sampling rate was limited within 10Hz. A 100-lb load cell was used in monitoring and measuring mechanical loads.

Six bars generated meaningful data and the results are given in Table 2 along with those from a separate purchase in 2006. Specimens from 2008 purchase apparently had a higher flexure strength than 2006 purchase, and also higher than entire stacks.[2] This could be attributed to the specimen size effect involved with this process.

Table 2. Stacks of 08 Purchase Were Tested and Compared to 06 Purchase

	Dimensions (mm^3)	Quantity	Mean of strength (MPa)	Std dev of strength (MPa)
ECPOS08	30 x 7 x 3.2	6	35.04	1.55
EPCOS06	30 x 3 x 2.5	2	22.10	-

Failure of stack bars mostly occurred across the plate-to-bonding-layer interface as a result of delamination as shown in Fig. 5. This is confirmed as the half PZT layer is very obvious that is the bottom of the plate. No failure origin can be identified because there was no fracture ledge on the failed surface. A part of half PZT layer was peeled off

around the right corner but not entirely detached and cannot be identified as the failure origin. On the other hand, PZT-layer-to-internal electrode interface had a higher mechanical strength since no delamination was observed there.

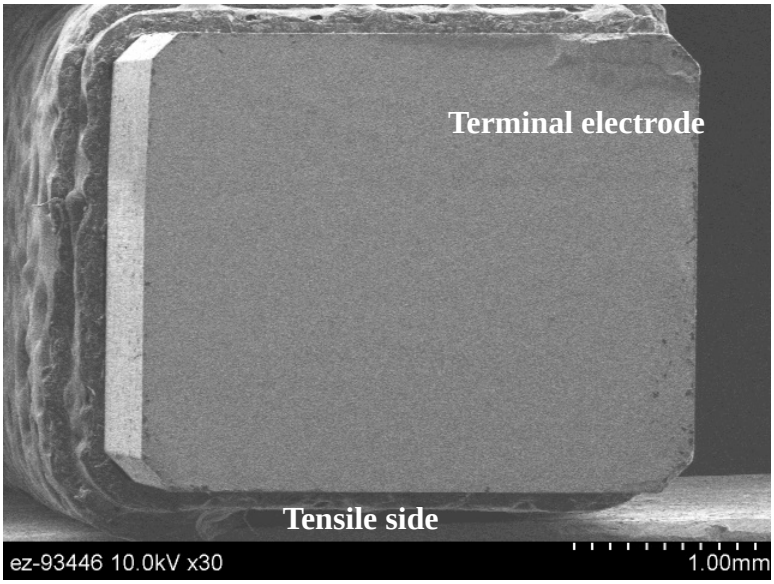

(a)

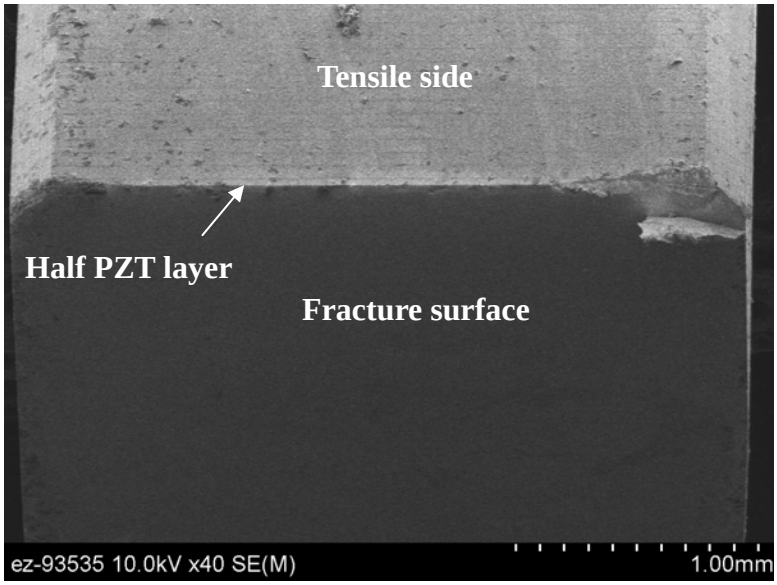

(b)

Fig. 5. Fracture Surface of a bar Specimen (a) fracture surface, and (b) side view of bar.

2. KCI Piezoceramic Test and Characterization

Understanding of fatigue and breakdown mechanisms of PZT materials can help diagnose the cause of stack failure in field test. In the previous stage of the project, the electric fatigue in bipolar loading of KCI single layer plate was studied experimentally using ORNL piezodilatometer. It has been shown that 1) tested PZT exhibited a significant reduction in unipolar measurement especially in the charge density, piezoelectric, and dielectric hysteresis, 2) in the bipolar measurement, drastic changes occurred in two wings of S(E) butterfly curve, 3) as for the D(E), the coercive field appeared to be decreased, but the remanant polarization did not, and 4) both the asymmetry of S(E) and the bias field of D(E) exhibited an noticeable change during the cyclic process. SEM studies revealed volume pores, grain, and domain structures on the polished and etched cross sections of the fatigued specimens and reference specimens. No significant difference in microstructures was observed between the fatigued and reference specimens (such as etch grooves previously observed in bipolar fatigued specimens). It is believed that involved fatigue mechanisms might not have developed to an extent that can be detected by the conventional microscopic analysis method, and a much more advanced approach such as scanning probe microscopy is demanded. Similar work was carried out for the bipolar cyclic fatigue in this quarter.

Bipolar Electric Cyclic Fatigue of PZT Single-Layer Plates: Bipolar cycling was conducted using 1.05/-1.05 kV/mm sine wave at 200 Hz. The cycling level corresponded to the coercive field of the material. Both unipolar and bipolar measurements were performed in the same way as done in unipolar electric cyclic fatigue.

Results showed that amplitudes of S(E) and D(E) didn't exhibit any defined trend in unipolar measurement perhaps due to the stabilized domain structure. On the other hand, bipolar measurement revealed consistent trend in S(E) and D(E). Specifically the S(E) exhibited a decreased size (ΔS_1 and ΔS_2) in both wings. The results for one pair of specimens are given in Fig. 6.

Although both wings of S(E) curve (butterfly) decreased due to the cycling, but the right wing decreased more than the left. This was also observed for PIC 151 in bipolar cycling.[3] In fact, the decrease in both wing sizes is different from various changes in unipolar cycling of this KCI PZT. In the latter, the right wing increased and the left decreased. Changes of wing sizes and piezoelectric hysteresis were not found to be symmetric as observed in the variation of asymmetry quantities (not shown). This asymmetry may be attributed to the remaining influence of the first poling and the offset polarization arising from the cycling.

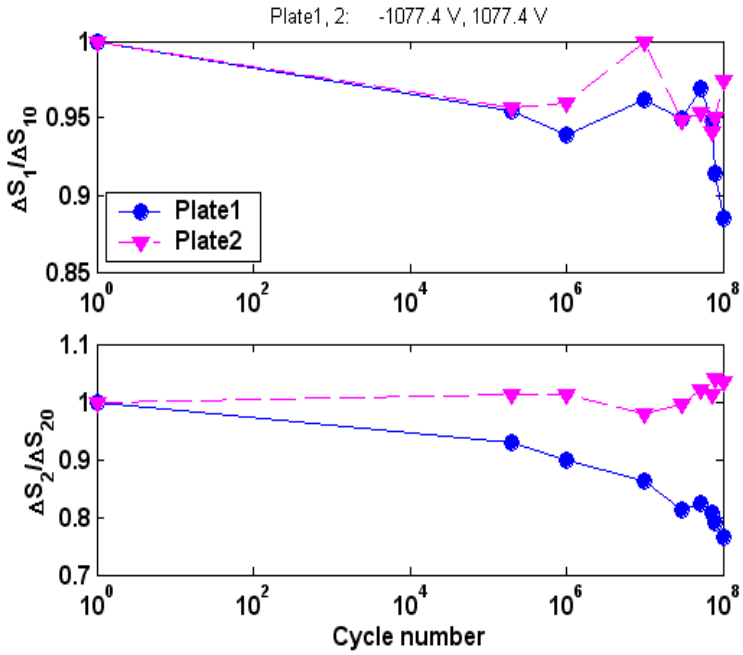

(a)

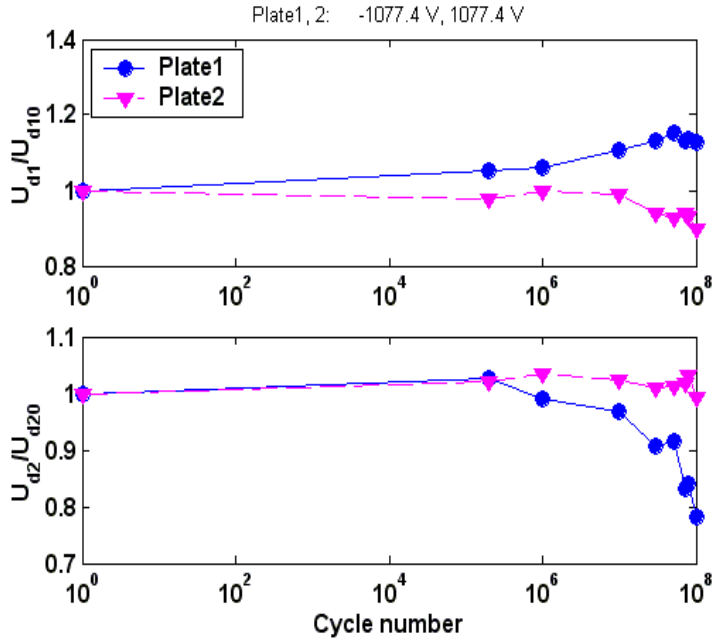

(b)

Fig. 6 Variations of (a) S(E) wing sizes as a function of cycle numbers, and (b) hysteresis obtain by bipolar measurement.

Loss of switchable polarization (P_r) amounted to 13%, whilst coercive field fluctuated and didn't exhibit any trend as shown in Fig. 7. The absence of increase in coercive field (E_c) may be related to the definition used in the data process. Nevertheless, bias field (E_{bias}) was accumulated additional 2% as a result of cycling (not shown). The fatigue of the PZT was, therefore, appreciable even in the cycling field of coercive level.

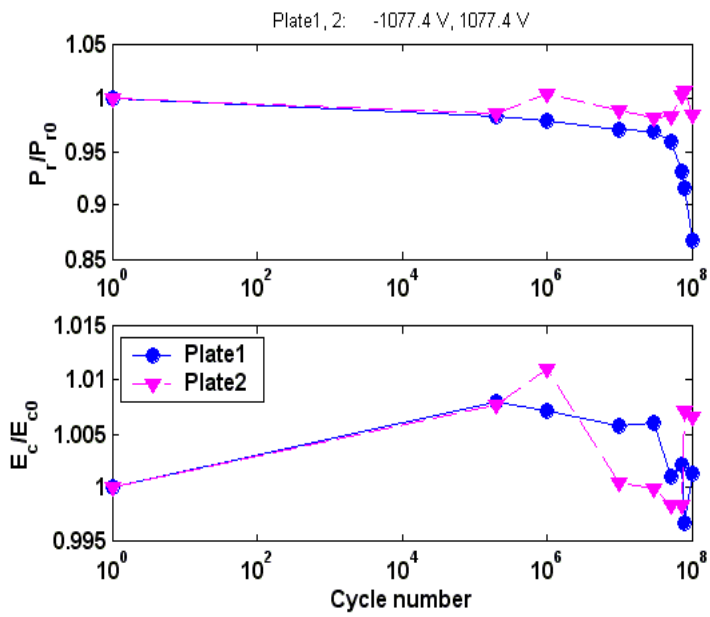

Fig. 7. Variations of switchable polarization and coercive field as a function of cycle number obtained by bipolar measurement.

Status of FY 2010 Milestones

Measure and compare reliability of competing commercially available piezoactuators under consideration for use in diesel fuel injectors, *on schedule*.

Communications/Visits/Travel

Conference call on CRADA update with Cummins, Inc. was held on June 28, 2010.

Publications/Presentations/Awards

1. Wang, H., Matsunaga, T. and Lin, H.-T., Characterization of poled single-layer PZT for piezo stack in fuel injection system, *34th Int. Conf. on Adv. Ceramics and Composites*, Jan. 24-29, 2010, Daytona Beach, FL, in print.
2. Wang, H., Cooper, T. A., Lin, H.-T., and Wereszczak, A. A., Fatigue responses of PZT stacks under semi-bipolar electric cycling with mechanical preload, *J. Appl. Phys.*, 2010, accepted.
3. Wang, H., Lin, H.-T., and Wereszczak, A. A., Strength properties of poled PZT subjected to biaxial flexural loading in high electric field, *J. Am. Ceram. Soc.*, 2010, in print.

4. Wang, H., Matsunaga, T., and Lin, H.-T., Effects of temperature and electric field on mechanical strength of single-layer PZT plate, in preparation.

References

1. B. Zickgraf, G. A. Schneider, and F. Aldinger, “Fatigue behavior of multilayer piezoelectric actuators,” *Proc. ISAF 1994*, University Park, PA, 325-328, 1995.
2. P. Supancic, Z. Wang, W. Harrer, Reichmann, and R. Danzer, “Strength and fractography of piezoceramic multilayer stacks,” *Key Eng. Mater.* 290, 46–53, 2005.
3. N. Balke, H. Kungl, T. Granzow, D.C. Lupascu, M. Hoffmann, and J. Rödel, “Bipolar fatigue caused by field screening in $Pb(Zr,Ti)O_3$ ceramics” *J. Am. Ceram. Soc.* 90, 1088, 2007.

Agreement 15050: Evaluation of Materials via ACERT Engine

Michael Kass, Brian Kaul, Norberto Domingo, Robert M. Wagner,
K. Dean Edwards, H. T. Lin, and D. Ray Johnson
Oak Ridge National Laboratory

Objective/Scope

This project is focused on improving the performance, emissions and efficiency of heavy-duty diesel engines through the application of materials enabled technologies. The range of material systems is comprehensive and includes 1) improved structural materials to accommodate higher cylinder pressures and temperatures, 2) improved durability and corrosion resistance, 3) low inertial components to improve transient response, 4) improved emissions aftertreatment performance, and 5) waste heat recovery systems.

To date a dynamometer engine research cell was constructed for use with heavy-duty engines. A 2004 C15 ACERT Caterpillar engine was provided by the Caterpillar materials research staff for materials-based efficiency evaluations. The engine was instrumented for combustion and thermal assessment. During FY09, the Caterpillar combustion research staff signed a WFO agreement with ORNL to evaluate a thermodynamic model used to assess efficiency improvements on the C-15ACERT engine.

Progress This Quarter (April – June 2010)

- We evaluated a novel turbine system, as part of a WFO agreement with Caterpillar, to improve the engine of a heavy-duty diesel engine. A prototype mixed-flow turbine (along with a standard geometry turbine) was sent to ORNL for engine evaluation. A photo of the two turbines is shown in Figure 1.

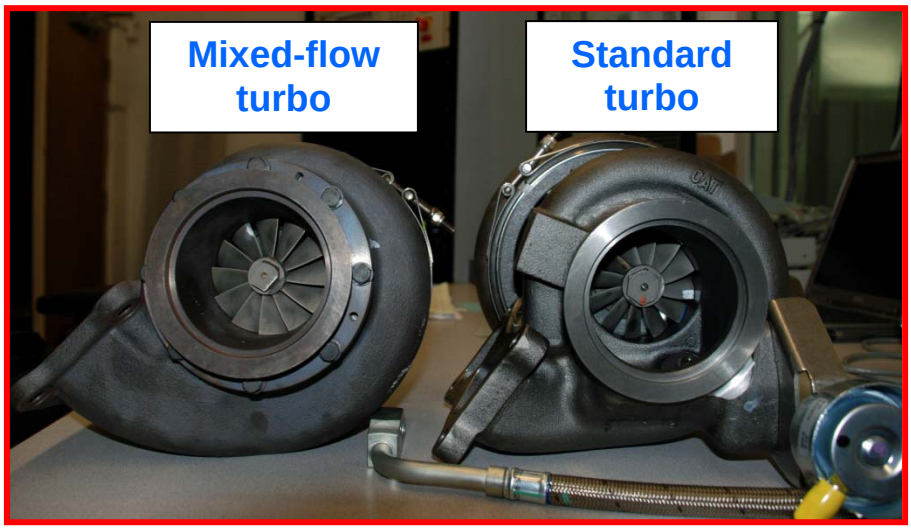

Figure 1. Photograph showing mixed-flow and baseline turbines.

- The housings for the new turbines would mate correctly with the existing engine hardware so a new compressor was fitted to the C-15 ACERT engine to enable proper alignment of the baseline and mixed flow turbine housings. The engine was operated under the conditions shown in Table 1 to effectively assess turbine performance.

Table 1. Engine Operating Conditions for Turbo Evaluation

Condition	Engine Speed (RPM)	% of Maximum Load
1	1200	100
2	1200	75
3	1200	50
4	1200	25
5	1500	100
6	1500	75
7	1500	50
8	1500	25
9	1800	75
10	1800	50
11	1800	25

The thermal efficiency and Brake Specific Fuel Consumption (BSFC) results for the baseline and mixed-flow turbines are shown in Figure 2 for each operating point. For every test condition, except #12, the thermal efficiency was observed to increase slightly when using the mixed-flow turbine. The efficiency improvement is also reflected by the decreased BSFC values for the mixed-flow turbine design. Although the efficiency improvements appear to be marginal, they are significant, and do advance the development of high-efficiency heavy duty diesel engines.

The WFO was completed on schedule and within budget. Caterpillar was extremely pleased with the results and, based on the success of this effort, nixed flow turbines are being considered for further engine designs.

- The next phase of experiments will focus on engine evaluations of new valve and exhaust manifold materials. Discussions are currently being held with Caterpillar to define an experimental matrix and schedule for valve experimentation to be performed during the next quarterly period. Caterpillar has also expressed a desire for ORNL to receive an advanced Tier IV engine for further efficiency experiments, which will be critical for FY 2011 activities.

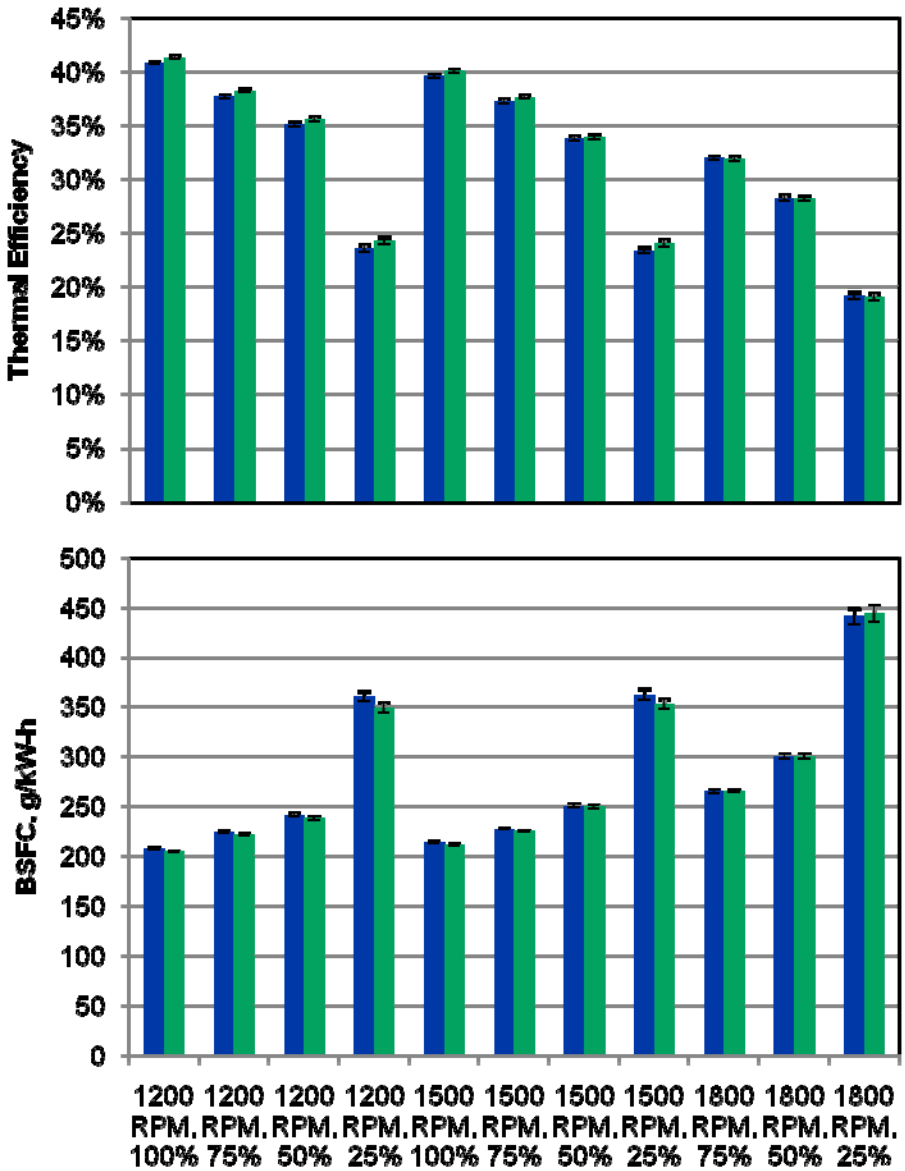

Figure 2. BSFC and Thermal Efficiency Comparison Data for the Baseline and Mixed-Flow Turbine.

Publications/Presentations/Awards

Materials-enabled High-efficiency Diesel Engines, Presented by Mike Kass during the 2010 DOE Hydrogen Program and Vehicle Technologies Annual Merit Review, June 10, 2010.

Plans for Next Reporting Period

- Complete engine evaluation for novel valve materials.

Agreement 16303: Materials for High Pressure Fuel Injection Systems

Peter J. Blau, Amit Shyam
Oak Ridge National Laboratory

Michael J. Pollard
Caterpillar Corporation

Objective/Scope

The objective of this Cooperative Research and Development Agreement (CRADA) between UT-Battelle, LLC and Caterpillar Corporation is to advance the state of the art in the characterization, selection, and use of metallic alloys for high-pressure diesel engine fuel injector nozzles.

During recent decades, fuel efficient, low-emissions diesel engine designs for heavy trucks have relied upon increasing fuel injection pressures to optimize combustion characteristics. Precise fuel metering is required. This key functional requirement has raised concerns over the ability of spray holes to be machined to sufficiently close tolerances to provide desired spray patterns and for the materials of construction to withstand hundreds of millions of high-pressure pulses without succumbing to fatigue damage. The data and analyses obtained in the course of this three-year effort are expected to provide vital information for designers and material selectors for high-performance fuel systems for energy-efficient diesel engines.

A three-pronged approach has been developed. It involves: (1) characterization of current fuel injector hole geometry and alloy metallurgy, (2) measuring the residual stress in nozzle tips near spray holes, and (3) development and use of specialized fatigue test methods to address the special requirements of the next generation of high-pressure fuel injectors.

Technical Highlights

Fatigue testing, with and without simulated flaws. Work continues to establish the method to prepare small notches (approximately 200-300 μm wide and similar in depth) in fatigue test specimens using electro-discharge machining (EDM). This is being done to study the effects of notches (holes) on the fatigue life of non-heat-treated and heat-treated alloy steels used in fuel injectors. The axial fatigue specimens contain an hour-glass shaped gauge section that is polished flat on opposing sides. The notch is in the middle of one of the two polished portions. During testing, it will face in the direction of the Questar optical imaging system. Previously reported experiments characterized the fatigue life versus applied stress of notch-free (smooth) specimens and established that they possess a transitional behavior based on whether cracks initiated in the bulk or on surface features. The net effect was to produce an offset in the log-log plots of fatigue life versus stress at high stresses (above about 900 MPa) from the portion of the the curve at lower stresses, where bulk flaws control initiation.

Figure 1 shows an EDM notch in the center of the polished flat gauge section of an axial fatigue specimen. Figure 2 shows a fatigue fracture that was initiated in a specimen containing such a notch. The radial propagation of the crack front is clearly seen in

Figure 2. Initial tests on non-heat-treated specimens with notches, produced failures at less than 20 cycles of fatigue loading. The heat-treated specimens, to be tested subsequently, are expected to last orders of magnitude longer.

Crack growth imaging. Computer control problems for the translation stage of the newly-installed Questar™ long distance-microscope system have now been resolved. The documentation of crack movements during fatigue tests will provide new insights on flaw propagation mechanics in current and candidate steels for high pressure fuel injectors.

Residual stress studies. Because residual stress can affect mechanical properties, like fatigue crack initiation and propagation, studies of the effects of aging on residual stress were conducted at Caterpillar Tech Center. Figure 3 compares the effects of time at 250 ^{o}C on residual stresses produced by shot-peening a series of candidate alloys. In most cases, heat treatment reduces the residual stress level, but in some alloys, there is more of an effect than others, offering an opportunity to adjust the residual stress to desired levels. Combined with fatigue studies, one or more of these alloys may emerge as leading candidates for improved high-pressure fuel injectors. Selected treated specimens will therefore be tested at ORNL using the notched, axial fatigue method described earlier.

New technical staff member. Mr. Tyson Jordan, a technical intern from Pellissippi State Community College has joined the project part-time. He will be trained by A. Shyam to help with both fatigue testing and optical imaging.

Plans for the coming quarter.
1) Continue to conduct axial fatigue tests on non-heat treated fuel injector alloy specimens that have been machined with EDM notches. Some of the hour-glass specimens will also be returned to Caterpillar for heat treatment after the EDM notches are produced at a specialty machine shop in Oak Ridge.

2) Obtain bar stock of the leading candidate Carpenter Technology alloy and begin testing and characterization.

3) Conduct nanoindentation studies of the walls of injector spray holes.

4) A journal article on the initial fatigue test results will be prepared.

Status of FY 2010 Milestones
1) Complete baseline fatigue tests on smooth specimens without artificial flaws.
(3/31/2010) Status: extended due to a delay in receiving heat-treated test specimens.

2) Complete fatigue tests on heat-treated steel specimens containing holes produced by the same process used on fuel injector nozzles. **(9/30/2010) Status**: on-going.

Communications/Visits/Travel
Coordination continues periodically between ORNL and Caterpillar by conference call.

Problems Encountered

There continues to be a delay in receiving specimens for fatigue studies. Fewer specimens were provided than were originally planned for ORNL fatigue testing. The Carpenter material has been fatigue-tested at Caterpillar but has not been available to ORNL. Since FY 2010 milestones (see above) are dependent on specimen material availability, the shortage of test specimen materials for ORNL continues to be a concern.

Publications/Presentations/Awards

Presentation. A poster, titled "Materials for High Pressure Fuel Injection Systems," was prepared and presented at the *2010 U.S. Department of Energy Hydrogen Program and Vehicle Technologies Program Annual Merit Review and Peer Evaluation Meeting* on June 10 in Washington, DC.

References

None

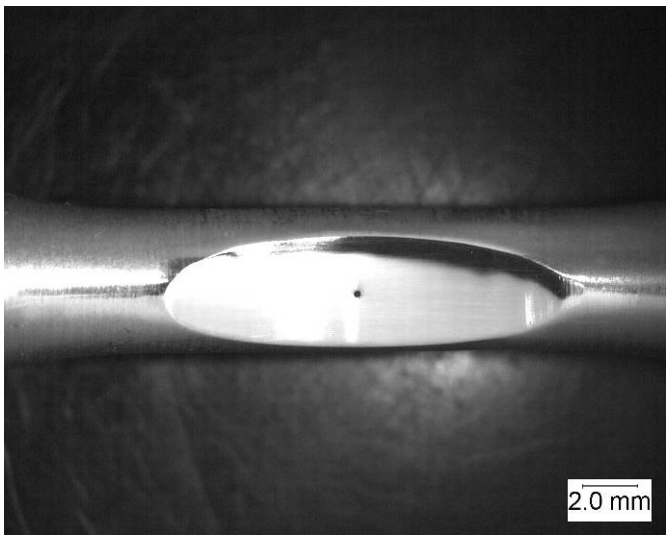

Figure 1. Polished flat section of an alloy steel axial fatigue specimen showing an EDM notch to simulate a fuel injector spray hole.

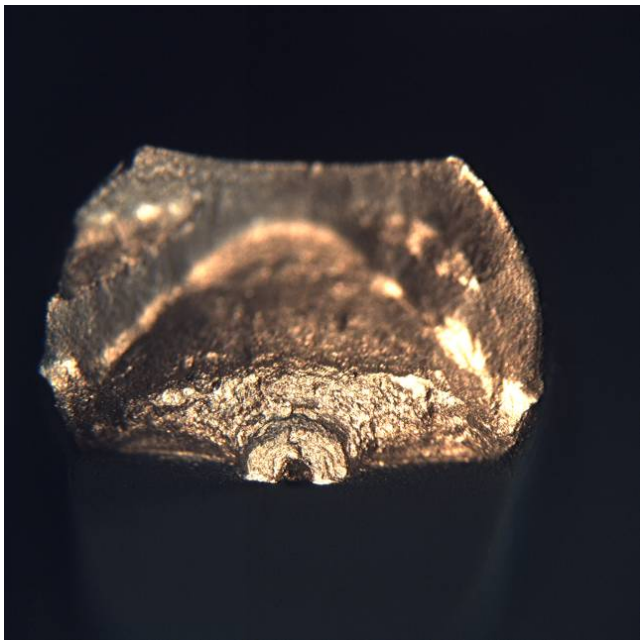

Figure 2. Test specimen showing a fatigue fracture that originated from an EDM notch (at bottom).

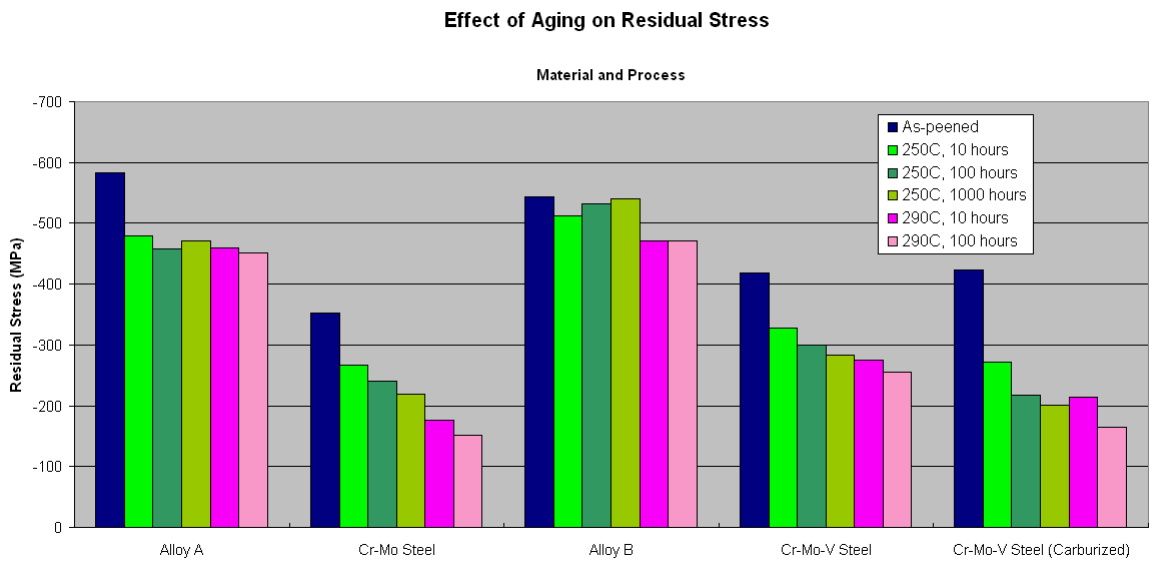

Figure 3. Effect of aging time and temperature on the compressive residual stress of shot-peened steels. Alloys A and B are high alloy steels, which retain their residual stress much better than the more conventional steels. A and B do have higher tempering temperatures, which may partially explain the different behavior.

Agreement 16304: Materials for Advanced Engine Valve Train

P. J. Maziasz and N. D. Evans
Oak Ridge National Laboratory

M. D. Veliz
Caterpillar, Inc.

Objective/Scope

This is an ORNL CRADA project with Caterpillar, NFE-07-00995 and DOE OVT Agreement 16304, which lasts for about 3.5 years, and is scheduled to end in Dec., 2010. This CRADA project focused on addressing the wear and failure modes of current on-highway heavy-duty diesel exhaust valves and seats, and then evaluating changes in valve-seat design or selection of advanced alloys, which will then enable higher temperature capability, as well as better performance and durability. The CRADA was extended for 12 more months due to technical success during the 2nd year of the project. Another 24 month extension was requested last quarter, due to the need to generate new creep-data and wear-test new prototype valves made of new Ni-based superalloys with more temperature capability. Requests for more detailed information on this project should be directed to Caterpillar, Inc.

Highlights

Caterpillar, Inc.

Caterpillar continued very high temperature wear-rig tests of new prototype exhaust valves made from upgrade Ni-based superalloys with higher temperature capability than standard 31V superalloy valves. Caterpillar also expanded the test temperature range, and included an additional seat-insert alloy.

ORNL

ORNL received tensile/creep specimens for testing at ORNL, made from the same upgrade Ni-based superalloys used to make new prototype exhaust valves for testing at Caterpillar. Creep-rupture testing at 800°C and above began at ORNL last quarter, to demonstrate higher temperature capability and performance compared to the standard 31V superalloy.

Technical Progress, 3rd Quarter, FY2010

Background

This OVT Agreement 16304 is an ongoing ORNL CRADA project with Caterpillar, NFE-07-00995, which will last for about 5.5 years, after this year's new 24 month extension. This CRADA project has addressed the wear and failure modes found for current on-highway heavy-duty diesel exhaust valves and seats. It then identified changes in valve-seat advanced alloys that will enable higher temperature capability, as well as better performance and durability. The need for such upgraded valve-seat alloys is driven by the demands to meet new emissions and fuel economy goals, which continue to push

diesel exhaust component temperature higher. The CRADA was originally scheduled to be complete at the end of 2009, but was extended for 12 more months and is being extended for another 24 months, due to outstanding technical progress and success at mitigating wear between exhaust valves and seat-inserts at above 800°C. Requests for more detailed information on this project should be directed to Caterpillar, Inc.

Approach

Caterpillar provides the baseline wear and mechanical behavior characteristics of engine-exposed standard valves and seats, and provides exposure of similar components from simulation-rig testing at Caterpillar. ORNL provides more in-depth characterization and microcharacterization of those valves and seats, and provides knowledge and understanding of the full range of commercially available heat-resistant alloys, to select those most suitable for upgraded valve performance. ORNL and Caterpillar have developed an understanding of the underlying degradation mechanisms, which is the technical basis for selecting and testing alternate valve and seat alloys with upgraded performance and temperature capability. Caterpillar and ORNL are working with Caterpillar's various component and materials suppliers, to enable prototype production of upgraded exhaust valves and seats for evaluation in Caterpillar's wear-test rig, and parallel testing and characterization of the same advanced alloys at ORNL.

Technical Progress – Caterpillar, Inc.

Caterpillar previously initiated a project with a major valve supplier to obtain heats of two advanced, alternate Ni-based superalloys for forging into upgraded exhaust valves. These new upgrade Ni-based alloys should have improved performance and higher temperature capability than the standard 31V alloy. Last quarter, Caterpillar received new prototype exhaust valves from its valve supplier, and completed some of the initial testing and evaluation of Ni-based 1 and 2 alloys in the wear-test rigs this quarter.

Technical Progress – ORNL

ORNL placed a sub-contract with Caterpillar's exhaust valve supplier to forge new valves and to make various mechanical properties test specimens previously, from two alternate alloys, Ni-based 1 and 2, with more temperature capability and performance than the standard 31V alloy. Both alternate Ni-based alloys have higher tensile yield strength (YS) when tested at 816°C (1500°F), as shown in Figure 1. ORNL received all of the test specimens, and began elevated temperature creep-rupture testing last quarter, which continued this quarter.

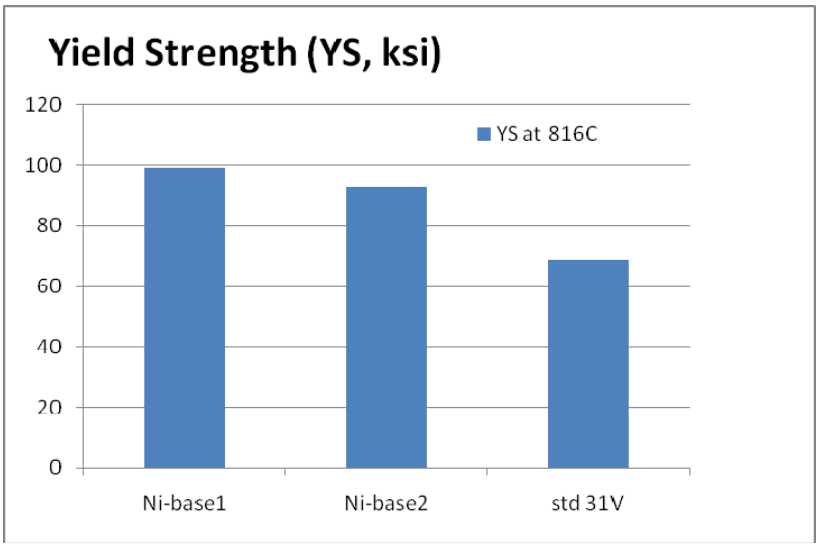

Figure 1 – Yield strength (YS) of the standard 31V exhaust valve alloy and two alternate upgrade Ni-based superalloys, for tensile tests in air at 816°C (1500°F).

Communications/Visits/Travel

Detailed team communications between ORNL and Caterpillar occur regularly in multi-party conference calls. Caterpillar has extended team discussions to include their commercial seat-insert supplier as well as one of their exhaust valve suppliers.

Status of Milestones (ORNL for DOE)

Milestone for Caterpillar rig-testing of prototype valves and seats of new advanced alloys is on schedule for FY 2010.

Publications/Presentations/Awards

None

Agreement 17257: Materials for Advanced Turbocharger Designs

P.J. Maziasz and A. Shyam
Oak Ridge National Laboratory

K. Pattabiraman
Honeywell Turbo Technologies

Objective/Scope

This is a recent ORNL CRADA project with Honeywell, NFE-08-01671 (DOE/EERE/OVT Agreement 17257), that began in August, 2009, and is scheduled to last for about 3 years. This CRADA project addresses the limitations of lifetime or use-temperature for the various components (casing, wheel, shaft, bearings) of both the turbine and compressor parts of the turbocharger system. As exhaust temperatures increase, to provide higher engine efficiency and lower emissions, turbocharger component temperatures also increase, so the need for more heat-resistant materials must be addressed. Requests for more detailed information on this CRADA project should be directed to Honeywell, Inc.

Highlights

This is a new project that began several quarters ago.

Technical Progress, 3rd Quarter, FY2010

Background

This recent CRADA project, which began at the end of FY2009, will extend for 3 years, and covers several different tasks. The first task was to assess and prioritize the various components that need or would most benefit from materials upgrades to increase temperature capability and performance, as well as durability and reliability. The next tasks examine current performance and degredation modes of wheel/shaft assemblies for turbines and compressors, housings for turbines and compressors, and bearings. These tasks may then obtain and test new materials with upgraded performance, and provide the results to Honeywell for designing advanced turbocharger systems, or manufacturing new prototype components for testing and evaluation.

Approach

This recent CRADA project was executed late in FY2009, and began several quarters ago. This project is comprised of six tasks, which will span the next 36 month period. Activity began with ORNL and Honeywell discussing the priority of the various turbocharger components for materials upgrades.

A turbocharger system includes the hot (turbine) end, driven by exhaust gas from the engine, a cold (compressor) end to increase air pressure into the combustion changer, and a transition region that connects these two ends. The turbine and compressor wheels are connected to a common shaft, supported by bearings. For the first task, the turbine wheel-shaft assembly was chosen as the first component for consideration, with analysis focused on residual stresses near the weld-joint of the Ni-based superalloy wheel to the steel shaft, which can upset balance during service. Another task of this new CRADA project continues previous work between ORNL and Honeywell on testing of the new CF8C-Plus cast stainless steel as a significant performance upgrade for the turbine housings relative to standard SiMo cast iron. This CRADA project for turbine housings will cover a broad range of other high temperature properties, including creep and fatigue strength, and expand it to turbine housing applications for passenger vehicle gasoline engines.

Technical Progress

For Task 1, Honeywell identified neutron-scattering experiments to measure residual stresses in welded wheel/shaft assemblies as one of their highest priority items.

For Task 2, efforts to define these experiments, including developing the proposal needed to obtain neutron scattering time at the HFIR Residual Stress User- Facility, began previously and continued this quarter.

For Task 3, ORNL continued several of the CF8C-Plus steel creep-rupture tests that were stopped during a previous ORNL/Honeywell CRADA project. ORNL also machined new tensile/creep specimens of CF8C-Plus steel to fill in the data gaps for selected high-temperature tensile and creep-rupture tests. Honeywell also identified the next steps necessary to commercially produce some prototype turbocharger housing using CF8C-Plus steel for certain turbocharger models, to that they could be evaluated and tested on engines. Figure 1 shows data from previous work by ORNL and Honeywell comparing the new CF8C-Plus steel to HK30-Nb at 700-900°C. HK30-Nb is a standard commercially available cast stainless alloy used for turbochargers for heavy-duty truck diesel engines when temperatures exceed the limitations of SiMo cast iron. CF8C-Plus cast stainless steel clearly has more creep-resistance than HK30-Nb stainless at 700-900°C, for the several creep-testing conditions shown in Figure 1.

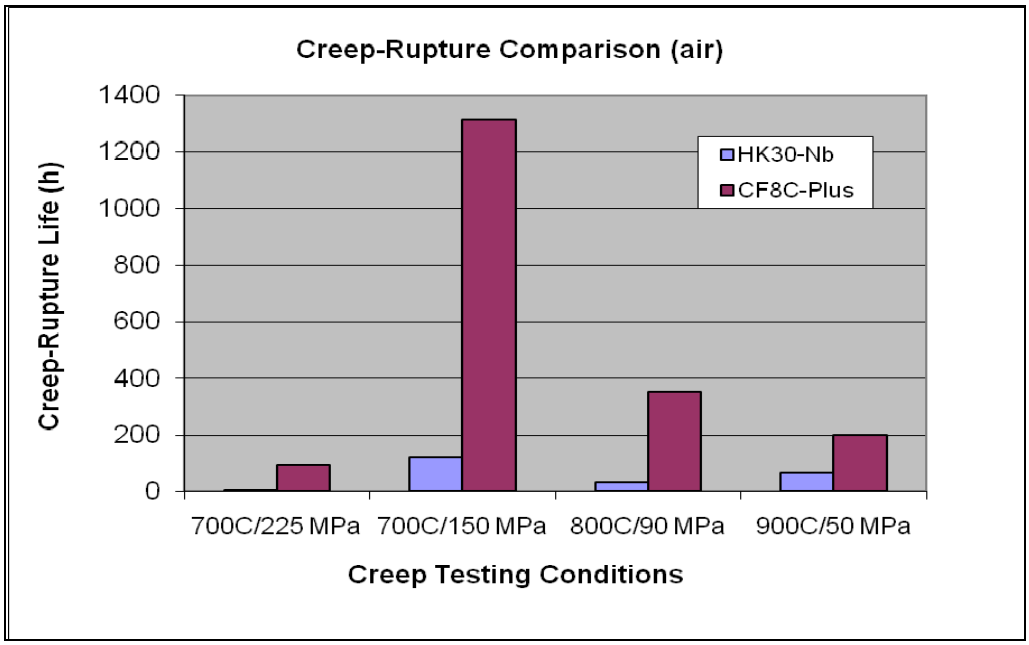

Figure 1 – Comparison of creep-rupture life for elevated temperature creep testing of both cast CF8C-Plus and cast HK30-Nb austenitic stainless steels in air. The CF8C-Plus cast stainless steel is clearly more creep-resistant at 700-900°C.

Communications/Visits/Travel

Periodic conference calls are held between ORNL and Honeywell Turbo Technologies, and email communications help to coordinate the work

Status of Milestones (ORNL for DOE)

New project in FY 2010, and milestones for FY 2011 are on-track.

Publications/Presentations/Awards

None

Agreement 17894: NDE for ACERT Engine Components

J. G. Sun
Argonne National Laboratory

Mark Veliz and J. A. Jensen
Caterpillar, Inc.
Technical Center

Objective/Scope

Applications of advanced materials in diesel engines may enhance combustion and reduce parasitic and thermal losses, thereby improving engine efficiency. Engine components developed from advanced materials, however, require rigorous assessment to assure their reliability and durability in more stringent operating conditions. The objective of this work is to develop and assess various nondestructive evaluation (NDE) methods for characterization of advanced engine components in a Caterpillar heavy-duty ACERT experimental engine at ORNL. NDE technologies established at ANL, including optical scanning, infrared thermal imaging, ultrasonics, and X-ray CT, will be further developed for detection of volumetric, planar, and other types of flaws that may limit the performance of these components. NDE development will be focused on achieving higher spatial resolution and detection sensitivity. Current efforts are directed in applications of optical methods for valvetrain components, X-ray and ultrasonic for joinings, and thermal imaging for thermal barrier coatings (TBC).

Technical Highlights

Work during this period (April-June 2010) focused on thermal imaging NDE analysis for TBC specimens received from Caterpillar and on development of a high depth-resolution algorithm for thermal tomography.

1. Thermal Imaging NDE for Thermal Barrier Coatings

During this period we continued thermal imaging NDE development for characterization of TBC specimens from Caterpillar. Although thermal imaging provided NDE data for the entire TBC surface, its lateral resolution is limited by the pixel size which is ~0.2 mm when testing 1-in.-squared specimens. On the other hand, optical methods such as laser backscatter have better lateral resolution, down to micron level, they however cannot resolve coating delaminations when optical depth penetration is shallow. Therefore, to validate thermal imaging NDE results, it is necessary to improve its lateral resolution so small delaminations that are common in these TBCs can be resolved and correlated with optical data. To achieve higher lateral resolution, the thermal-imaging experimental setup was carefully reconfigured by placing the camera lens closer to the sample as illustrated in Fig. 1. Because of the small space between the camera lens and sample surface, only one flash lamp was used with a large incident angle to the sample surface. As a result, heating efficiency was lower but appeared to be adequate.

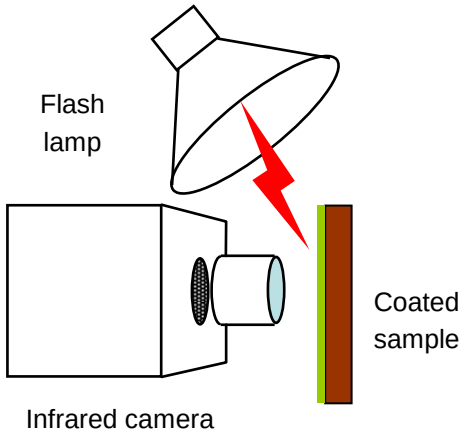

Fig. 1. Schematic illustration of the top view of the experimental setup.

Thermal imaging tests using the modified setup were conducted for thermal-cycled TBC specimen #9 that has been studied extensively by optical and thermal NDE methods. The specimen was imaged with various close-up arrangements (of different pixel sizes or lateral resolutions) and a high imaging rate of 1905 Hz. Of particular interest is a 10-mm x 5-mm region scanned by the laser backscatter method. Figure 2 shows a photograph of TBC #9 surface with the region being highlighted, along with the laser backscatter scan image and a typical raw thermal image (surface temperature image) for the same region. In the laser backscatter image, the high scatter-intensity regions correspond to coating surface (gray color in photograph) and low scatter-intensity regions to coating-spalled areas (dark-brown color in photograph). The raw thermal image represents the surface temperature rise after the flash, with brighter grayscale for higher temperature due to heat absorption on the specimen surface. The pixel size in the thermal image is ~78 µm. The thermal image has some similarity to the laser scan image, but shows more variations due to the different rate of heat conduction to the substrate at each surface location (affected by cracks and delaminations) and surface roughness. Typical thermal tomography plane slices are shown in Fig. 3. As determined previously (quarterly report Oct-Dec 2009), the first 7 plane slices are located within the coating layer (when coating exists) and the deeper slices are in the substrate. In plane slice #1 (on surface), all regions with low grayscale (low effusivity) represent the coated areas that are either damaged (with increased porosity) or cracked/delaminated, and the regions with brighter grayscale correspond to coating-spalled areas. The delaminated regions can be better identified in deeper depths within the coating layer, as seen in Slices #5 and #7 (the darker spots). The most severe delaminations are also seen in depths below the interface, Slice #10, which is due to the thermal diffusion effect. This effect is undesirable because it reduces spatial resolution and messes up the depth dimension. A method to reduce/remove this effect is being developed as to be discussed in the next section.

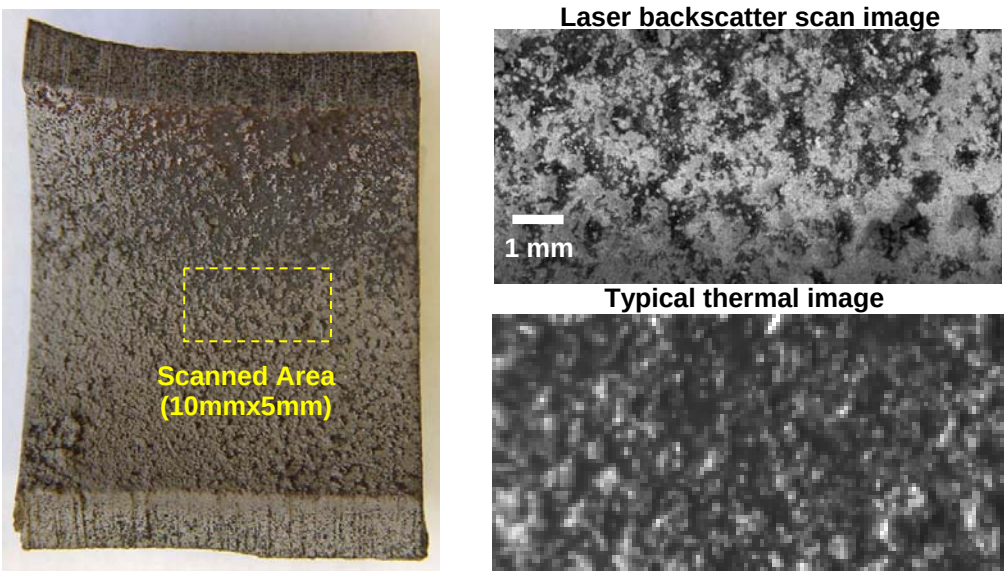

Fig. 2. Photograph of thermal-cycled TBC #9 surface, and laser backscatter scan image and raw thermal image of a 10 mm x 5 mm surface region marked in the photograph.

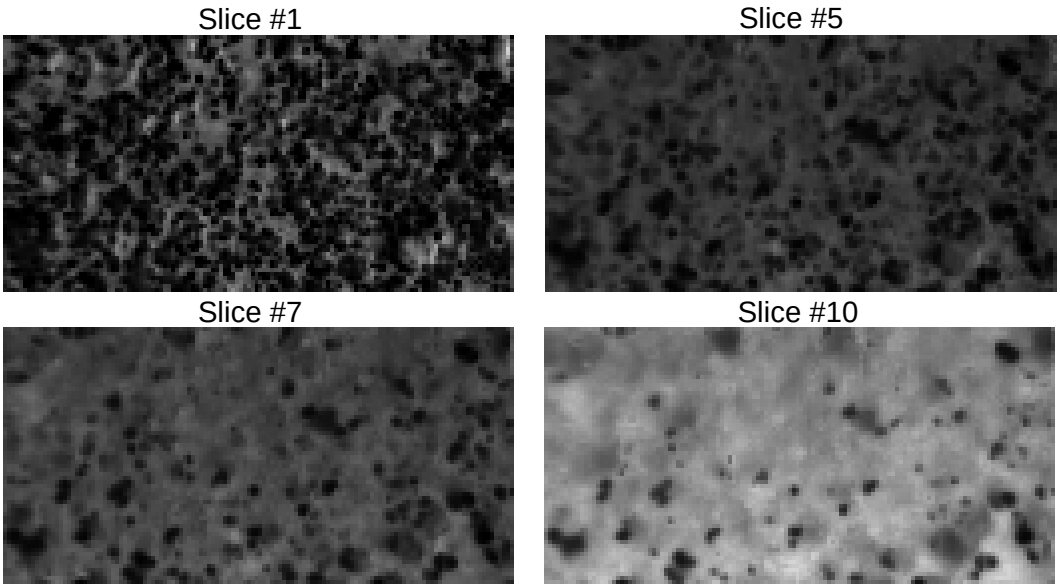

Fig. 3. Plane slices #1, #5, and #7 within the coating layer and #10 in the substrate for thermal-cycled TBC specimen #9.

The thermal tomography results are correlated with optical data to validate the detection of delaminations. Optical data that clearly show coating cracks/delaminations are photomicrographs of specimen surfaces. A micrograph for a region within the imaged area is shown in Fig. 4 and compared with the tomography image of the same region from the (rescaled) plane slice #5. From the micrograph, cracked/delaminated coatings can be easily identified because they are raised above surface as surface bumps. In the tomography image, all cracked/delaminated coatings are represented with lower

grayscale (low effusivity), and their size and shape are almost exactly the same as those shown in the micrograph (the size is slightly larger because of the large pixels). This correlation clearly demonstrates that the detected coating damages by thermal tomography are indeed coating cracks and delaminations; therefore, thermal tomography can be used for reliable inspection of coating conditions. In addition, thermal tomography detected other coating damages that are not visible on surface; two of these are circled in Fig. 4. These should also be delaminations under the coating layer.

The improved lateral resolution also helps to reveal other features that were not observed with coarse resolutions. Figure 5 shows two cross-sectional slices for TBC specimen #9. Three inclined darker features were detected; they run from the surface to the right side into the depths. These features are different from those of typical delaminations, which are aligned in the vertical direction as seen for some in Slice J=57. It is unclear if these are due to the shadowing effect of flash lighting because the flash lamp is located at the left side with a very low incident angle. The exact nature of these features is unknown and may need further investigation.

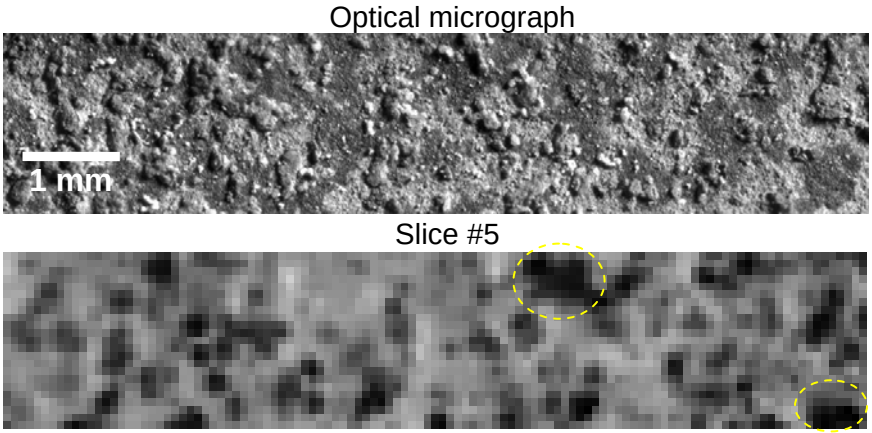

Fig. 4. Detailed comparison of surface micrograph and thermal tomography image for thermal-cycled TBC specimen #9.

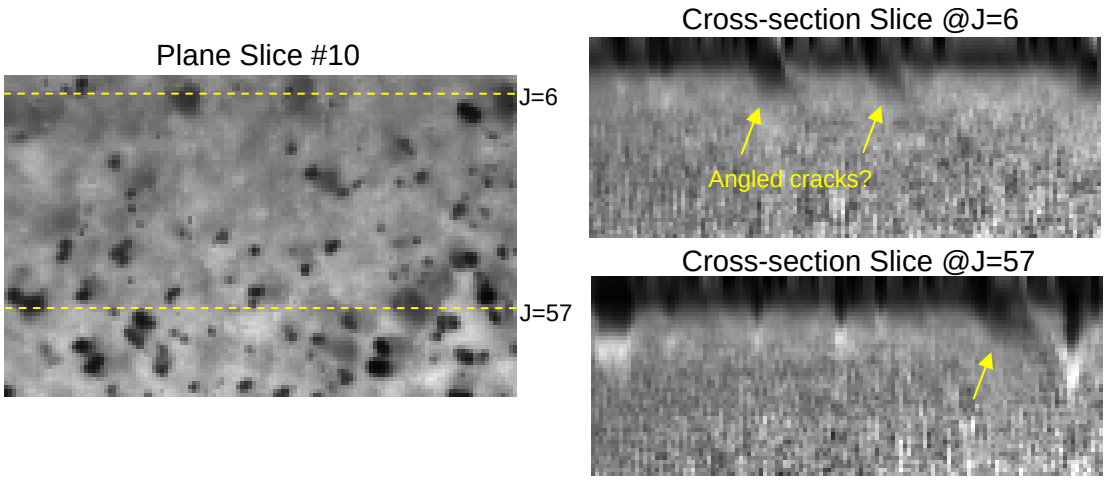

Fig. 5. Cross-section slices J=6 & J=57 at locations indicated in the plane slice #10 for thermal-cycled TBC specimen #9.

2. Development of High Depth-Resolution Algorithm for Thermal Tomography

During this period we continued the development of the new thermal tomography algorithm as described in the previous quarterly report. This algorithm is based on a rigorous convolution formulation as shown below:

$$e_a(z) = \int_0^\infty E(l)\, r(z/l)\, dl,$$

where $e_a(z)$ is measured apparent effusivity, $E(l)$ is the real material effusivity along depth l or z, and $r(z/l)$ is a response function. Because the discretized formulation of above equation results in a matrix of $r(z/l)$ that is singular, a damping parameter D was introduced so an iterative solution for $E(z)$ is required. The iteration operation however does not affect the solution time because the matrix size is small (100x100). Figure 6 shows the performance of the new algorithm as compared with the current algorithm for a single layer material of 1 mm thick and a constant effusivity of 2000. For this material, the exact solution is a step function, having a constant effusivity of 2000 within $0<z<1$ mm and 0 when $z>1$ mm. It is seen that the solution $e(z)$ from the current algorithm has a significant diffusion at the back surface $z=1$ mm. The solutions of the new algorithm, $E^0(z)$ and $E^{90}(z)$, corresponding to 0 and 90 iterations, have better resolution at the back surface and almost completely eliminated the diffusion in the solution $E^{90}(z)$. It can be shown that by choosing appropriate parameter D, the solution $E(z)$ can reproduce the exact solution. This new algorithm, although still under development for multilayer materials, for the first time demonstrates that the thermal diffusion effect can be removed, which has been the single limiting factor for wide application of thermal imaging technology. A U.S. patent for this algorithm has been filed during this period.

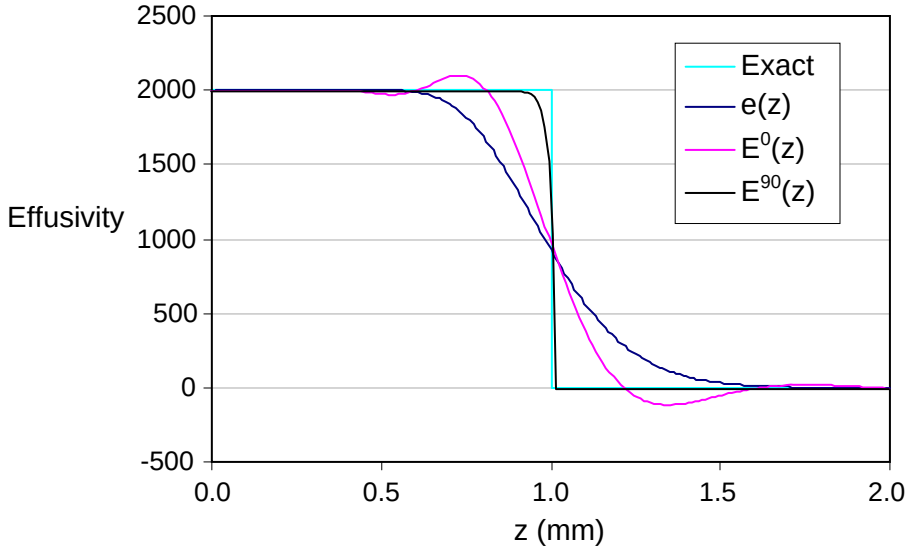

Fig. 6. Effusivity profiles as a function of depth for a one-layer material.

Status of Milestones

Current ANL milestones are on schedule.

Communications/Visits/Travel

J.G. Sun attended the 2010 Vehicle Technologies Annual Merit Review and Peer Evaluation Meeting, June 7-11, 2010, in Washington, D.C.

J.G. Sun plans to present a paper entitled "Quantitative Three-Dimensional Imaging by Thermal Tomography Method" at the 37th Annual Review of Progress in Quantitative Nondestructive Evaluation, San Diego, CA, July 18-23, 2010.

Problems Encountered

The laser backscatter system failed to operate during this period. It was identified that the network connection between the PC and the motion control unit was broken. The system is being diagnosed and fixed.

Publications

None this period.

Agreement 18570: Materials Alternative Fuels Compatibility

S. J. Pawel
Oak Ridge National Laboratory

Objective/Scope

The purpose of this Cooperative Research and Development Agreement (CRADA) between Oak Ridge National Laboratory and USCAR is to systematically evaluate compatibility between engine materials and ethanol fuel blends over a range of temperatures consistent with engine operation. Four primary tasks are included in the overall program:

1) surface analysis of materials exposed in field and lab exposures
2) in-situ extraction of gas and/or fluid from the valve seat crevice
3) development of electrochemical testing protocols
4) laboratory corrosion exposures of coupon materials

Technical Highlights

For Task 1 (surface analysis), a cylinder head has been sectioned by electro-discharge machining to expose critical valve seat crevice areas for surface analysis (microprobe, auger) and to facilitate placement of specimens in the analytical microscopes for examination. Figure 1 shows one such cylinder head for which surface analysis has been initiated. The goal of this effort is to identify corrosion products and surface constituents that may suggest corrosion mechanisms, or perhaps direct development of screening tests to identify materials or material combinations less susceptible to corrosion.

For Task 2 (in-situ extraction of gas/liquid from valve seat crevice), the initial proof of concept has been completed, and an engine head is being modified by one of the USCAR Partners to facilitate this testing.

For Task 3 (electrochemical test development), specimens of the aluminum-based engine alloy have been machined in two orientations from one of the heads delivered for analysis. Fabrication of reference electrodes is on-going, although further effort will be required to develop a suitable resistance across the solution/electrode tip for the routine use. Initial autoclave testing is expected in the coming quarter. In addition, the USCAR Partners are attempting to procure, through suppliers, appropriate stock material (cast bars) with which to fabricate tests specimens representing the Fe-based valve seat alloy and the Al-based engine alloys.

Status of FY2010 Milestones

Work initiated.

Communications/Visits/Travel

Routine electronic mail and telephone contact is being maintained between the USCAR Technical Lead and the ORNL PI. No travel occurred this quarter.

Problems Encountered
None

Publications/Presentations/Awards
None

References
None

Figure 1. A representative cylinder head sent to ORNL as been sectioned to facilitate surface analysis of the valve seat crevice region. Sectioning was required to reduce the specimen size and expose critical surfaces for microprobe and auger analysis. These pieces retain the as-received (from engine testing) corrosion products to the greatest extent possible.

Agreement 18571: Materials Issues Associated with Exhaust Gas Recirculation Systems

M. J. Lance, C. S. Sluder and J. M. E. Storey
Oak Ridge National Laboratory

Objective/Scope

Provide information to industry specialists about fouling deposit properties so as to enable improved models and potential design improvements to reduce fouling and its impact on the performance of EGR (exhaust gas recirculation) coolers.

Technical Highlights

In February of 2009, a consortium consisting of engineers responsible for EGR systems was assembled from nine diesel engine manufacturers and surveyed to identify the biggest problems facing EGR systems. EGR cooler fouling was identified as a very critical concern. Each member of the EGR consortium agreed to provide a cooler that had seen enough operation to categorize it as 'half-useful-life'. Of the nine members, the seven companies that currently use HP-EGR all sent at least one fouled cooler for analysis with the results to be shared with the entire consortium.

Three removal mechanisms were identified in the coolers that, to the authors' knowledge, have not heretofore been described in the literature on EGR cooler fouling. Figure 1 shows all three of these phenomena in one image from cooler deposit #8. Longitudinal grooves form on the leading edge of the turbulation structure (here a sinusoidal wave down the length of the cooler). These grooves could be formed by debris hitting and eroding the deposit propelled by the exhaust gas. This debris may then roll along the deposit, collecting more deposit forming a groove. A second feature in Figure 1 is mudcracking which will form as the deposit shrinks in the plane of the metal substrate presumably due to hydrocarbon and water condensation. Conversely, mudcracks may also form during drying of the deposit after the engine is turned off.

A third feature from Figure 1 is spallation which seems to be linked to mudcracking. Once mudcracks have encircled a region of the deposit, and if shrinkage of the deposit continues, it will begin to buckle and will eventually spall. The fracture plane for the spalled region in Figure 1 was within the coarse region of the deposit, and not at the metal-deposit interface. This was also the case for coolers #1 and #2 which also exhibited spallation. This suggests that hydrocarbon and water condensation will promote spallation both by shrinking the deposit and by providing a brittle fracture plane for a crack to propagate. This may be the origin of spontaneous regeneration that has been reported by many EGR consortium members.

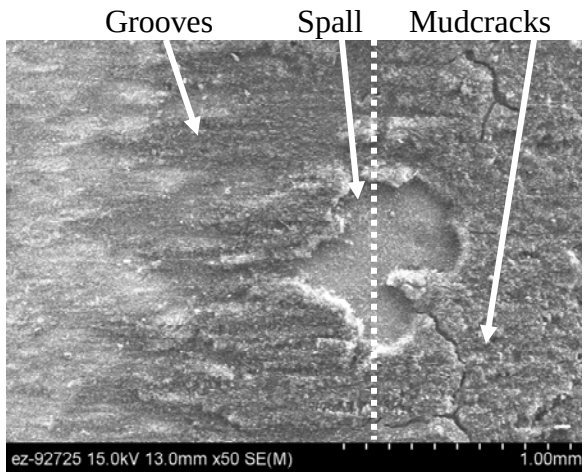

Figure 1. SEM image of the surface of cooler deposit #8. The dashed white line indicates the peak of the sinusoidal wave of the turbulation structure (see Figure 9 for cross-section view).

Tube Reactor System for EGR Particulate Hydration

A tube reactor system (Figure 2) was designed to flow humid or hydrocarbon-laden exhaust-type gases over particulate deposits in a single EGR tube. The system consists of a gas manifold supplied by two (can be expanded to four) digital mass flow controllers flowing air or bottled gases, a water vapor introduction system, a gas heater and a water jacket to cool or heat the sample tube. Additionally, the water jacket can be left empty for an insulated system. It is equipped with multiple thermocouples to monitor gas temperature before and after the sample and the cooling water entry and exit temperatures. This tube reactor will be used to age engine-produced deposits under different exhaust gas conditions and coolant temperatures.

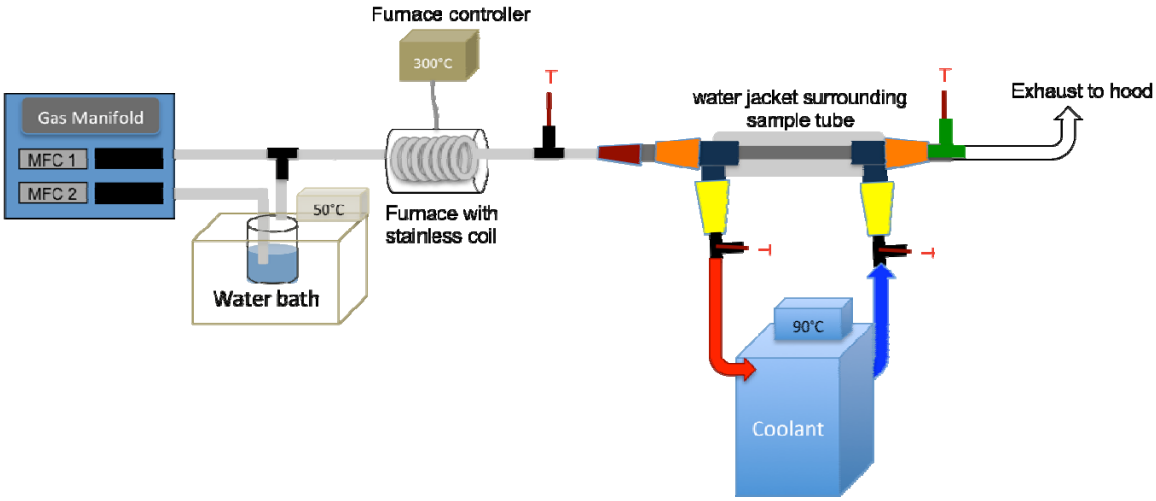

Figure 2. Tube Reactor system schematic

Status of FY2010 Milestones

Complete chemical and microstructural characterization of industry provided coolers. **(09/10)** *On Schedule.*

Communications/Visits/Travel

None.

Problems Encountered

None.

Publications/Presentations/Awards

- Results on neutron tomography were presented to the Diesel Crosscut Team.
- An update was provided to Ford on May 20th, 2010.

References

Michael J. Lance, C. Scott Sluder, John M. E. Storey, and Samuel A. Lewis Sr., "Characterization of Field-Aged EGR Cooler Deposits," to be published SAE 2010-01-2091.

Agreement 19202: Titanium Friction and Wear
(Surface Engineering of Bearing Components)

Peter Blau and Dinesh Bansal
Oak Ridge National Laboratory

Objective/Scope

Energy efficiency and durability of internal combustion engines (ICEs), whether fueled by conventional or alternative fuels, benefits from the utilization of lightweight materials. Examples include fiber composites and alloys of aluminum, magnesium, and titanium. While such materials offer attractive efficiency gains, their use also presents technical and economic challenges. The nature of those challenges depends upon which materials and engine components are involved. One class of applications involves tribological applications: that is, those which concern friction, wear, and lubrication. Studies in the United States, Japan, and the United Kingdom have shown that mechanical losses comprise about fifteen percent of the energy dissipation from fuel in a typical ICE, and that of those, energy losses by friction comprise about eighty percent. The two major subsystems in terms of engine frictional losses are the piston ring/cylinder interface and the engine bearings. Past work at ORNL and other organizations has focused on the piston ring/cylinder interface. The current project, beginning in FY 2010, not only addresses the second contributor: connecting rod bearings, but it also demonstrates surface engineering technologies that could benefit other transportation applications as well.

The objective of this project is to ***enable the use of lightweight titanium (Ti) alloys for both connecting rods (CRs) and crankshafts*** by applying integrated surface-engineering methods to effect significant improvements in the lubricity and durability of bearing surfaces. The goal is to evaluate and identify the best available surface engineering methods to reduce friction and wear of Ti alloys under engine-simulated contact conditions. This work compliments recent developments in Ti processing technology, especially that being studied at PNNL, to reduce raw material cost. It utilizes the experience and capabilities of ORNL to effect changes in surface-critical properties via a variety of potential treatment routes. The three phases of this effort are:

1. *To down-select surface treatment technologies*. Laboratory-scale testing of candidate surface treatments and coatings will be conducted using simple coupons and ASTM test methods. These will include both commercial and experimental coatings. In parallel, a variable loading spectrum bearing wear and friction apparatus will be built. (Year 1)

2. *Simulative, variable load testing*. To perform tests on selected surface engineered Ti samples using the spectrum-loading bearing tester that was designed and built during Phase 1. (Years 2 and 3)

3. *Scale-up testing*. Scale-up and dynamometer testing of a titanium connecting rod produced using the preferred surface engineering (Year 3)

Technical Highlights

Candidate surface engineering approaches. Based on a comprehensive literature review, consultation with industry, and prior experience of the ORNL staff, a list of candidate surface treatments and coatings was compiled. Further discussion and analysis pared down that list to a smaller number of promising approaches. In addition to coatings and surface treatments, some bulk materials were also included to benchmark friction and wear performance.

Table 1 lists the materials being evaluated in Phase 1. The Ti-6Al-4V substrates were machined from bar stock and pre-polished at ORNL before being distributed for treatment or coating. As the footnotes show, samples were processed by a variety of sources: ORNL, commercial companies, company R&D laboratories, and another national laboratory (Argonne National Laboratory). Note that Eaton Corporation provided nanocomposite coatings from a sister program sponsored by DOE's Office of Industrial Technologies. Due to industry interest in this work, most of the treatments, including a number of commercial coatings, were contributed to the project at no charge. However, in a few cases, such as nitriding heat treatments and shot peening, services were purchased.

Progress in Friction and Wear Screening. The results of baseline tests of AISI 52100 steel balls against untreated Ti-6Al-4V (Table 1, Line 1) were discussed in the second quarterly report, as was the rationale for the selected test conditions. For convenience, a summary of the tribotest conditions is reproduced in Table 2. Tribology test coupons are also tested for hardness and affected layer depth or coating thickness. Most of the tests are being conducted under the modified ASTM G133 Procedure B that involves lubrication by engine-conditioned diesel oil. That approach has been found to provide a more realistic ranking of bearing performance than tests in fresh oil. Barring severe wear, three tests are conducted for each candidate material.

Progress in friction and wear testing. Oxygen diffusion treated Ti-6Al-4V (Table 1, Line 6). Ti-6Al-4V base material was used as the substrate for an oxygen diffusion (OD) treatment consisting of exposure to 800ºC in air for two hours, followed by an air cool. Loose surface scales were lightly abraded away to produce a smooth surface with an enriched oxygen subsurface zone approximately 20 μm thick. Coefficient of friction (μ) versus time for three repeated tests (Proc. B-mod.) is shown in Figure 1. The average μ ranged from 0.05 to 0.08. For non-lubricated tests (Proc. A), the average μ over the course of sliding ranged from 0.6 – 0.8. Thus, the OD treatment seems more suitable for lubricated sliding than dry contact. Measurements of the wear scars on both ball and coupon specimens also indicated that wear was greatly reduced under lubricated sliding. A substantial amount of powdery, yellow-orange wear debris was generated during the non-lubricated tests.

Table 1. Materials and Treatments Being Considered and Investigated in Phase 1

	BULK MATERIALS
1	Baseline, non-treated Ti-6Al-4V
2	Pb-Sn bronze alloy CDA 932 (baseline bearing bronze)*
3	60Ni-40Ti (a NASA development)**
	MECHANICAL TREATMENTS
4	Shot peening*
5	Low plasticity burnishing*
	THERMAL and CHEMICAL TREATMENTS
6	Oxygen diffusion treatment (developed by J. Qu at ORNL)**
7	Carburizing*
8	Nitriding*
9	Surface alloying to form 60Ni-Ti (pending results of tests on bulk 60Ni-40Ti, line 3)
10	Electrochemical anodizing*
	HARD and SOFT COATINGS
11	TiN hard coating*
12	CrN hard coating*
13	DLC hard coating ***
14	Nanocomposite AlMgB (developed under a DOE/ITP project)****
15	In situ IR-produced Ti MMC (developed at ORNL under Laboratory Directed R&D funding)**
16	Metallic soft coating of Cu-Ni-In on Ti-6Al-4V*
17	Metallic soft coating of Cu-Ni-In on CDA 932 bronze*
	HYBRID TREATMENTS
18	Shot peening* after oxygen diffusion treatment**
19	Shot peening* after carburizing*
20	Shot peening* after nitriding*
21	Cu-Ni-In soft coating* after shot peening*

** Commercial source, ** Produced at ORNL, *** Produced at ANL, **** Produced at a company R&D Lab*

Table 2. ASTM G 133 Test Conditions

Test Variable	Procedure A	Procedure B
Applied load (N)	25.	200.
Sliding stroke length (mm)	10.	10
Speed of oscillation (cycles/s)	5	10
Test length (s)	1000.	2000.
Sliding distance (m)	100.	400.
Surrounding atmosphere	ambient air	ambient air
Relative humidity (%)	40 - 60	not specified
Lubrication method	none	surface immersion
Lubricant temperature (C)	not applicable	150 (Note 1)
Air temperature (C)	22 +/- 3	not specified
Ball (slider) diameter (mm)	9.525	9.525

Note 1: For this work, the lubricant was used at room temperature. Therefore, results are reported as being performed under a modified Procedure B.

Microcomposite formed in situ by infrared (IR) surface processing (Table 1, line 15). A novel, infrared surface treatment was used to produce Ti matrix composite coating deposits approximately 300 to 500 µm thick, containing micrometer-sized hard particles. They were prepared at ORNL by rapid surface melting of mixed powders (Ti-6Al-4V plus approximately 25% by volume of -100 mesh TiB_2 powder) using a Vortek™ plasma arc lamp. Further information on this treatment may be found in Ref. [1]. Prior to tribotesting, the coupon specimens were exposed to 485°C in air for approximately 3 h to produce a thin layer of oxide. Figure 2 shows the variation of µ during the course of sliding for the tests under lubricated conditions (Proc. B-mod). In both the test cases a spike in µ accompanied with large vibrations, was observed after about 17 min. of sliding. Tests were terminated shortly after that point. This behavior is typical of failure by scuffing.

Bearing bronze (BB). Alloy CDA 932 is a popular leaded bronze alloy used in plain bearings for engines. The alloy was tested in the as-received condition after surface finishing in successive steps to a 1.0 µm diamond lapped finish. Friction and wear behavior was repeatable on all three tests of this material.

In summary, Figure 3 compares the variation in µ with time for bare Ti-6Al-4V, OD-treated Ti-6Al-4V, IR-treated Ti-6Al-4V, and BB in used diesel engine oil (Proc. B-mod). Tests with untreated and IR treated Ti-6Al-4V failed prematurely while tests with OD treated Ti-6Al-4V and bearing bronze completed successfully. It should be noted that for OD treated Ti-6Al-4V (around 0.085) was actually lower than that of BB (0.094). The friction and wear results generated during Phase 1 will be presented at the 2011 International Conference on Wear of Materials (see Publications, below), and the same paper will be submitted to *Wear* journal for archival publication.

Progress in the design of a spectrum loading test system. A computer-aided design package was obtained and is being employed by Dr. Bansal to design the spectrum load bearing materials test system to be used in Phase II of this work. Parts have been ordered, and some have been received. These include a 3-phase motor, computer controlled motor drive, a sturdy base unit, and a pre-drilled mounting plate. An area in the ORNL tribology laboratory has been reorganized to provide space for the apparatus.

Future Plans. In the upcoming quarter, plans include (1) concluding coupon testing on the majority of treatments listed in Table 1, and (2) assembling the prototype load spectrum test apparatus.

Status of FY 2010 Milestones

Design friction and wear testing apparatus to simulate connecting rod motions, loads, and speeds, and complete a series of baseline experiments on small test coupons of candidate titanium alloys, with and without surface treatments. **(09/10)** *Status: on schedule***.**

Communications/Visits/Travel

P. Blau attended the 65th Annual Meeting of the Society for Tribologists and Lubrication Engineers (STLE) to investigate surface engineering approaches for metals and alloys being developed by the international technical community. Discussions led to the expansion of the test matrix of candidate surface engineering approaches.

Problems Encountered

It has taken longer than expected to establish a non-disclosure agreement with a diesel engine manufacturer who has expressed an interest in working with ORNL on this project. It is expected that any remaining intellectual property issues will be resolved during the coming quarter, and that we can immediately begin to discuss engine bearing operating information to aid in our design of the simulative testing protocols.

Publications/Presentations/Awards

1) P. Blau presented an overview of this project during the *2010 U.S. Department of Energy Hydrogen Program and Vehicle Technologies Program Annual Merit Review and Peer Evaluation Meeting* on June 10 in Washington, DC. It was part of a technical session on Propulsion System Materials, organized and chaired by J. Gibbs (DOE).

2) D. Bansal and P. Blau have submitted a paper to the 2011 International Conference on Wear of Materials. The title is: “Surface engineering to improve the durability and lubricity of Ti-6Al-4V alloy.” The conference is scheduled for April, 2011, in Philadelphia. Blau is also a member of the conference organizing committee.

References

[1] P. J. Blau, D. L. Erdman III, E. Ohriner, and B. C. Jolly (2010) “High-Temperature Galling Characteristics of Ti-6Al-4V with and without Surface Treatments,” accepted for *Tribology Transactions*.

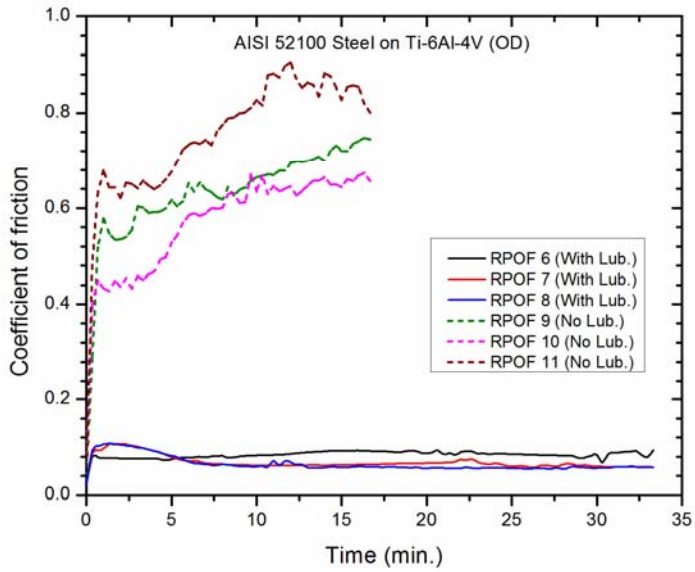

Figure 1. Variation in coefficient of friction with time for tests with OD-Ti-6Al-4V.

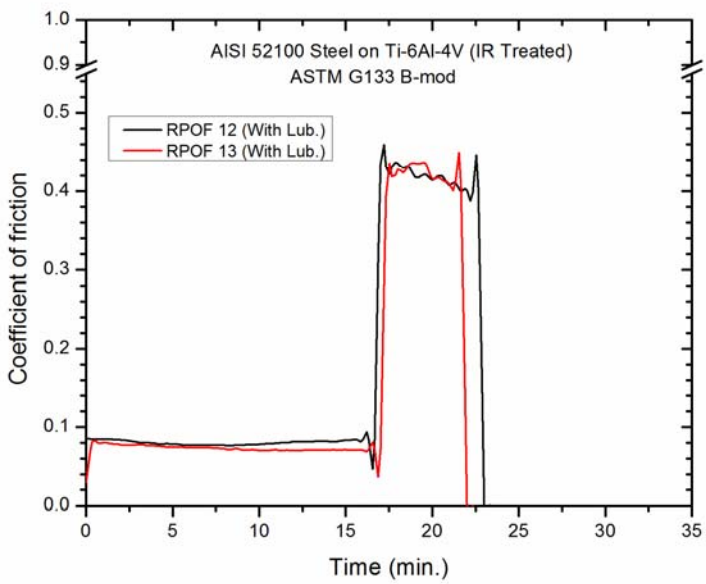

Figure 2. Variation in coefficient of friction with time for tests with IR treated Ti-6Al-4V

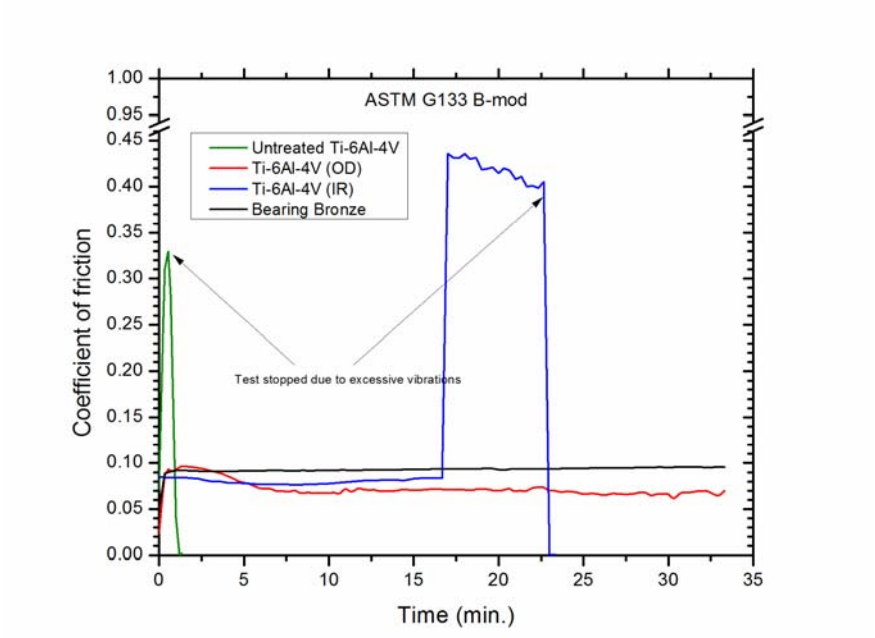

Figure 3. Comparison of the variation in coefficient of friction for 52100 steel sliding against four materials in engine-conditioned diesel oil.

Agreement 10461: Durability and Reliability of Ceramic Substrates for Diesel Particulate Filters

Thomas R. Watkins, Amit Shyam, Hua-Tay Lin and Edgar Lara-Curzio
Oak Ridge National Laboratory

Randall J. Stafford
Cummins, Inc.

Objectives

The objective of this effort is to identify and implement test techniques to characterize the physical and mechanical properties of ceramic substrates used as diesel particulate matter filters (DPFs), to identify the mechanisms responsible for the degradation and failure of DPFs and to develop analysis tools for predicting their reliability and durability.

Goals, Barriers, Relevance & Integration

In the study area of the DOE Office of Vehicle Technology's (OVT) Advanced Combustion Engine research, the *goals* are to (1) improved commercial vehicle engine efficiency by at least 20% and (2) to achieve engine system cost, durability and emissions targets. This project addresses the three *barriers* related to the Emission Control System in this study area: Improving durability, numerous components and costly precious metal content. This project is *relevant* to the first goal as the understanding of the relationships of the material properties for the filter (and catalyst) substrates enables optimization of porosity, strength, elastic modulus, thermal conductivity, thermal expansion, etc. leading to thermal management and improved efficiency. This project supports clean diesel, which increases acceptance by the public. Larger acceptance, in turn, results in larger percentages of conversion to diesel, with the resulting reduction in petroleum usage/dependency upon foreign oil. This project is *relevant* to the second goal as the thrust is to characterize and improve the durability, resulting in the lowest overall cost and preventing emission release in service. This project is *integrated* within Vehicle Technologies program as it utilizes characterization tools acquired and maintained by the High Temperature Materials Laboratory (HTML) Program.

Technical Progress

In the reporting period, the ORNL team began characterizing a new Al_2TiO_5-based DPFs. The DPF was sectioned and samples were machined. The cross-section revealed a new honeycomb design with 2 channel sizes (see Figure 1; asymmetric cell size). The larger channel size is on the inlet side and is designed to allow ash to accumulate in the DPF without plugging the channel. In Figure 2, the microstructure exhibits high porosity, rectangular-shaped grain and numerous microcracks as viewed with a SEM. X-ray diffraction indicates that the Al_2TiO_5-based DPF material contains 3 phases: Al_2TiO_5, a feldspar and an unidentified phase which is not mullite. Figure 4 shows the large thermal expansion hysteresis through two heating and cooling cycles. The behavior is due the large thermal expansion anisotropy Al_2TiO_5; the single crystal coefficients for thermal expansion (CTE, α), the sample contracts are $\alpha_a \approx$ 20–22; $\alpha_b \approx$

10–11; $\alpha_c \approx -3 \times 10^{-6}/°C$.[1] The CTE for polycrystalline Al_2TiO_5 without microcracks would be about $9.7 \times 10^{-6}/°C$.[1] Initially upon heat up, the expansion along the a and b directions within the grains is directed into the microcracks (closing them) such that only the contraction along the C direction is measured. Around 150°C, these cracks close enough that positive expansion occurs. During heating at the highest temperatures, these microcracks close and sinter together (heal), which is the origin of the different contraction path.[2,3,4] As stresses build up between the grains on cooling, microcracks form or reform (refracture) noticeably starting at ~700°C. At room temperature, there is a noticeable off-set from the initial length. This is due to the fact that the initial sample was sintered at a higher temperature than 1000°C. As such, some microcracks were healed and not refractured because the change in temperature of the expansion test was less than the initial fabrication sintering temperature. Subsequent heating and cooling expansion curve are reproducible. The CTE curves in Figure 4b tell a similar story showing the CTE as negative and gradually increasing to just above $2 \times 10^{-6}/°C$. The CTEs on cooling are initially due to the reduced number of microcracks. After about 700°C, the CTEs are similar. Reheating shows a near zero CTE until about 400°C. The higher final CTE on reheating is again attributed to the reduced number of microcracks relative to the initial heat. Excluding the initial heat, the average CTEs were 1.07 and $2.17 \times 10^{-6}/°C$ in the direction parallel and perpendicular to the extrusion direction, respectively. These low CTE values relative to the polycrystalline average above is due in large part to the large amount of porosity present (bulk density = 1.65 g/cc; skeletal density (excludes open porosity) = 3.43 g/cc; relative density = 48.2% or 51.8% porosity).[5] Figure 5 show the fracture toughness, K_{IC}, as measured with the double torsion technique, increasing as a function of strength. The strength values were corrected for the moment of inertia of the honeycomb structure for three DPF materials. Both the fracture toughness and strength increase with decreasing porosity for the cordierite data. The lowest and highest strength samples have relative densities/porosities of 68.1 and 50.2%, respectively. The mullite-based material possessed an unusual microstructure of interpenetrating needles, which results in the high strength and toughness with high porosity (63.1%).

Since fracture toughness measurements are easier to perform and require less material than strength testing, a new thermal shock parameter, $R_K=K_{IC}/\alpha E$, has been adopted as was discussed previously,[6] where E is the Young's modulus. R_K is calculated from measured parameters and is tabulated for various DPF materials and conditions in Figure 6. This simplified analysis provides a means to compare and suggests the coated samples and samples that have been aged appear to be more thermal shock tolerant. Figure 7 is a Weibull plot for four point bend strengths[7] of the Al_2TiO_5-based DPF material. The plot suggests two flaw populations are present; a mean strength of 2.98 MPa was determined. Figure 8 shows the dynamic fatigue data. The Al_2TiO_5-based DPF exhibits a lower strength than cordierite. Although not shown, neither material exhibited a specimen size effect nor a strong response to elevated temperature.

Meetings

Thomas Watkins and Amit Shyam travelled to Columbus, IN for technical discussions related to the CRADA on December 1, 2009.

ORNL and Cummins personnel traveled to Daytona Beach, FL for a meeting of the ASTM C28.01 Mechanical Properties and Reliability committee on January 24, 2010 which, in part, provides standards for the DPF community. On the same trip, a related technical talk was presented by T.R. Watkins at the 34th International Conference and Exposition on Advanced Ceramics and Composites, Daytona Beach, FL, January 27, 2010. The co-authors and talk titles are:

T.R. Watkins, A. Shyam, H.T. Lin, E. Lara-Curzio, R.J. Stafford, "Microstructure and Select Mechanical Properties of an Aluminum Titanate-Based Diesel Particulate Filter."

T. R. Watkins, A. Shyam, H.T. Lin, E. Lara-Curzio, R. Stafford, T. Yonushonis, "Durability of Diesel Engine Particulate Filters," presented at the DOE 2010 Vehicle Technologies Annual Merit Review and Peer Evaluation Meeting, Washington, D.C., June 10, 2010.

References

1. Thomas & Stevens, J. Br. Ceram. Trans. 1989.
2. Buessem et. al., Ceram. Age 1952.
3. Bush & Hummel, J. Am. Ceram. Soc. 1958, 1959.
4. Morosin & Lynch, Acta Cryst. 1972.
5. Definitions given in ASTM D3766, ASTM International, West Conshohocken, PA.
6. T. R. Watkins, A. Shyam and E. Lara-Curzio, "Durability of Diesel Particulate Filters (CRADA No. ORNL-04-0692 with Cummins Inc.)," FY 2009 Progress Report for the Heavy Vehicle Propulsion Materials Program, December 2009.
7. ASTM C1674-08, Test Method B.

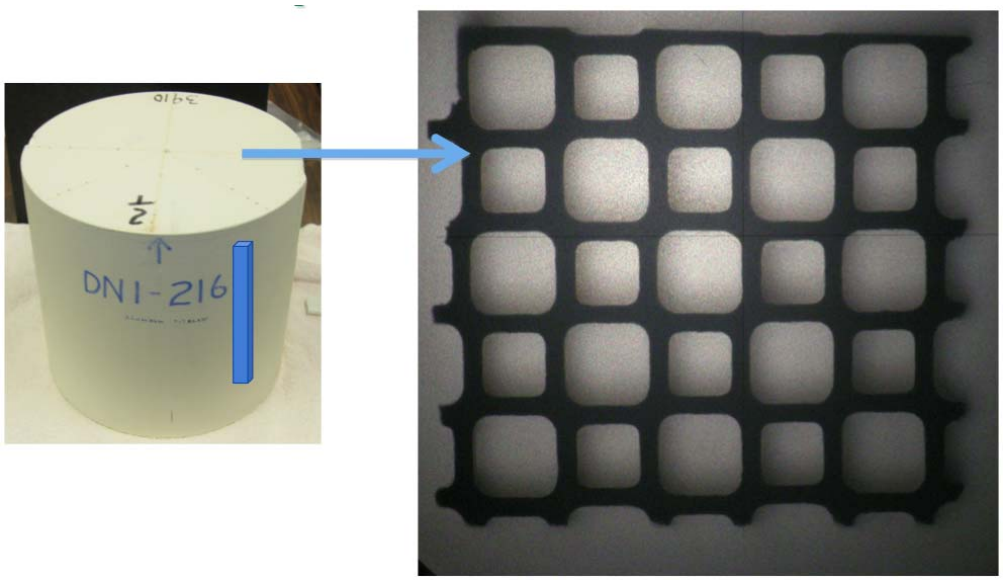

Figure 1 – (left) An Al_2TiO_5-based DPF, nominal dimensions: 26.5 X 25.5 cm (D X H), received from Corning. (right) expanded view of the cross-section showing two channel sizes. The nominal dimensions of the cells are 1.4 x 1.4 and 1 x1 mm.

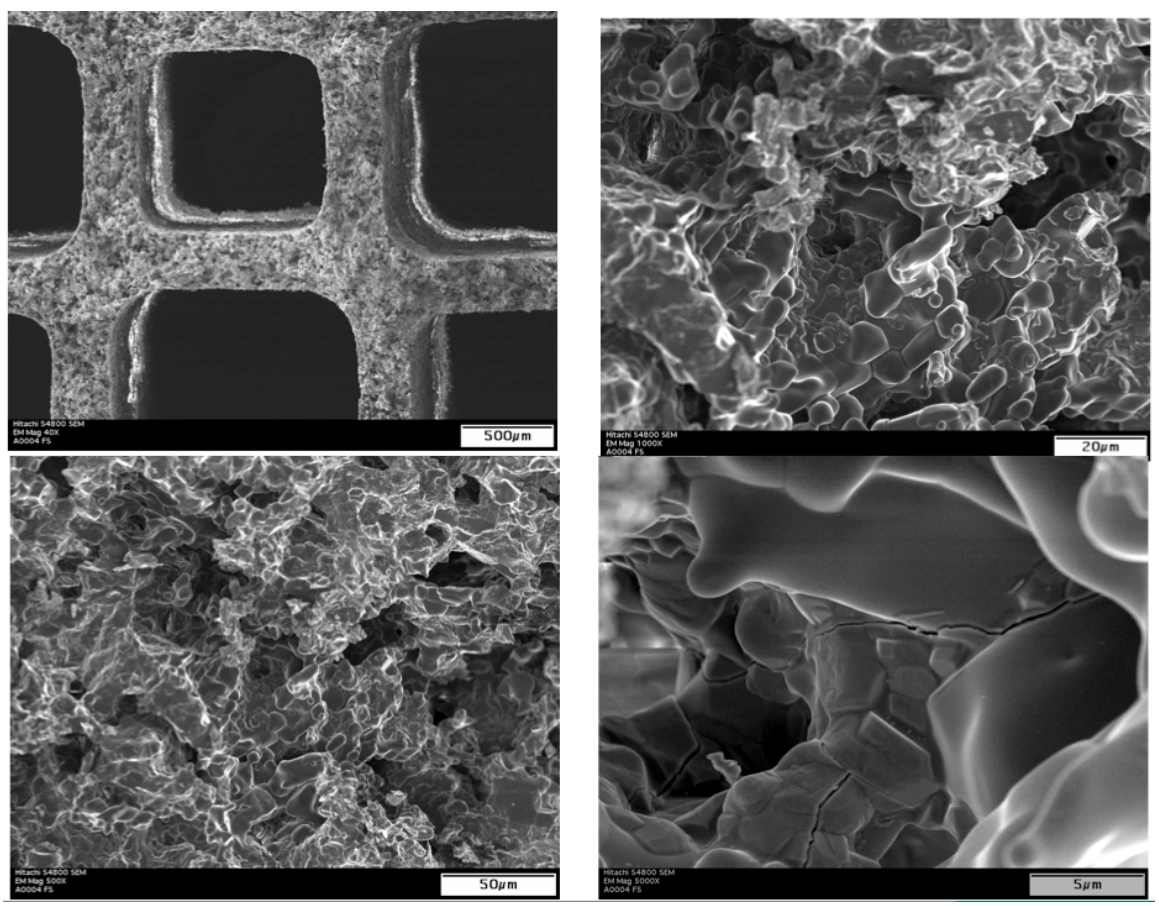

Figure 2 – SEM micrographs of the Al_2TiO_5-based DPF showing rectangular grains in a porous, microcracked microstructure.

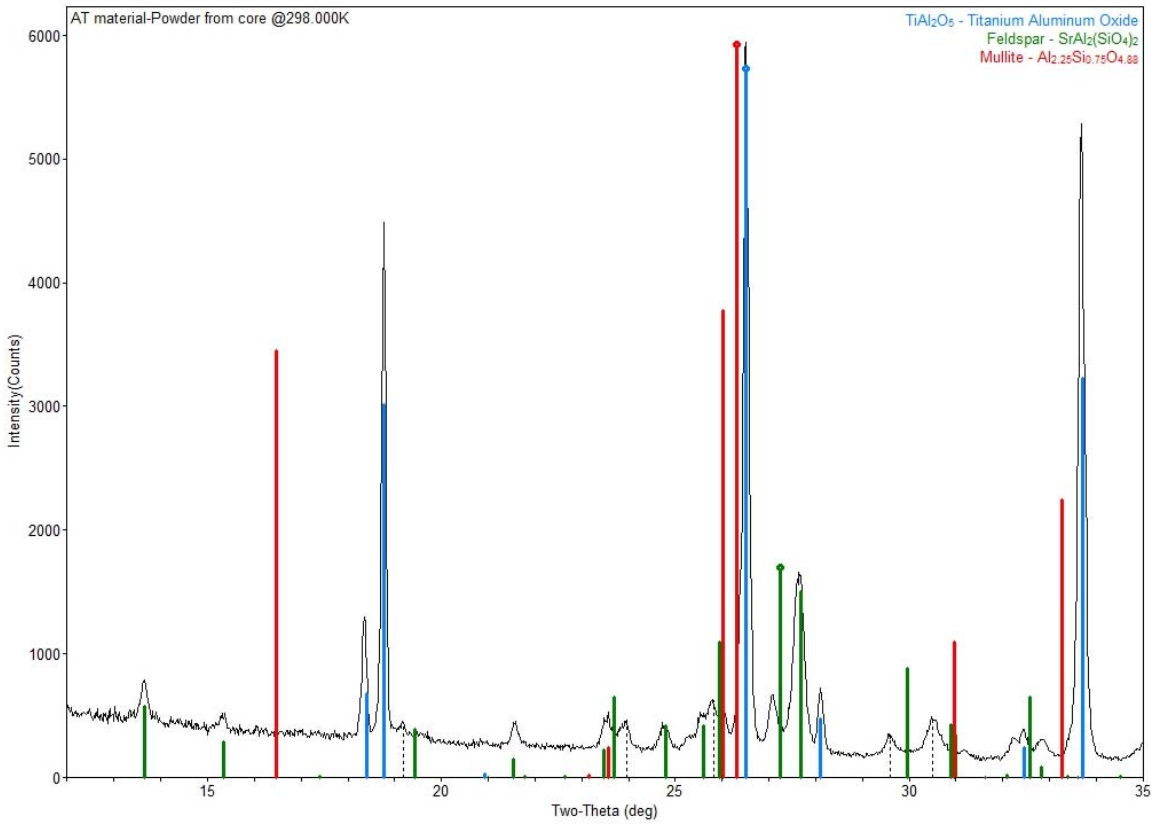

Figure 3 – The X-ray diffraction pattern the Al_2TiO_5-based DPF material.

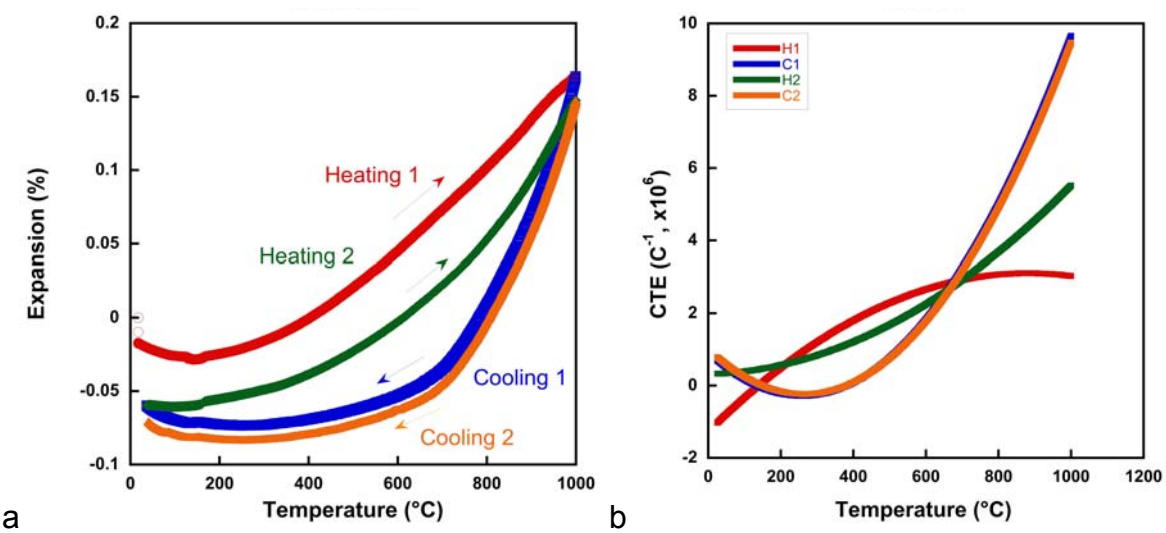

a b

Figure 4 – The expansion (left) and thermal expansion coefficient (right) curves as a function of temperature of Al_2TiO_5-based DPFs.

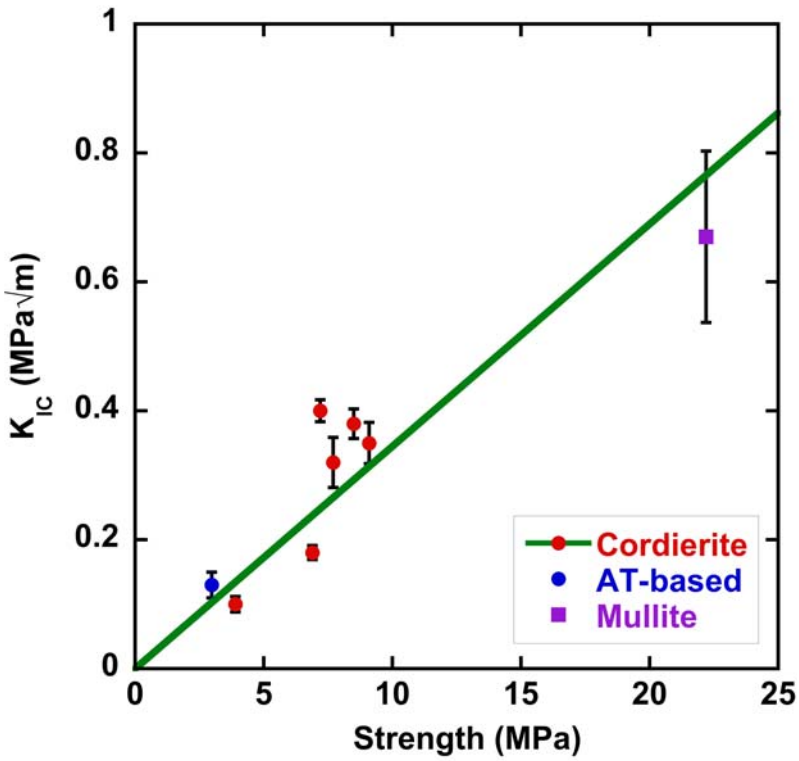

Figure 5 – The fracture toughness as a function of strength for three DPF materials.

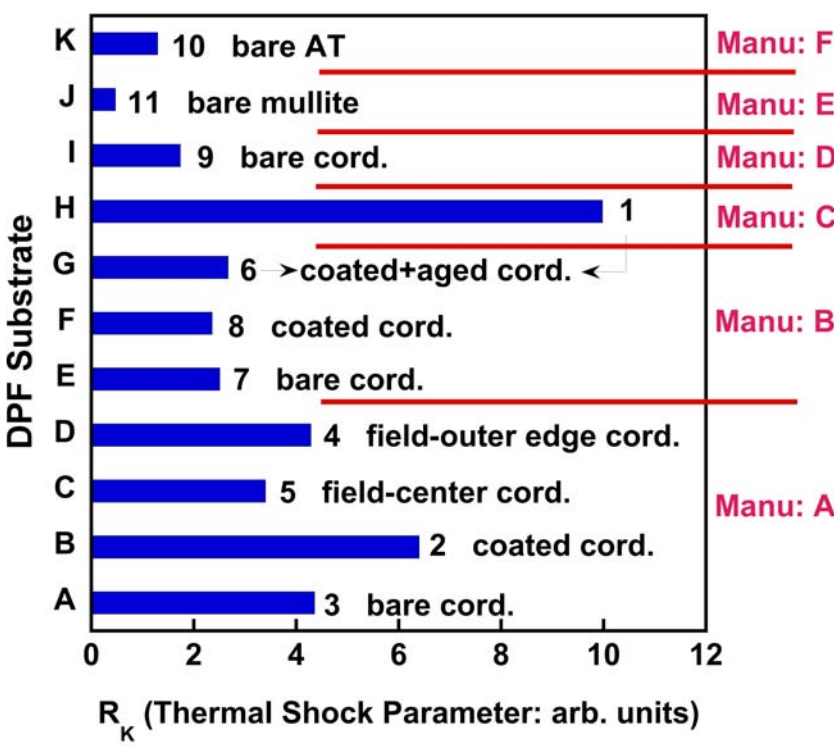

Figure 6 – The thermal shock parameter, R_K, for the various DPF examined.

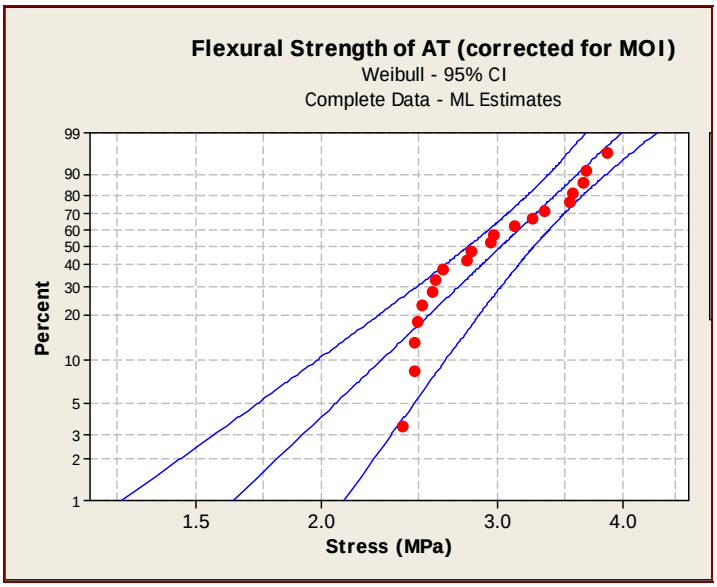

Figure 7 – The Weibull plot for the flexural strengths of Al_2TiO_5-based honeycombs corrected for the moment of inertia.

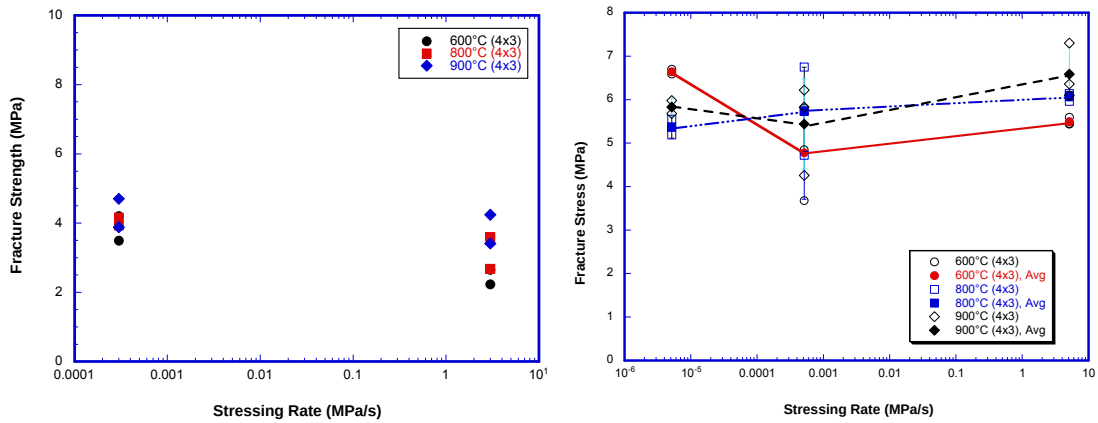

Figure 8 – The flexural strength as a function of stressing rate and temperature for the Al_2TiO_5-based (left) and cordierite (right) DPFs.

Agreement 10635: Catalysis by First Principles - Can Theoretical Modeling and Experiments Play a Complimentary Role in Catalysis?

C. Narula, M. Moses DeBusk, Xiaofan Yang
Oak Ridge National Laboratory

Objective/Scope

This research focuses on an integrated approach between computational modeling and experimental development, design and testing of new catalyst materials, that we believe will rapidly identify the key physiochemical parameters necessary for improving the catalytic efficiency of these materials. The results will have direct impact on the optimal design, performance, and durability of supported catalysts employed in emission treatment; e.g., lean NO_x catalyst, three-way catalysts, oxidation catalysts, and lean NO_x traps etc.

The typical solid catalyst consists of nano-particles on porous supports. The development of new catalytic materials is still dominated by trial and error methods, even though the experimental and theoretical bases for their characterization have improved dramatically in recent years. Although it has been successful, the empirical development of catalytic materials is time consuming and expensive and brings no guarantees of success. Part of the difficulty is that most catalytic materials are highly non-uniform and complex, and most characterization methods provide only average structural data. Now, with improved capabilities for synthesis of nearly uniform catalysts, which offer the prospects of high selectivity as well as susceptibility to incisive characterization combined with state-of-the science characterization methods, including those that allow imaging of individual catalytic sites, we have compelling opportunity to markedly accelerate the advancement of the science and technology of catalysis.

Computational approaches, on the other hand, have been limited to examining processes and phenomena using models that had been much simplified in comparison to real materials. This limitation was mainly a consequence of limitations in computer hardware and in the development of sophisticated algorithms that are computationally efficient. In particular, experimental catalysis has not benefited from the recent advances in high performance computing that enables more realistic simulations (empirical and first-principles) of large ensemble atoms including the local environment of a catalyst site in heterogeneous catalysis. These types of simulations, when combined with incisive microscopic and spectroscopic characterization of catalysts, can lead to a much deeper understanding of the reaction chemistry that is difficult to decipher from experimental work alone.

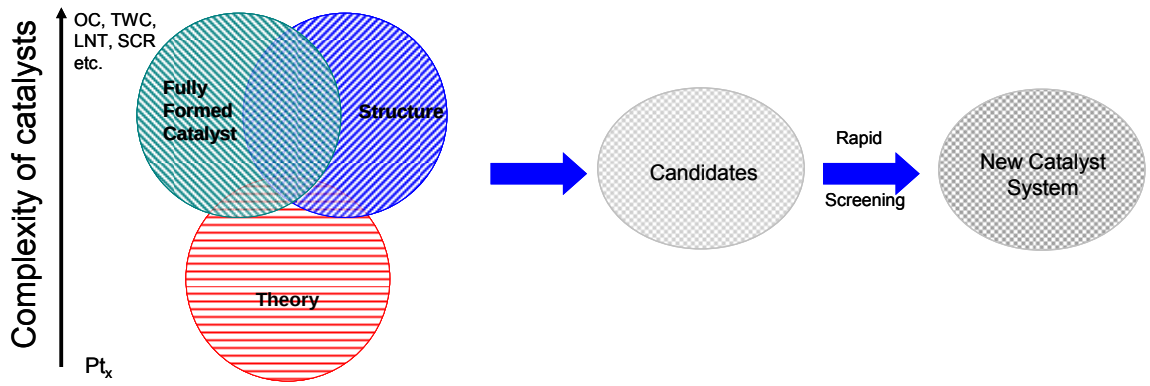

Thus, a protocol to systematically find the optimum catalyst can be developed that combines the power of theory and experiment for atomistic design of catalytically active sites and can translate the fundamental insights gained directly to a complete catalyst system that can be technically deployed.

Although it is beyond doubt computationally challenging, the study of surface, nanometer-sized, metal clusters may be accomplished by merging state-of-the-art, density-functional-based, electronic-structure techniques and molecular-dynamic techniques. These techniques provide accurate energetics, force, and electronic information. Theoretical work must be based on electronic-structure methods, as opposed to more empirical-based techniques, so as to provide realistic energetics and direct electronic information.

A computationally complex system, in principle, will be a model of a simple catalyst that can be synthesized and evaluated in the laboratory. It is important to point out that such a system for experimentalist will be an idealized simple model catalyst system that will probably model a “real-world” catalyst. Thus it is conceivable that “computationally complex but experimentally simple” systems can be examined by both theoretical models and experimental work to forecast improvements in catalyst systems.

We have focused on the oxidation catalyst to develop and demonstrate catalyst by design protocol as a prelude to developing catalyst by design protocols for complex emission treatment catalysts; e.g., TWCs, NO_x traps, and HC-SCR catalysts. Our goals are as follows:

- Our theoretical goal is to carry out the calculation and simulation of realistic supported Pt nanoparticle systems (i.e., those equivalent to experiment), in particular by addressing the issues of complex cluster geometries on local bonding effects that determine reactivity. As such, we expect in combination with experiment to identify relevant clusters, and to determine the electronic properties of these clusters.
- Our experimental goal is to synthesize metal carbonyl clusters, decarbonylated metal clusters, sub-nanometer metal particles, and metallic particles (~5 nm) on alumina (commercial high surface area, sol-gel processed, and mesoporous molecular sieve), characterize them employing modern techniques including

Aberration Corrected Electron Microscope (ACEM), and evaluate their CO, NO_x, and HC oxidation activity.

- This approach will allow us to identify the catalyst sites that are responsible for CO, NO_x, and HC oxidation. We will then address support-cluster interaction and design of new durable catalysts systems that can withstand the prolonged operations.

Technical Highlights

Our theoretical studies on single platinum atoms supported on θ-alumina slab shows that the platinum atom is in the zero oxidation state. This result is very different from that reported in literature on single platinum atoms supported on α-alumina or simplified models of γ-alumina where a platinum atom generally has an unpaired electron. This also means that mechanism of CO, NO_x, or HC oxidation on Pt(0) will be different from that on Pt(I) or Pt(II). We plan to carry out first principle studies of CO oxidation on Pt atoms supported on θ-alumina slab.

Since our experimental work has already shown that the distribution of platinum on γ-alumina and θ-alumina is almost identical, and the surface properties and CO oxidation of both catalysts are identical, we propose that Pt supported on θ-alumina is a better model for Pt supported on γ-alumina than Pt supported on α-alumina or simplified models of γ-alumina.

Our next step involves substitution of platinum atoms from agglomerates with palladium to understand the energetics of the system that will enable us to synthesize more durable catalysts than the current generation of catalysts.

Theoretical Studies

We have previously summarized the results on DFT calculation of bulk θ-alumina, θ-alumina slab, and a single platinum atom on a θ-alumina slab. We also reported preliminary results on a charge neutral supercell of 420 atoms combining 2 x 3 x 3 cells and found the location of platinum to optimize in an environment identical to the one in 180-atom supercell. We also optimized the single Pd, Ag, or Au atom adsorbed on the [010] surface of θ-alumina and found the adsorption energies for Pt, Pd, Au, and Ag are in the order of Pt>Pd>Au>Ag and are -62.29, -44.84, -20.21, and -13.23 Kcal/mole, respectively suggesting that the absorption of these atoms is exothermic.

We also summarized local density of state [LDOS] analysis of Pt/θ-Al2O3 which showed the Pt is zero oxidation state. The implication of this important result is that the mechanism of CO, NO, or HC oxidation on sub-nanometer particles such as single atoms should be different from the large particles normally examined by DFT. We also summarized preliminary results on DFT structural studies of 2-atom and larger clusters of Platinum on a charge neutral supercell of 420 atoms combining 2 x 3 x 3 cells. Since 2x3x3 cell has four identical sites, we initiated our study of 2- and 4- Pt atoms on the surface with no bonding interaction with Pt atoms.

We also calculated the energy barrier between two-independent platinum atoms and two-bonded platinum atoms on 010 θ-alumina surfaces and found the two-independent configuration favored by 1.27 Kcal/mole. Thus, the energetics does not seem to favor Pt clustering. Thus, the preliminary studies summarized here suggest that the platinum atoms prefer independent locations where they are in zero oxidation state and are bonded to two neighboring oxygen atoms. The agglomerates of platinum also do not exhibit Pt-Pt interaction. An important implication of this study is on the mechanism of CO or NOx oxidation.

In this report, we describe our results on Pd, Au, and Ag atoms supported on θ-alumina surface. We also present our results on Pt-Pd clusters.

The configuration of a palladium atom is $d^{10}s^{0}$, and it has higher energy valence d and s states than those for platinum. For Pd atoms, the Pd-O bond distances are 2.227 Å and 2.201 Å with an O-M-O angle of 134.54º. The distance from sub-surface Al is 2.49 Å and the Pd atom sits 0.86 Å above the cell surface. As expected, these distances are slightly larger that those for platinum atom but the bonding are identical to Pt atoms. For Au atoms, the Au-O bond distances are 2.45 Å and 2.69 Å with an O-M-O angle of 107.34º. The distance from sub-surface Al is 2.976 Å and nearest surface Al is 2.706 Å. The Au atom sits 1.519 Å above the cell surface. The Ag-O bond distances for Ag/θ-alumina are 2.483 and 2.549 Å with an O-Ag-O angle of 108.5º. The distance from sub-surface Al is 3.08 Å and from closest surface Al is 3.09 Å. Both Ag and Au are $d^{10}s^{1}$ atoms and the energy of their valence d and s orbitals are lower that that of valence orbitals of Pt. There is a magnetic moment of 1.0 associated with Au and Ag atoms and magnetization is primarily in s orbitals of Au and Ag. The LDOS of Au (Figure 1) show filled 5d-orbitals while supporting the fact that magnetization originates from unpaired electron in Au-s orbital. There is small magnetization transfer to both neighboring oxygen which are bonded to

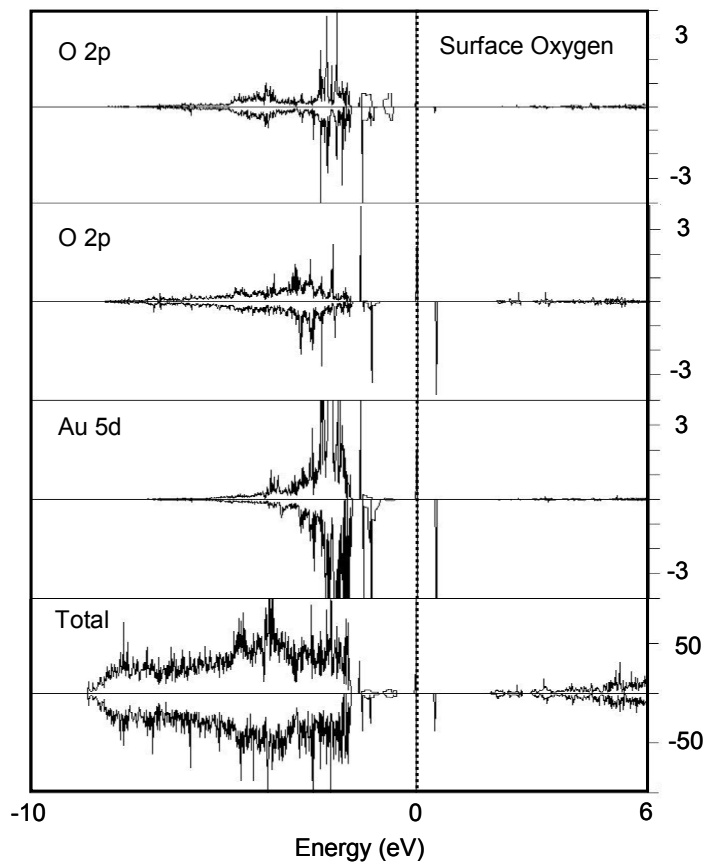

Figure 1: Selected Density of States plots for Au/ θ-Al_2O_3

the Au atom. There is no interaction with the Al atom below the Au atom which is not within bonding distance to Au.

We have also carried out preliminary study of Pt-Pd clusters supported on 010 θ-alumina surfaces. Replacement of one platinum atom with one palladium atom in each of the three models shown in Figure 2 did not lead to any difference in the optimized structure.

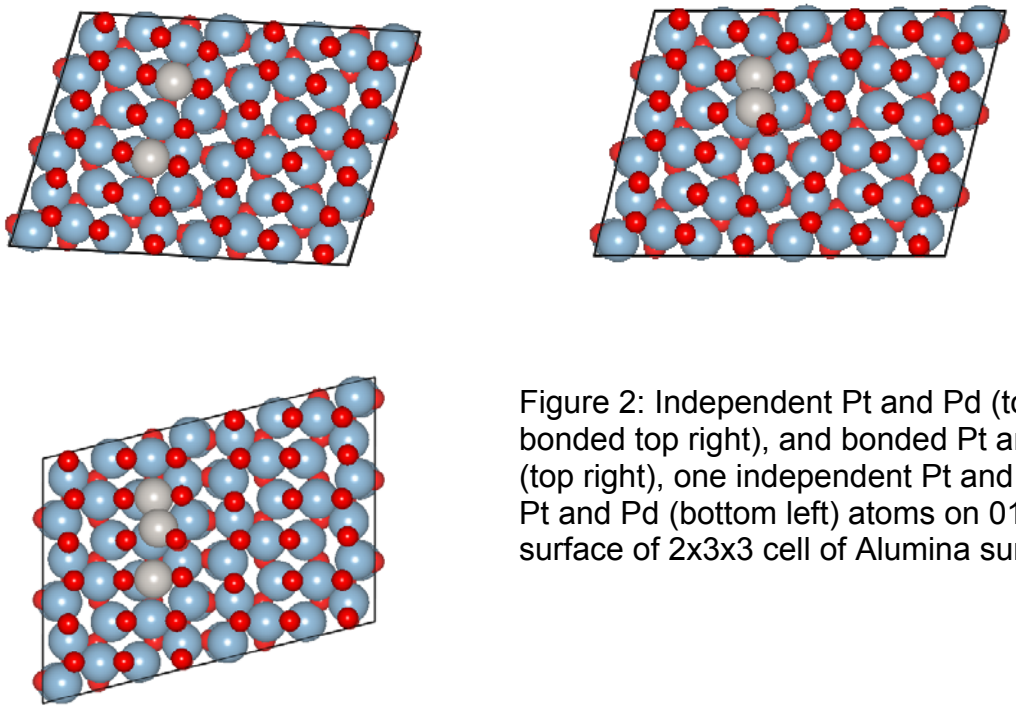

Figure 2: Independent Pt and Pd (top left), bonded top right), and bonded Pt and Pd (top right), one independent Pt and bonded Pt and Pd (bottom left) atoms on 010 surface of 2x3x3 cell of Alumina surface

As expected, the Pt-O bond distances are 2.192 and 2.13Å which is identical to single Pt atom on 101 surface of 2x3x3 alumina cell. The Pd-O distances are 2.24 and 2.2 Å which are also identical to single Pd atom on 101 surface of 2x3x3 alumina cell. When the second atom (Pt or Pd) is bonded to the first Pt atom, the Pt-O bond distances decrease slightly indicating stronger interaction of first platinum with alumina surface oxygens. The bond distances of second Pt or Pd atom to first Pt atom are 2.489 and 2.57 Å, respectively. The independent configuration of both Pt atoms is favored by 1.27 Kcal/mole over the bonded configuration. The independent configuration of Pt and Pd atoms is favored by 0.6 Kcal/mole over the Pt-Pd bonded configuration. In other words, there is no significant energy benefit between bonded or independent configurations. A very similar behavior is observed for three atom clusters in bonded (Figure 2) and independent configurations.

These observations are not surprising but do not explain hydrothermal durability of Pt-Pd nanoclusters over Pt-Pt nanoclusters as described in the experimental section. We

have initiated a study of Pt/PdO clusters on 010 Alumina surface to gain insights and the results will be presented in the next report.

Experimental Studies

In order to compare the results of theoretical studies on palladium substituted platinum agglomerates, we have synthesized and characterize platinum-palladium agglomerates supported on γ-alumina substrates.

We followed the procedure described by Toshima *et al.* (J. Chem. Soc. Faraday Trans., 1993, 89, 2537-2543) for the synthesis of homogeneous Pd-Pt nanoclusters with different Pt:Pd ratios, around 1.5 nm, employing poly(N-vinyl-2-pyrrolidone) (PVP, average MW 40,000) to stabilize nanoparticles.

Pd-Pt (1:4) on Al_2O_3 – PVPPdPt14: $PdCl_2$ (0.0160 g, 0.090 mmol) was dissolved in 170 mL ethanol and filtered after 24h stirring followed and 1.003 g PVP40 was added to the filtrate A water solution (170 mL) of hexa-chloroplatinic(IV) acid (0.171 g, 0.368 mmol) and 1.003 g PVP was added to the Pd ethanol solution. The combined yellow ethanol/water solution was refluxed for an hour, resulting in a dark brown transparent solution. 4 g γ-Al_2O_3 was added to the resulting dark brown solution. The slurry was stirred for 48 hours, centrifuged, and washed to obtain grey powder. The grey powder was dried at room temperature (overnight), and calcined at 350°C for 1 hour (1°C /min).Elemental Analysis shows a Pd to Pt ratio of 0.22: Pd 0.06%, Pt 0.52%.

Pd-Pt (1:1) on Al_2O_3 – PVPPdPt11: $PdCl_2$ (0.0471 g, 0.265 mmol) was dissolved in 200 mL ethanol and filtered after 24 h stirring and 1.180 g PVP40 was added to the filtrate. A water solution (200 mL) of hexa-chloroplatinic(IV) acid (0.125 g, 0.269 mmol) and 1.180 g PVP was added to the Pd ethanol solution. The combined yellow ethanol/water solution was refluxed for an hour, resulting in a dark brown transparent solution. 4 g γ-Al_2O_3 was added to the resulting dark brown solution. The slurry was stirred for 48 hours, centrifuged, and washed to obtain grey powder. The grey powder was dried at room temperature (overnight), and calcined at 350°C for 1 hour (1°C/min). Elemental Analysis shows a Pd to Pt ratio of 0.86: Pd 0.52%, Pt 0.43%.

Pd-Pt (4:1) on Al_2O_3 – PVPPdPt41: $PdCl_2$ (0.0914 g, 0.515 mmol) was dissolved in 240 mL ethanol and filtered after 24h stirring 1.432 g PVP40 was added to the filtrate. A water solution (240 mL) of hexa-chloroplatinic(IV) acid (0.060 g, 0.129 mmol) and 1.432 g PVP was added to the Pd ethanol solution. The combined yellow ethanol/water solution was refluxed for an hour, resulting in a dark brown transparent solution. 4 g γ-Al_2O_3 was added to the resulting dark brown solution. The slurry was stirred for 48 hours, centrifuged, and washed to obtain grey powder. The grey powder was dried at room temperature (overnight), and calcined at 350°C for 1 hour (1°C/min). Elemental Analysis shows a Pd to Pt ratio of 3.77: Pd 0.59%, Pt 0.64%.

The TEM images of all three PdPt nanoclusters supported on θ-alumina together with their statistical size distribution curve are shown in Figure 3. The size distributions of all

three PdPt nanocluster species exhibit a distribution in 1-6 nm range and are centered at 2.5 nm.

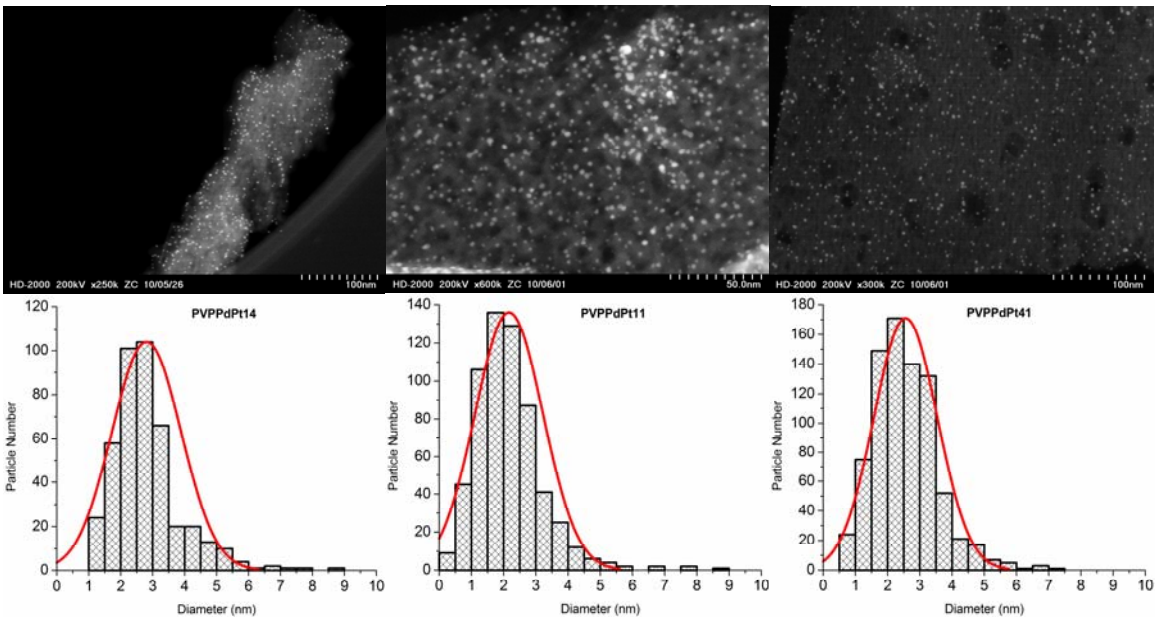

Figure 3: TEM of Pd-Pt (1:4) (left), Pd-Pt (1:1) (middle), and Pd-Pt (4:1) (right) on γ-Al_2O_3

Hydrothermal aging of supported Pt-Pd nanoclusters: All three samples were subjected to hydrothermal aging protocol reported by Graham et al (Catalysis Letters, 2007, 116, 1-8). A 0.7 g of PdPt/alumina sample was treated under a flow (5L/min) of N_2, O_2 (5%) and H_2O (10%) for 3 hours at a series of temperatures (500°C, 600°C, 750°C and 900°C), held for 2.5 hours, and cooled under pure N_2.

The TEM studies of aged PVPPdPt41 (Figure 4) samples show that particle size grows gradually as temperature increases. After aging at 500°C, the particles had grown somewhat with distribution now centered at 3.5 nm. Aging at 600°C and 750°C led to rapid growth in the size of and distribution centered at ~7 nm and ~ 14 nm respectively were observed. The increase in aging temperature to at 900°C results in drastic increase in particle size with distribution centered at ~35 nm.

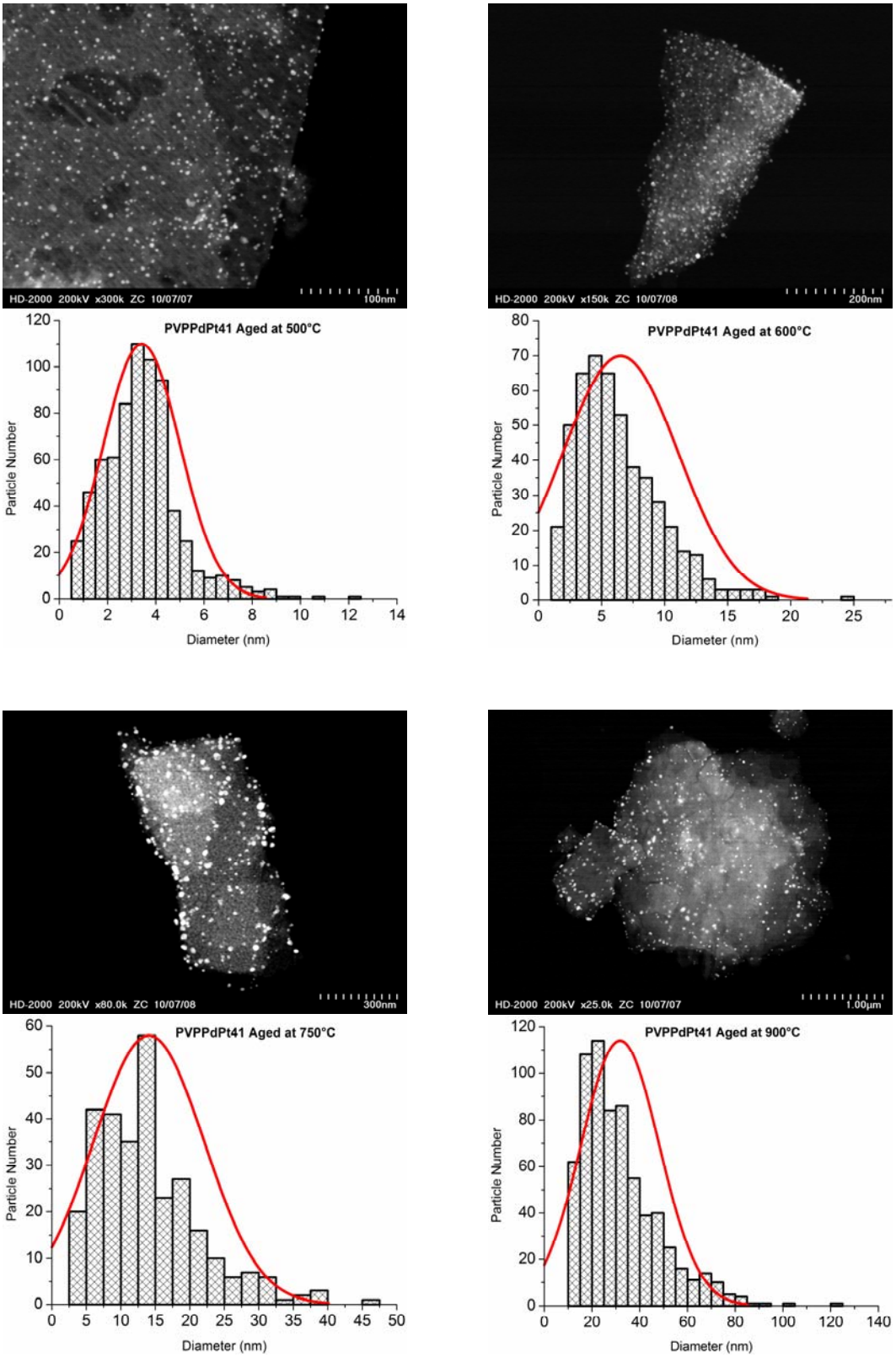

Figure 4: TEM Pd-Pt (4:1) on γ-Al_2O_3 after hydrothermal aging after aging at 500, 600, 750, and 900C.

We are synthesizing trans-[(NH3)2Pt(C5H6N3O)2PdCl](NO3)•H2O (Lippert et al., J. Am. Chem Soc., 113 (1991) 5129) which contains Pt-Pd bond to prepare subnanometer Pt-Pd agglomerates on alumina.

Next Steps: We plan to carry out the following tasks:

- We will carefully characterize palladium substituted platinum agglomerates and study their durability under CO, HC, and NO_x oxidation conditions and diesel emissions treatment conditions.
- Complete theoretical calculations on 10-20 atom platinum clusters supported on θ-alumina surface.
- Initiate CO oxidation theoretical studies on platinum single atoms supported on θ-alumina surface.

Other Activities

A joint project on lean NO_x treatment is on going with John Deere Co. under work for others arrangement.

Communication/Visitors/Travel

Our paper titled "First-Principles and Experimental Studies of the Sub-Nanometer Platinum Atoms Supported on θ-Alumina" has been accepted for presentation at ACS National Meeting in Boston. We have also submitted an article titled "Zero oxidation state platinum atom supported on θ-alumina" to Nature Materials.

Publications

1. C.K. Narula, X. Chen, M.G. Stocks, Zero oxidation state platinum atom supported on θ-alumina, Nature Materials, (submitted)
2. C.K. Narula, "Catalyst by Design – Bridging the Gap between Theory and Experiments at Nanoscale Level" Encyclopedia of Nanoscience and Nanotechnology, Vol. II, Taylor & Francis, New York, 2008, pp 771-782 (invited).
3. C.K. Narula, L.F. Allard, D.A. Blom, M. Moses-DeBusk, "Bridging the Gap between Theory and Experiments – Nano-structural Changes in Supported Catalysts under Operating Conditions" SAE-2008-01-0416, SAE Int. J. Mater. Manu., 1(2008) 182-188.
4. C.K. Narula, L.F. Allard, D.A. Blom, M.J. Moses, W. Shelton, W. Schneider, Y. Xu, "Catalysis by Design - Theoretical and Experimental Studies of Model Catalysts", SAE-2007-01-1018 (invited).
5. C.K. Narula, M.J. Moses, L.F. Allard, "Analysis of Microstructural Changes in Lean NO_x Trap Material Isolates Parameters Responsible for Activity Deterioration" SAE 2006-01-3420.
6. Y. Xu, W.A. Shelton, and W.F. Schneider, "The thermodynamic equilibrium compositions, structures, and reaction energies of Pt*x*O*y* (*x* = 1-3) clusters predicted from first principles," *Journal of Physical Chemistry B,* 110 (2006) 16591.
7. Y. Xu, W. A. Shelton, and W. F. Schneider, "Effect of particle size on the oxidizability of platinum clusters," *Journal of Physical Chemistry A*, 110 (2006) 5839.
8. C.K. Narula, S. Daw, J. Hoard, T. Hammer, "Materials Issues Related to Catalysts for Treatment of Diesel Exhaust," *Int. J. Amer. Ceram. Tech*., 2 (2005) 452 (invited).

Presentations (last 12 months)

1. Narula, C.K.; Chen, X.; Stocks, G.M., DeBusk, M.M.; Allard, L.F.; “First-Principles and Experimental Studies of the Sub-Nanometer Platinum Atoms Supported on θ-Alumina” 230th American Chemical Society Meeting, Boston, MA, August 22-26, 2010.
2. Narula, C.K.; Chen. X.; Stocks, M.G.; “First-Principles Studies of the Structure and Bonding of Metal Atoms Supported on θ-Alumina,” 229th American Chemical Society Meeting, San Francisco, CA, March 21-25, 2010.
3. Moses-DeBusk, M.; Narula, C.K. "Catalyst by design: Combining the power of theory, experiments, and nanostructural characterization for catalyst development," 227th National American Chemical Society Meeting, March 2009 (invited).
4. Narula, C.K.; DeBusk, M.M.; Allard, L.F.; “Catalyst by Design – Theoretical, Nanostructural, and Experimental Studies of Oxidation Catalyst for Diesel Engine Emission Treatment, DEER 2009, Detroit, MI.

Agreement 19214: Effects of Biodiesel Fuel on Diesel Particulate Filter Materials

M. J. Lance, T. J. Toops, S. A. Lewis, J.M.E. Storey and R. M. Connaster
Oak Ridge National Laboratory

Objective/Scope

To characterize changes in the microstructure and material properties of commercial diesel particulate filters (DPFs) in exhaust gas produced by biodiesel blends.

Technical Highlights

Chemical Analysis: Condensates were collected from the exhaust of ULSD (B0) and B20 fuels run on an air-cooled light duty, single cylinder Haatz engine at half and full loads. The condensates were titrated for acid content. Results show that the nitric and acetic acid levels were comparable for both fuels. However, B20 exhaust has significantly higher concentrations of sulfuric and formic acids as compared to the conventional diesel exhaust at both half and full load. For nitric acid, B20 exhaust had a 29% increase at half load and 119% increase at full load as compared to ULSD fuel. For sulfuric acid, the increase was much more dramatic, 96% and 263% for half and full load, respectively.

	ug in 100 uL of condensate			
	nitric acid	**sulfuric acid**	**formic acid**	**acetic acid**
ULSD				
half load	10.4	28	8.9	3.1
full load	7.4	46.3	18	6.8
B20				
half load	7.7	36.2	17.4	3.9
full load	7.4	101.3	65.3	6.1

Additional samples (1”x3” DPFs) are undergoing investigation during Q4.

New Samples: Four fuels, ULSD, B5, B20 and B100 were investigated at a single operating point (1500 rpm, 2.6 bar BMEP) on a light duty, late model Mercedes engine. Condensate was collected for each sample from the raw exhaust. These condensates will be titrated in Q4 for acid content, increasing the scope of biofuel blends considered in this study.

Status of FY2010 Milestones

Measure the chemical composition and pH of condensate and PM generated by a diesel engine running with ULSD and biofuel blends. (09/10) *On Schedule.*

Communications/Visits/Travel

None.

Problems Encountered
None.

Publications/Presentations/Awards
None.

References
None.

Agreement 20091: Electrically Assisted DPF Material

M. J. Lance, A. A. Wereszczak, J. E. Parks, and W. P. Partridge
Oak Ridge National Laboratory

Objective/Scope

In this CRADA project with General Motors (GM), two research objectives are being pursued:

1. Analysis of diesel particulate filter (DPF) substrate materials to understand crack and failure mechanisms and resolve current differences in simulation and experimental results.
2. Measure of substrate temperatures during DPF regeneration with optically based techniques that are not susceptible to conductive interferences that are problematic for common thermocouple technologies.

Technical Highlights

DPF Mechanical Evaluation

Several test coupon geometries were conceived and harvested out of a DPF with the intention to mechanically load them to failure to estimate failure stresses as a function of applied tensile stress direction and as a function of location within the interior or on the exterior of a DPF. The basic geometry of each have been used in other brittle materials applications to measure failure stress, and are adapted here with DPFs to judge their viability at candidate test specimens.

Biaxial flexure testing of disks will subject the tensile side of the specimen to an equibiaxial radial tensile stress. Such testing is featured in ASTM C1499 [1]. Such testing is underway on disks machined from the two ends of a DPF (Fig. 1) and from the DPF interior (Fig. 2).

Vertically oriented diametral compressive loading of an o-ring specimen geometry (Fig. 3) will subject the outer diameter to hoop tension at the 3 and 9 o'clock positions and subject the inner diameter to hoop tension at the 6 and 12 o'clock positions. The weakest of those four locations will cause failure and its failure stress will be noted. This test method was developed a while ago to measure failure stress in ceramic tubes [2-3].

Testing the sectored flexure specimen [4] in 4-pt flexure will subject the exterior of the DPF to an axial tensile stress. An illustration of that specimen in shown in Fig. 4.

The theta specimen [5] can be an effective test method to measure radial tensile failure stress. Its geometry [Fig. 5] requires careful machining, and will likely be dismissed in favor of the simpler biaxial flexure testing.

Mechanical testing of these geometries, and the evaluation of their failure stresses via supportive finite element analysis is now underway.

Optically based DPF Substrate Temperature Measurement
Efforts have begun for bench top development of the optically based temperature measurement technique. Blackbody radiation will be collected with fiber optic probes to measure temperature. A new Intensified Charge Coupled Device (ICCD) camera with spectrometer attached has been acquired and commissioned for use in the project. Calibration and data acquisition software customization for the engine-based experiments will continue in the next quarter as well as development of the fiber optic probes.

Interactions have begun between GM and ORNL to enable ORNL to operate GM's DPF technology for experiments in ORNL's engine dynamometer research cell. GM is producing hardware that will be installed on an existing GM 1.9-liter 4-cylinder diesel engine at ORNL.

Status of FY 2010 Milestones
Task 1.a. Electrically-heated DPF installed and operational (desoot event conducted successfully). (09/10) *Delayed - GM still fabricating prototype unit for installation at ORNL. Installation will commence when received at ORNL.*

Task 2.a. Identify and characterize failure initiation locations of cracked EHDPFs **(08/10)**. *On schedule.*

Task 2.b. Design test coupons harvestable from EHDPFs and whose testing will produce material, size-dependent, failure stress data for input for durability analysis and prediction **(09/10).** *On schedule.*

Communications/Visits/Travel
1. ORNL's W. Partridge and J. Parks visited GM in the Detroit area to observe the existing DPF system in an engine dynamometer lab and discuss hands-on details about operation of the device (April 2010).
2. A CRADA kickoff meeting with GM and ORNL was held in Oak Ridge, TN. DOE program manager Jerry Gibbs was in attendance (May 2010).

Problems Encountered
GM still fabricating prototype unit that is causing a delay in its installation at ORNL.

Publications/Presentations/Awards
None.

References

[1] "Standard Test Method for Monotonic Equibiaxial Flexural Strength of Advanced Ceramics at Ambient Temperature," ASTM C1499, Vol. 15.01, ASTM International, West Conshohocken, PA, 2009.

[2] O. M. Jadaan, D. L. Shelleman, J. C. Conway, Jr., J. J. Mecholsky, Jr., and R. E. Tressler, "Prediction of the Strength of Ceramic Tubular Components: Part I - Analysis," *Journal of Testing and Evaluation*, 19:181-191 (1991).

[3] D. L. Shelleman, O. M. Jadaan, J. C. Conway, Jr., and J. J. Mecholsky, Jr., "Prediction of the Strength of Ceramic Tubular Components: Part II - Experimental Verification," *Journal of Testing and Evaluation*, 19:192-200 (1991).

[4] A. A. Wereszczak, S. F. Duffy, E. H. Baker, J. J. Swab, and G. J. Champoux, "Strength of a Ceramic Sectored Flexural Test Specimen," *Journal of Testing and Evaluation*, 36:17-23 (2008).

[5] G. D. Quinn, E. Fuller, D. Xiang, A. Jillavenkatesa, L. Ma, D. Smith, and J. Beall, "A Novel Test Method for Measuring Mechanical Properties at the Small-Scale: The Theta Specimen," *Ceramic Engineering and Science Proceedings*, [2] 23:117-126 (2005).

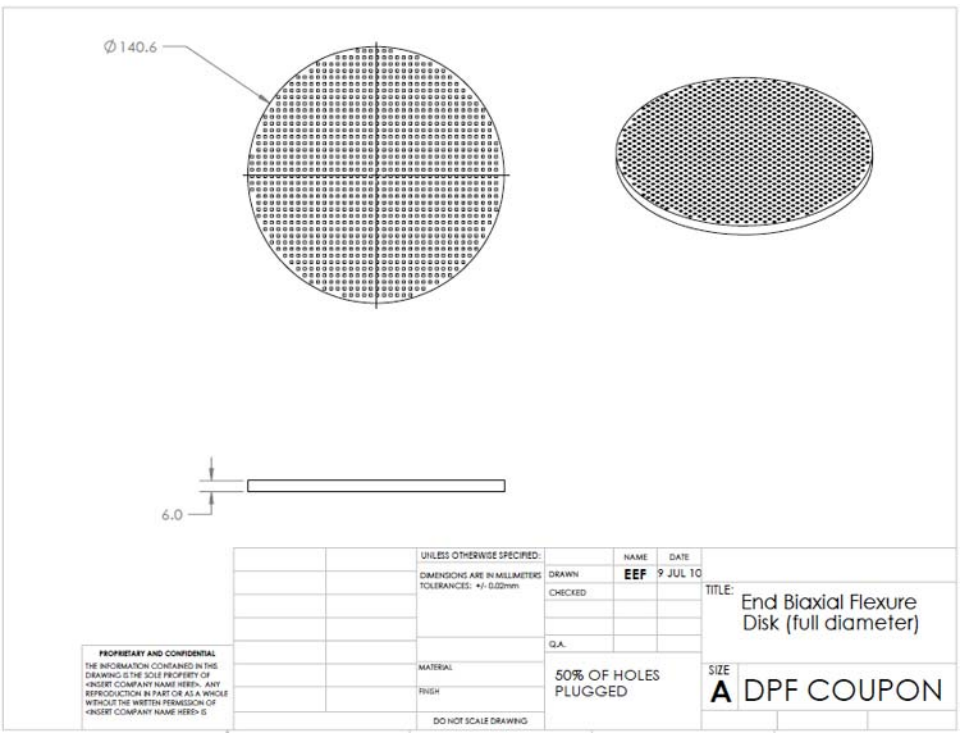

Figure 1. Biaxial flexure disk harvested from the two ends of a DPF.

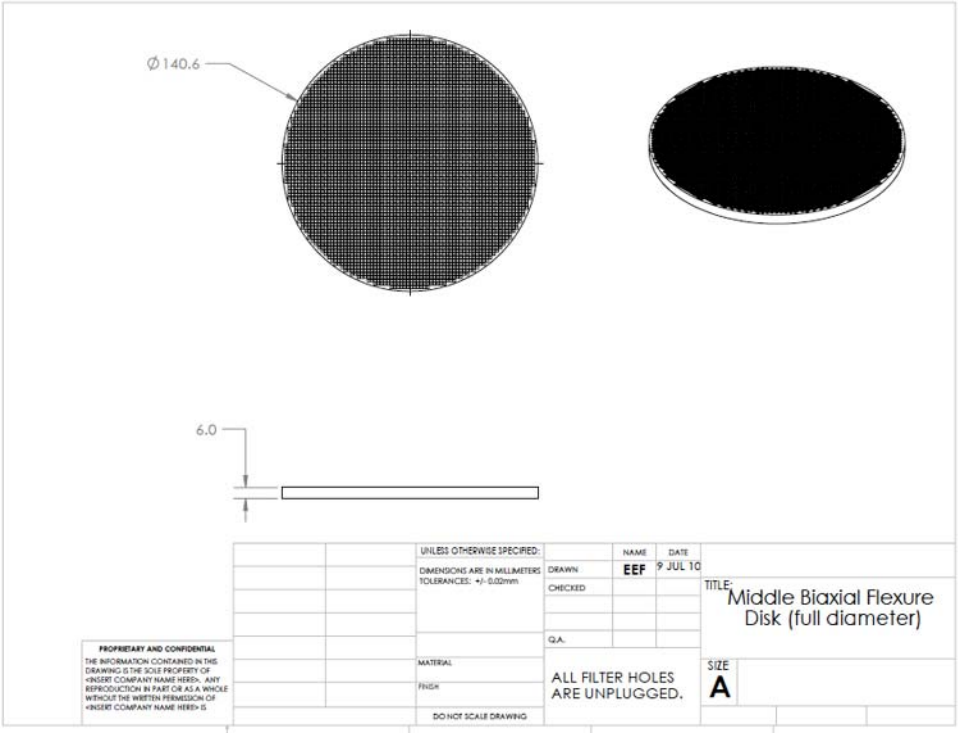

Figure 2. Biaxial flexure disk harvested from the interior of a DPF.

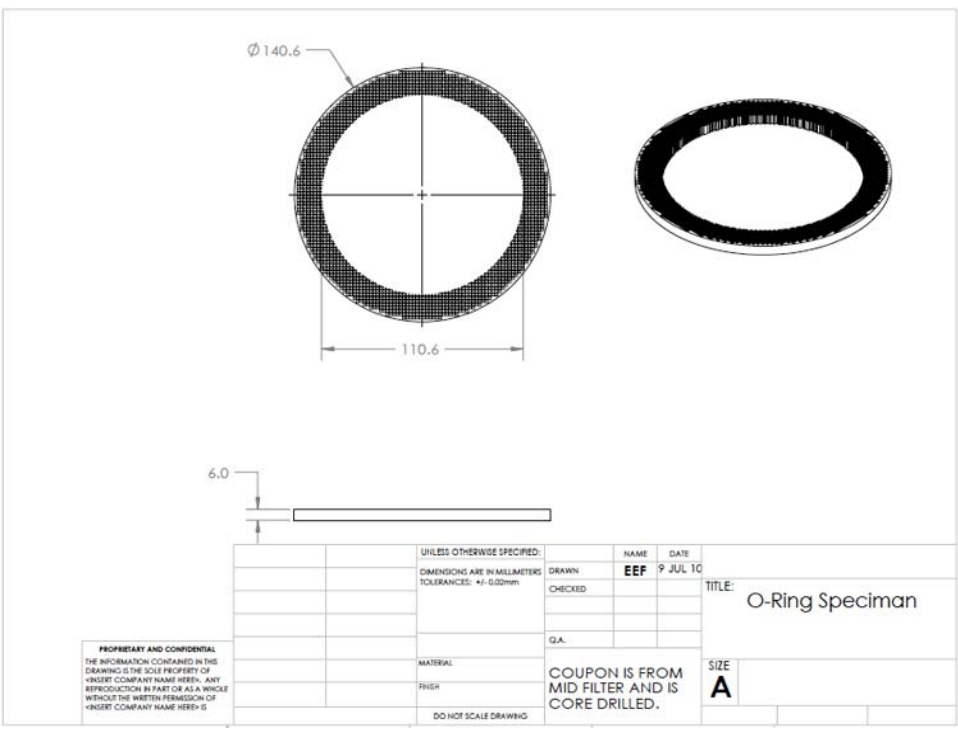

Figure 3. O-ring specimen geometry.

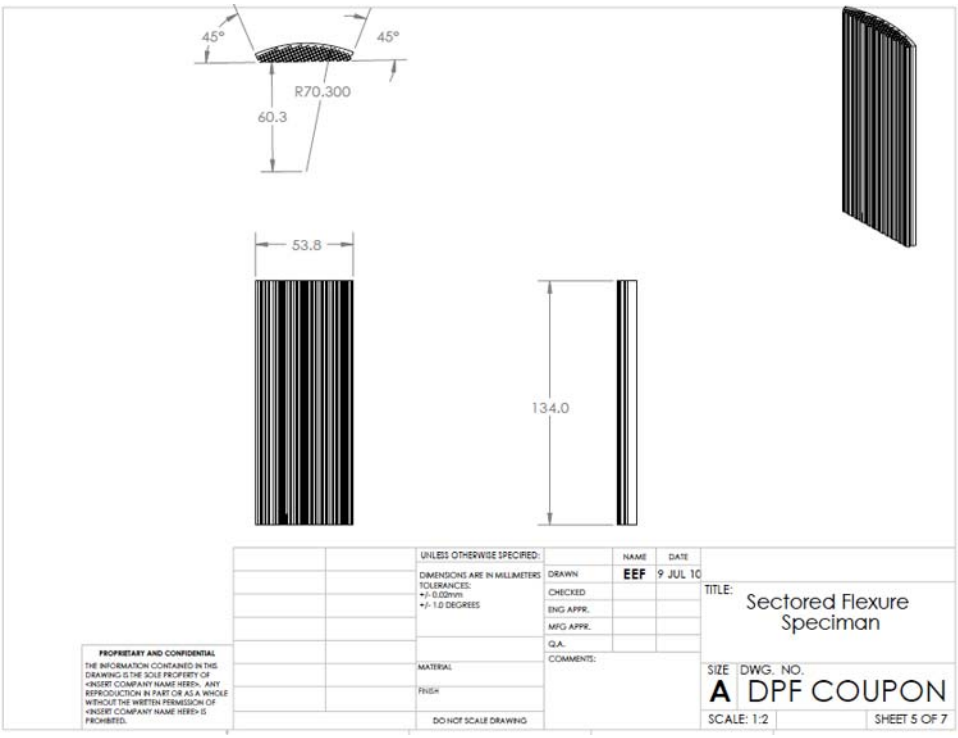

Figure 4. Sectored flexure specimen geometry.

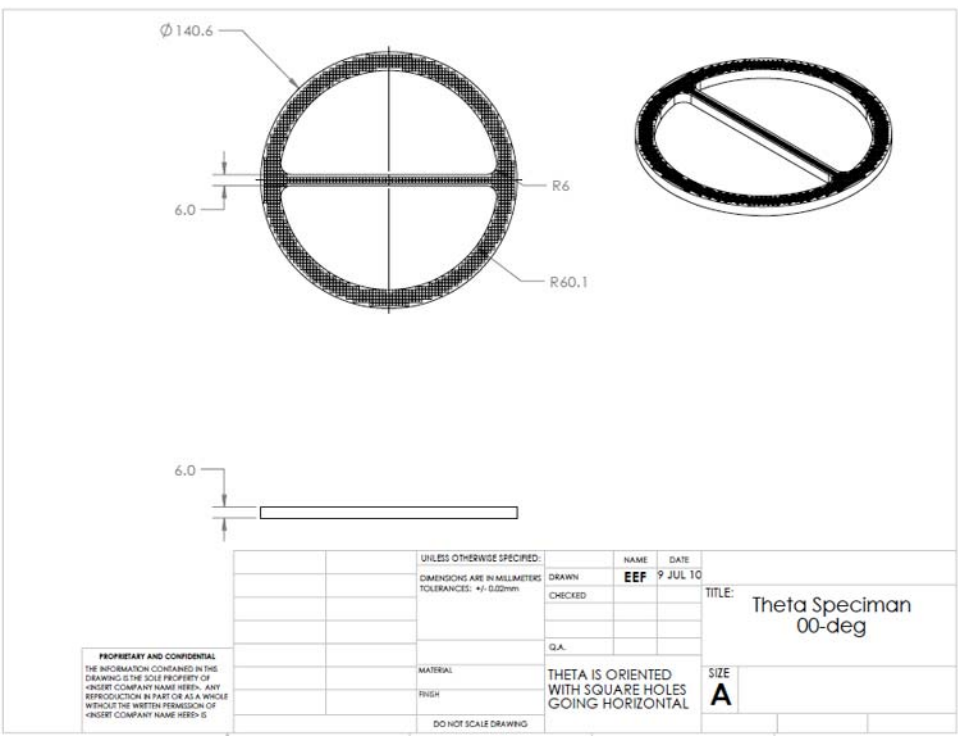

Figure 5. Theta specimen geometry.

Agreement 9105: Ultra-High Resolution Electron Microscopy for Characterization of Catalyst Microstructures and Reaction Behavior

L.F. Allard, C.K. Narula, W.C. Bigelow, J. Liu, D.P. Nackashi and J. Damiano
Oak Ridge National Laboratory

Objective/Scope

The objective of the research is to understand fundamental processes in catalytic systems with applications to transportation technologies, such as those used for the treatment of NO_X emissions, and for the production of biomass-derived liquid fuels. The research heavily utilizes new capabilities and techniques for ultra-high resolution transmission electron microscopy with the HTML's aberration-corrected electron microscope (ACEM). The research is ultimately focused on understanding the effects of reaction conditions on the changes in morphology of heavy metal species on "real" catalyst support materials (e.g. oxides and carbon materials), and the understanding of the structures of model mono-, bi- and multi-metallic catalyst systems of known particle composition. A major thrust of these studies has been to develop methods of in-situ microscopy at elevated temperatures and under controlled gas compositions. This work has expanded with the collaboration with Protochips Inc. (Raleigh, NC), who provide a novel heating technology utilizing MEMS-based heating devices that we have shown to be stable enough to provide sub-Ångström imaging capabilities at high temperature in the ACEM. Model samples of nanoparticulates of controlled composition on carbon or oxide supports are also being studied in collaboration with the catalysis group at the University of Texas-Austin (Prof. P. Ferreira), the University of Texas-San Antonio (Prof. M. Jose-Yacaman), the University of Missouri-St. Louis (Prof. J. Liu), and University of New Mexico (Prof. A. Datye). Studies of the behavior of Pt species on oxide substrates are also being conducted with Drs. S. A. Bradley of UOP Co., and C. H. F. Peden of PNNL. NOx trap catalyst materials BaO/Al_2O_3 are being studied with Dr. Peden and Dr. Ja Hun Kwak at PNNL and Pt-Re/C catalysts on model carbon nanotube materials are being studies with Drs. Y. Wang and L. Zhang, also of PNNL. We have also initiated a new study of "intelligent catalysts" for automotive emission control applications, based on the self-regenerative phenomenon of heavy metal species such as Pd and Rh in Ca- and La-based perovskite crystal structures.

Technical Progress

This report highlights work this quarter on (1) development and characterization of MEMS-fabricated amorphous SiN layer on Protochips Aduro heater chips; and (2) use of the new double-tilt heating holder for precise orientation of catalyst supports.

MEMS-fabrication of Amorphous SiN films on Aduro™ Heater Chips

In order to achieve an environmental cell (E-cell) specimen holder for the JEOL 2200FS aberration-corrected electron microscope (ACEM) that is usable both for reducing and oxidizing environments, we have (with Protochips Co.) pursued the idea of MEMS-fabrication of thin SiN films during the heater chip production process. Heater chips from the initial production batch on which SiN layers were produced as the final microfabrication step were recently characterized. We had previously shown that we

could image at the atomic level with very little loss of resolution with the electron probe passing first through an amorphous SiN window prior to interacting with a catalyst material deposited directly on the underside of that window. It was expected that a similar SiN film could be deposited on the Aduro heater chips, but the first such films exhibited significant morphology, as shown in Fig. 1. This figure shows a high-angle annular dark-field (HA-ADF) image on the left, and the corresponding bright-field (BF) image on the right. Instead of a smooth, featureless film such as we have seen in past work using chips with large-area SiN "windows," the new films had a mottled structure as seen in Fig. 1, that looked like "Cheerios" on the surface, as seen at higher magnification in the HA-ADF and BF images of Fig. 2. The as-deposited SiN film was nominally 50nm thick, but this thickness is considered to be to great for the best imaging, so we had planned to use a standard etching technique employing concentrated HF, known to etch SiN at a specific rate (~10nm/min). We etched the new SiN layer to reduce the thickness to a nominal 25nm, and compared the etched film to the original, as shown in Fig. 3. While there was clearly a change in the appearance of the film, the "Cheerios" morphology still remained. Energy-dispersive x-ray analysis showed only Si and N in the film, so the structure was not due to any contaminant that resulted from the deposition process. The contrast in the HA-ADF image suggests that the Cheerios structures are protrusions that are thicker than the base thickness of the film. The HF etching process did not remove the Cheerios structure, but spaces between the Cheerios structures were clearly usable to test for the quality of the imaging process through the SiN layer.

Figure 4 shows a HA-ADF and BF image pair of the etched SiN film with a test catalyst sample (gold on iron oxide) deposited on the underside of the film. We imaged the lattice structure of the gold nanoparticles with the sample held at room temperature, and also with the sample heated to 600°C. The latter test is shown in Fig. 5, which confirmed that the as-deposited SiN film was very robust, as no cracks or tears were seen in any place on the heater chip during or after a heating procedure to 600°C. The image sequence in Fig. 5 shows a 65nm Au nanoparticle with part of the structure well oriented along a <110> crystallographic axis. This experiment shows the excellent imaging at the atomic level that can be achieved even with these less-than-ideal SiN films.

Results of tests of the behavior of the new Aduro chips with SiN layers deposited will be presented in the next quarterly. Also, work this quarter on a fully configured Gen 2 E-cell has led us to the decision to move to a modified, improved E-cell configuration, that we'll call the Gen 3 design; that new design will be detailed in a future quarterly.

Use of New Double-Tilt Heater Holder:

We have previously described the fabrication of a new specimen holder that permits both heating and a second axis of tilt to be possible. The "double-tilt" heater holder was initially fabricated to allow installation of original Aduro chips that are equiaxed and about 2.8mm in diameter. The holder was shown to allow heating to >1000°C at full ± tilts of 6°. The utility of the new holder is shown in the example of Fig. 6. Work with

Prof. Jimmy Liu of the University of Missouri-St. Louis involves studies of the behavior of platinum species on the surfaces of model ZnO support materials such as single-crystal nanobelts [1]. The original material had Pt species dispersed as single atoms and ultra-fine clusters on the surface of the ZnO nanobelt, but after heating in the microscope at a nominal 700°C for 30min, discrete Pt particles formed by coalescence mechanisms, and were epitatically oriented on the ZnO (11-20) surface. To show the epitaxy of Pt on ZnO, it was necessary to precisely orient the ZnO nanobelt so the electron beam was accurately positioned in the <11-20> zone axis orientation. The tilting process is easily observed on the ACEM's fast camera system, which shows the orientation by the appearance of a band structure related to the underlying crystal structure, when the electron beam is focused on the ZnO surface. In Fig. 6a, the band structure shows the position of the zone axis to be off the image, to the upper left corner, as suggested by the white dot at that position. An intermediate tilt position is shown in Fig. 6b, where the white dot in this image is cented at the zone axis position. The final, perfect tilt orientation is shown in Fig. 6c, this time with a black dot showing the zone axis orientation now symmetric with the electron beam direction. Figures 6d and 6e are, respectively, HA-ADF and BF images of the ZnO structure, showing the atomic columns of Zn in white contrast in Fig. 6d, and the higher atomic number Pt in higher bright contrast, indicating the Pt particles are epitactical with the ZnO crystal support. This process was facile to accomplish, and the tilting mechanism we have devised proved to be highly precise and extremely stable (e.g., no undue sample drift, or other sticking or jumping of the sample during tilting was noted).

References

1. J. Liu and L.F. Allard, "Imaging ZnO Nanobelts and Nanobelt-Supported Metal Nanocatalysts by Aberration-Corrected Scanning Transmission Electron Microscopy;" *Microsc Microanal* 15(Suppl 2), 1486-7, 2009

Status of Milestones

On schedule

Communications/Visits/Travel

None this quarter

Publications

1. L.F. Allard, M. Flytzani-Stephanopoulos and S.H. Overbury, " Behavior of Au Species in Au/Fe2O3 Catalysts Characterized by Novel *in situ* Heating Techniques and Aberration-Corrected STEM Imaging;" *Microscopy and Microanalysis*, in press (2010).

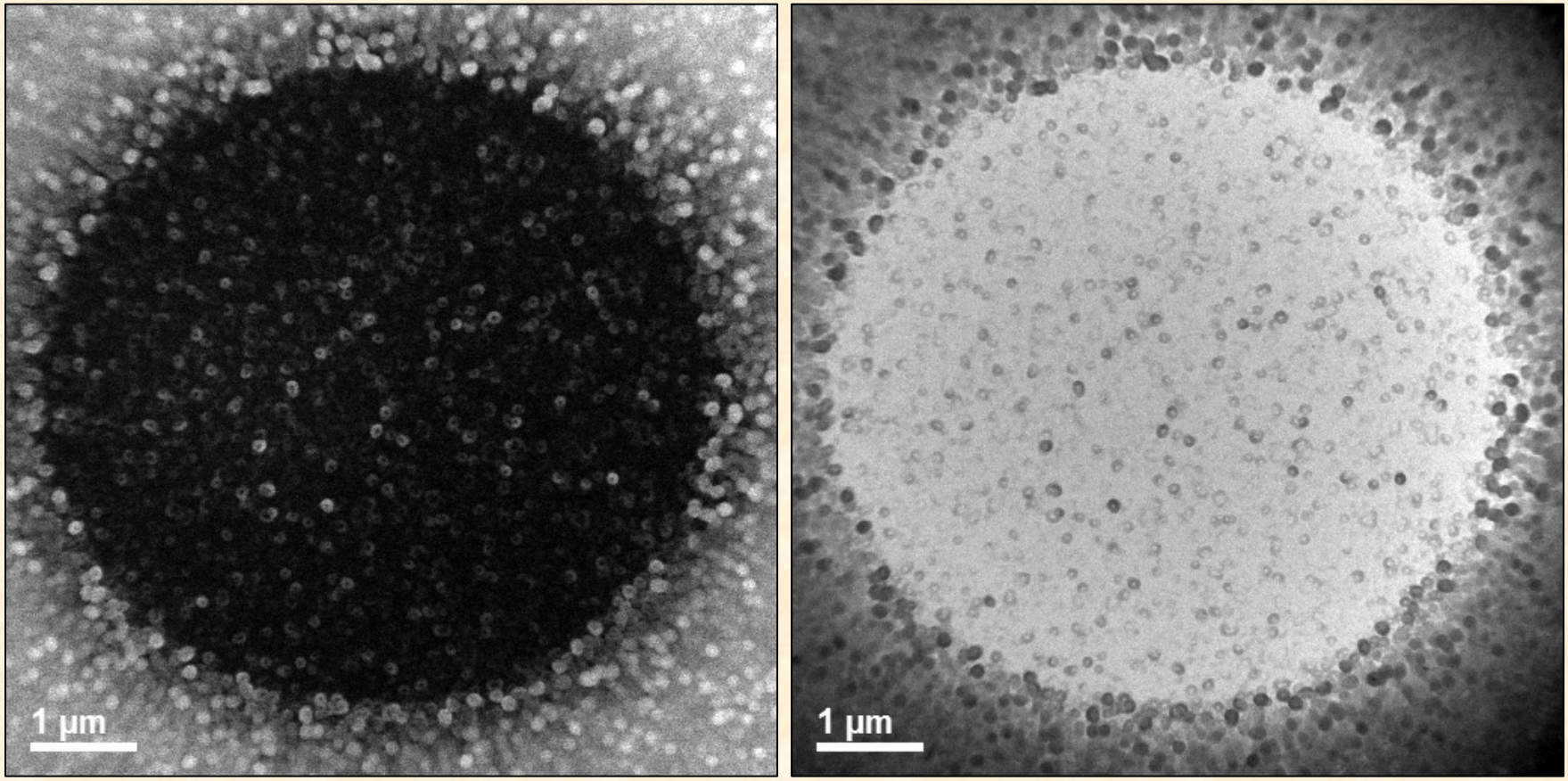

Heater membrane hole supporting 50 nm (nominal) SiN as-fabricated film. Note significant structure in film...?

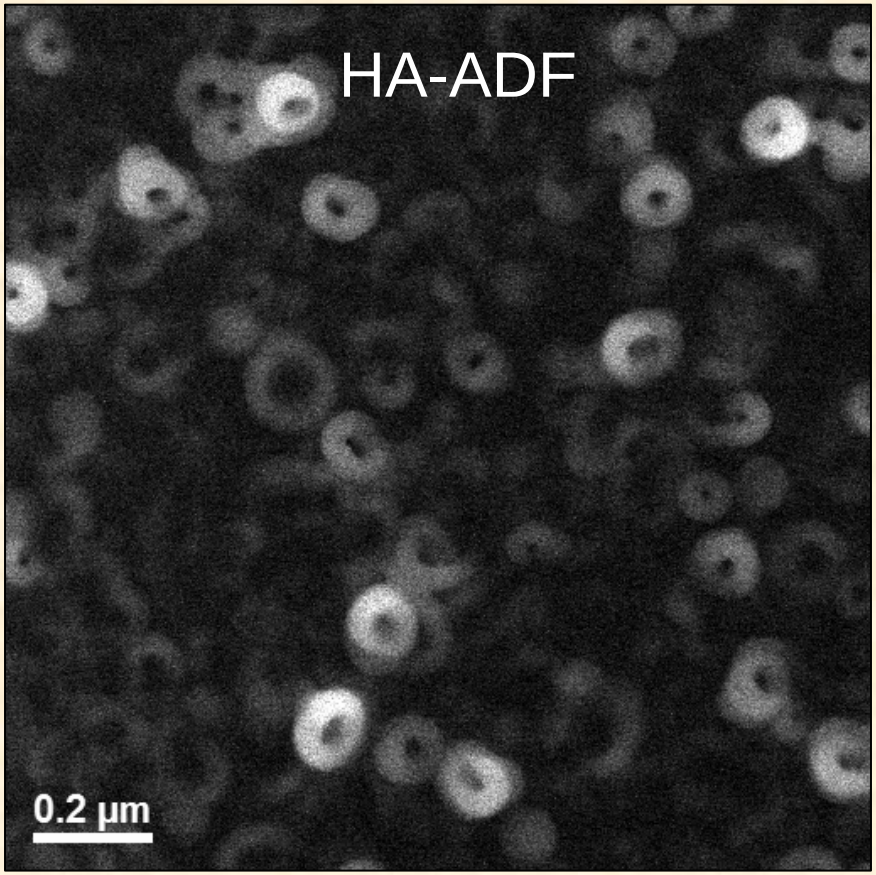

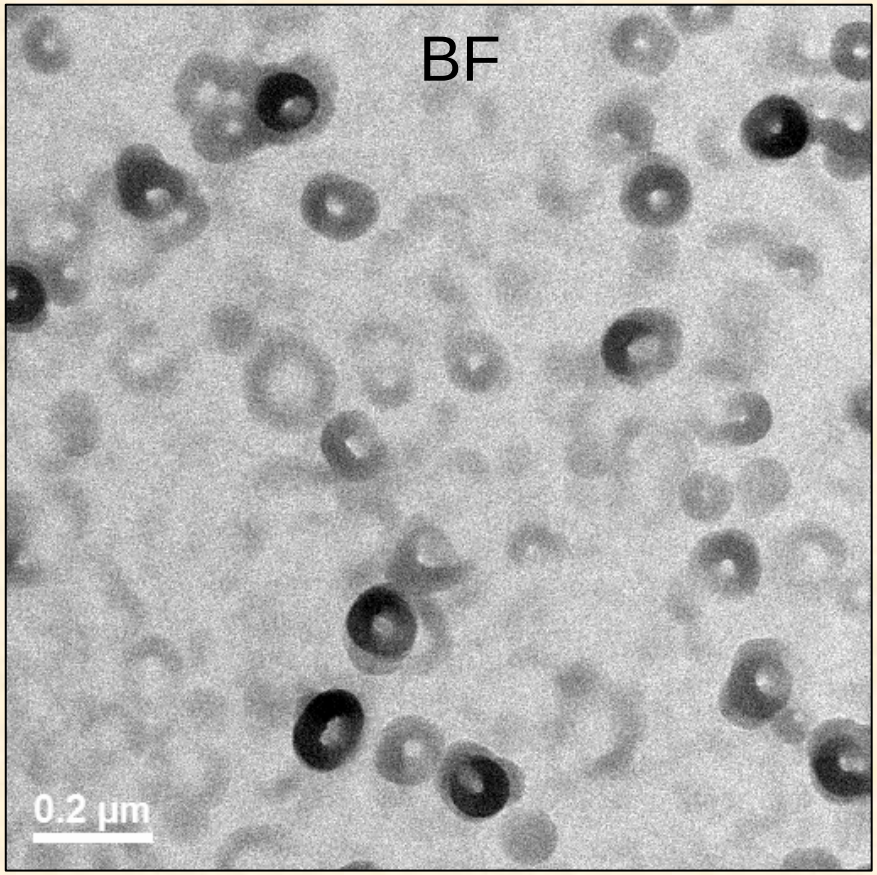

SiN film before etch; "Cheerios" on surface

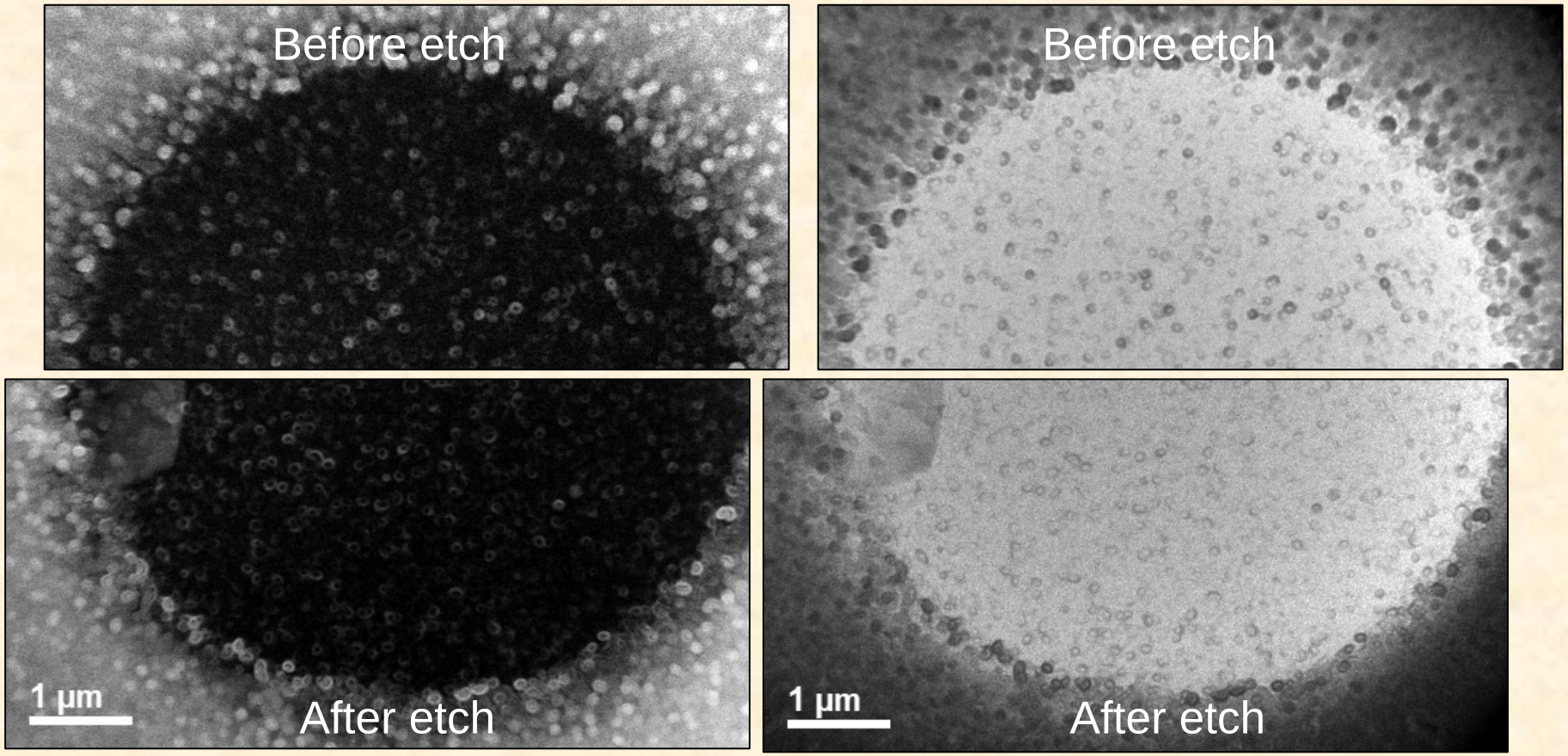

After etching in concentrated HF for 1 min, the SiN film was thinned to a nominal 25 nm thickness, and the "Cheerios" structure was somewhat reduced.

Fig. 3

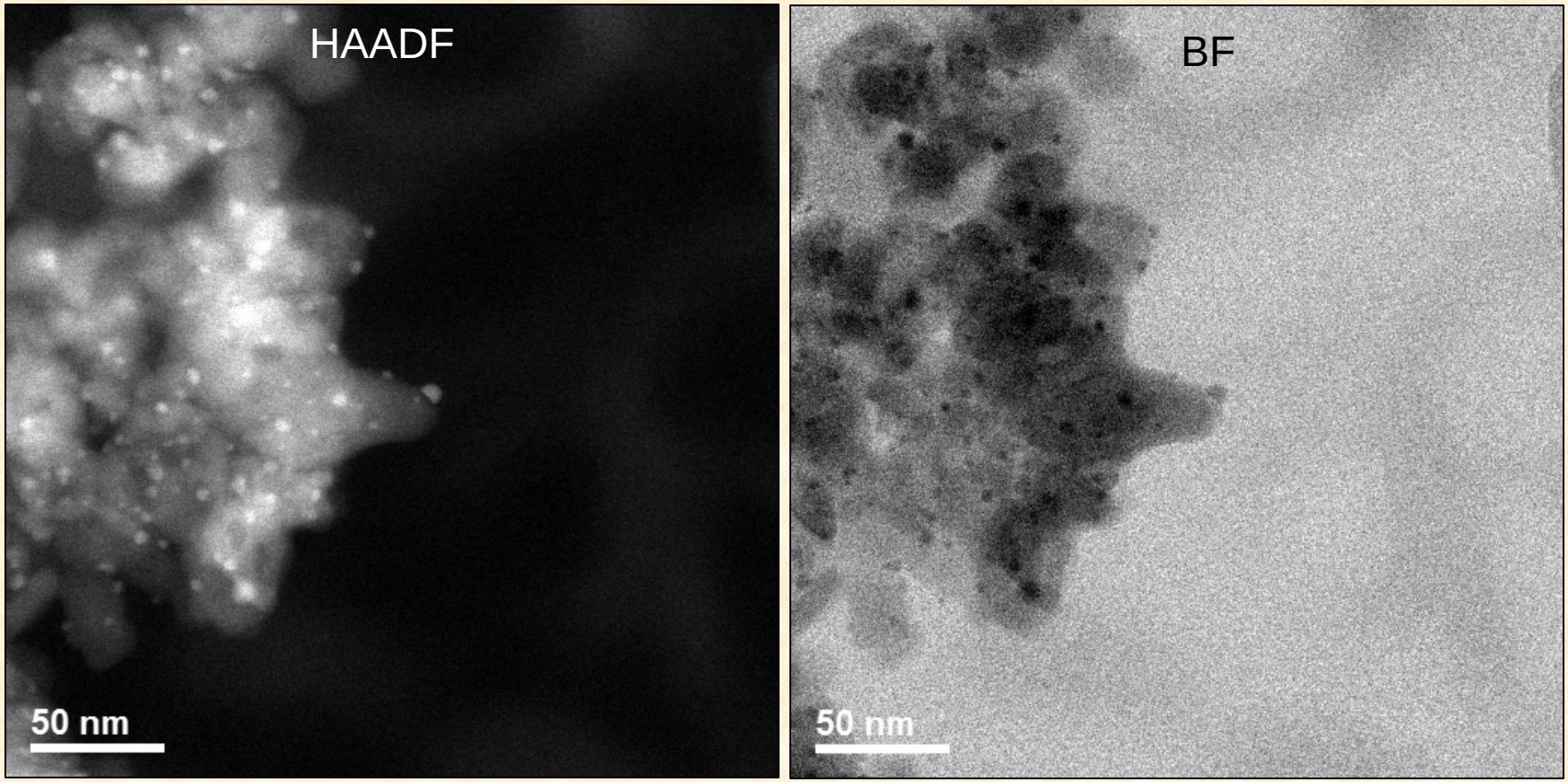

Imaging catalyst material (Au/FeOx) through the MEMS-fabricated SiN film on an Aduro heater chip.

Fig. 4

HAADF HAADF

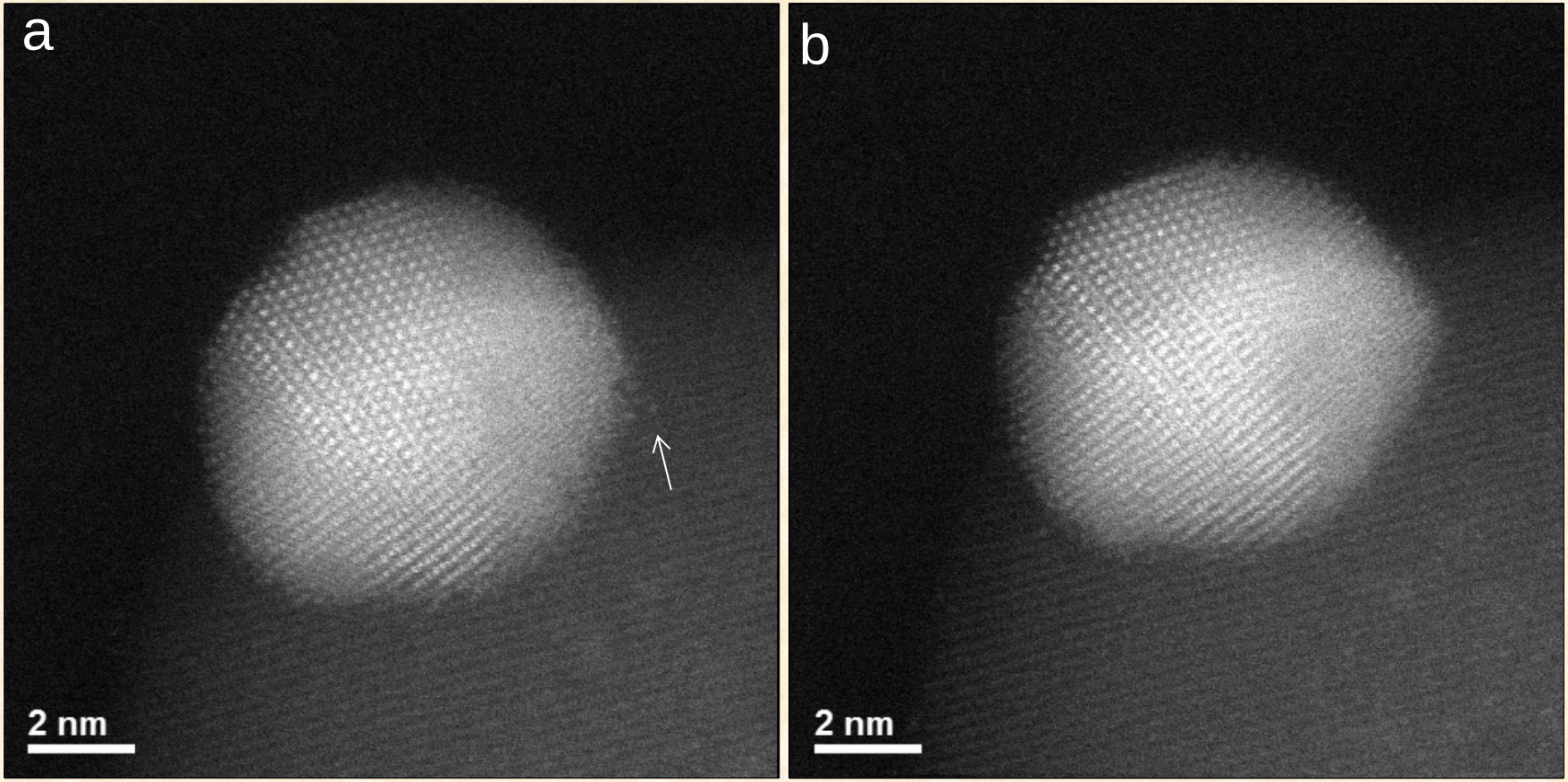

Imaging Au/FeOx catalyst thru ~25nm SiN film. Atomic columns and even single atoms (arrow) are clearly resolved through the SiN. In (a), the HA-ADF image was recorded at room temperature, after a 10-min-500°C heating treatment. In (b) the same Au nanoparticle is imaged at 500°C, showing the stability of the heater chip.

Fig. 5

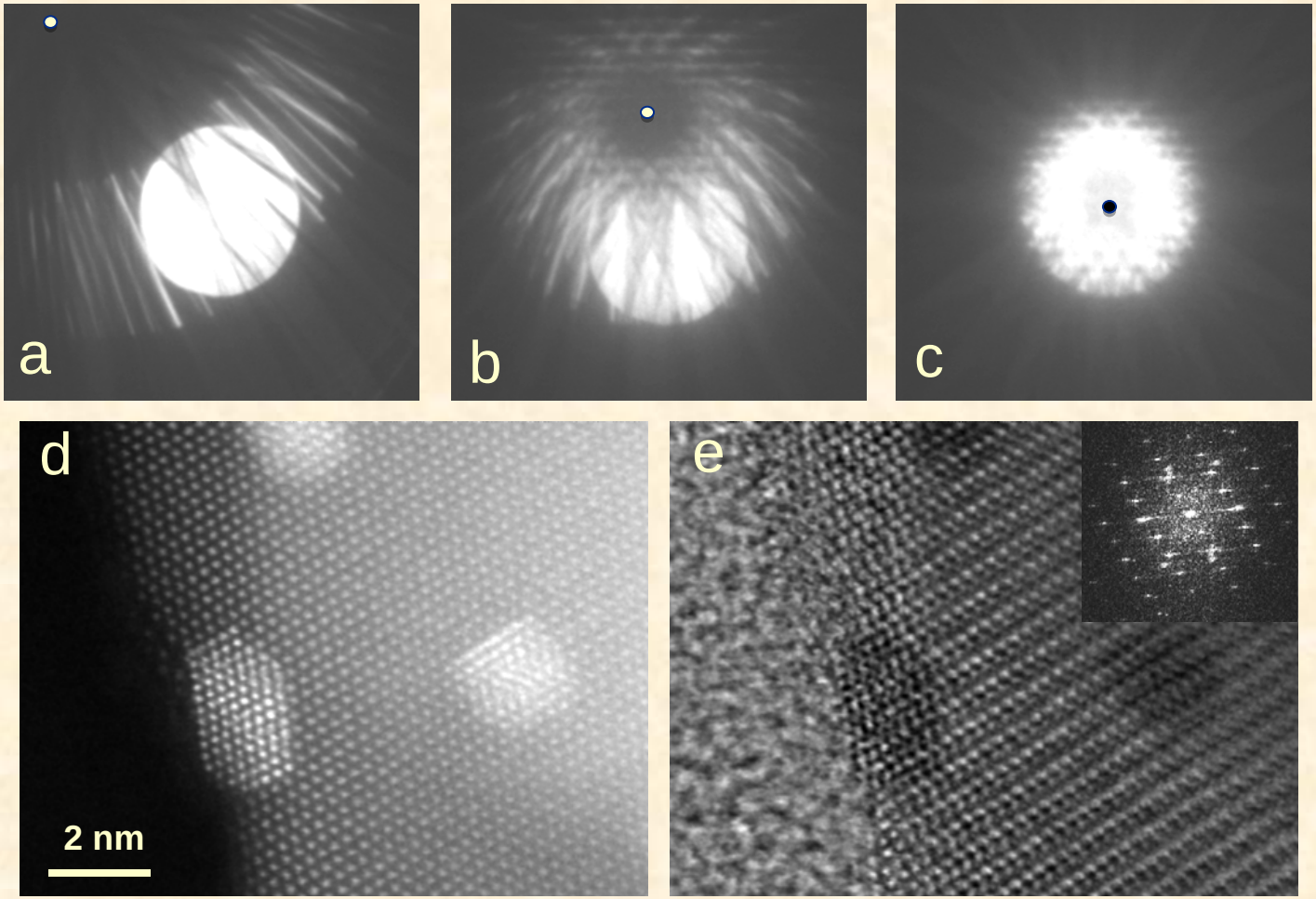

Example of the operation of the new double-tilt heater holder. Panels a, b and c show the band structure that is related to the crystallographic orientation of the ZnO single crystal "nanobelt" support material, with the white/black dots illustrating the gradual change in position during tilting to the final perfect orientation of (c). Panels d and e are, respectively, HA-ADF and BF images of Pt particles on the ZnO (11-20) crystal surface, showing epitaxy with the atomic columns of the ZnO crystal (after 700°C-30 min heating.

Agreement 14957: High Temperature Thermoelectrics

A. A. Wereszczak and H. Wang
Oak Ridge National Laboratory

R. McCarty and J. Sharp
Marlow Industries, Inc.

Objective/Scope

Measure needed thermomechanical and thermophysical properties of candidate thermoelectric (TE) materials and then use their data with established probabilistic reliability and design models to optimally design automotive and heavy vehicle TE modules. Thermoelectric materials under candidacy for use in TE modules tend to be brittle, weak, and have a high coefficient of thermal expansion (CTE); therefore, they can be quite susceptible to mechanical failure when subjected to operational thermal gradients. A successfully designed TE module will be the result of the combination of temperature-dependent thermoelastic property and strength distribution data and the use of the method of probabilistic design developed for structural ceramics.

Technical Highlights

Thermomechanical and thermophysical testing of Marlow-supplied materials continued throughout the FY10Q3.

Skutterudites:
Fast fracture (or inert) three-point bend fracture strength testing of n- and p-type skutterudites at 25, 200, 300, 400, and 500°C was completed. Slow rate testing (10x slower) at 400 and 500°C for both n- and p-types was completed too. About 100 n- and 100 p-type specimens were tested. No significant strength degradation was observed at those elevated temperatures for both the n- and p-type materials.

The mictrostructures on polished and fracture surfaces of n- and p-type skutterudite were examined and imaged with field-emission scanning electron microscopy.

Lead telluride (PbTe):
Fast fracture 450° three-point bend testing of n-type PbTe at 450°C was completed as was 300 and 450°C testing of p-type material.

High-temperature (HT) MAM bismuth telluride (Bi_2Te_3):
Fast fracture three-point bend testing of n-type HT MAM Bi_2Te_3 was completed at 80 and 225°C.

The mictrostructures on polished and fracture surfaces of p-type HT MAM Bi_2Te_3 were examined and imaged with field-emission scanning electron microscopy.

Bridgeman Bi_2Te_3:
Hundreds of Bridgeman specimens were received from Marlow for both thermoelectric, thermoelectric, and mechanical testing. Both n- and p-type materials were received. Specimens were also harvested out of the processed billets, and several properties will also be measured to determine if any positional dependencies exist.

Status of FY 2010 Milestones

1. Generate thermoelastic and mechanical property database as a function of temperature on candidate p- and n-type TEMats fabricated by Marlow Industries as part of CRADA. **(09/10)** *On schedule*.
2. Develop in-situ thermal-gradient-strength test method for TEMats. **(09/10)** *On schedule.*

Communications/Visits/Travel

Wereszczak and Wang visited Marlow (Dallas, TX) on 20 Apr 2010 for a semiannual CRADA review. A conference call was also held on 18 June 2010 with Marlow engineers and scientists.

Problems Encountered

None.

Publications/Presentations/Awards

A. A. Wereszczak, M. E. Ragan, K. T. Strong, Jr., P. J. Ritt, H. Wang, J. R. Salvador, and J. Yang, Strength of N- and P-Type Skutterudites," to appear in Vol. 31, *Ceramic Engineering and Science Proceedings*, 2010.

References

None.

Agreement 16308: MBD Thermoelectrics Theory and Structure

David J. Singh
Oak Ridge National Laboratory

Objective/Scope

We will use modern science based materials design strategies to find ways to optimize existing thermoelectric materials and to discover new families of high performance thermoelectrics for waste heat recovery applications in vehicles. The emphasis will be on the thermoelectric figure of merit at temperatures relevant to waste heat recovery and on other properties important for applications, especially anisotropy, cost, and mechanical properties.

Technical Highlights

Vehicular applications of thermoelectric materials for waste heat recovery will be greatly facilitated by the identification of high performance materials that have low cost and are available in large quantities. One class of materials that shows great promise are filled skutterudites. The first such material was $La(Fe,Co)_4Sb_{12}$. This is a Zintl-type compound. More recently higher performance has been found by replacing La by mixtures of rare earth elements, or rare earth elements plus Ba, particularly in n-type material. These materials derive their performance from the combination of low lattice thermal conductivity due to the rare earth filler and a favorable electronic structure that has multiple heavy conduction bands. [1] In the second quarter we performed electronic structure calculations that indicated that the chemical range where high performance can be achieved is larger than previously thought and identified alkaline earth (*Ae*) filled skutterudites containing Ni and Fe instead of Co as promising. During the present quarter we continued this work by doing transport calculations (Fig. 1) to test whether this is in fact the case and to make quantitative predictions for the thermopower.

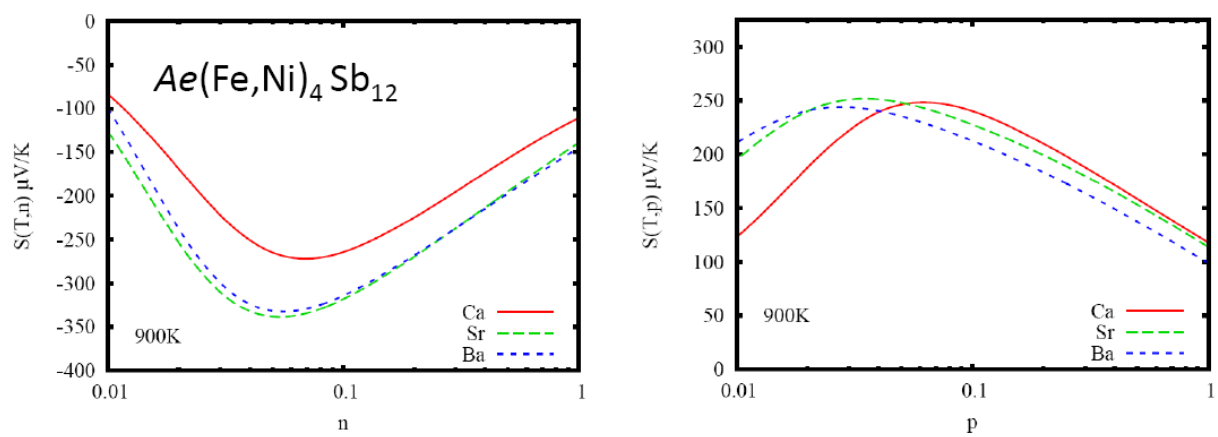

Fig. 1: Calculated *n*-type (left) and *p*-type (right) thermopowers for Fe,Ni based skutterudites at 900 K. Note the high thermopowers for both carrier types at doping levels in the range 0.05-0.1 per formula unit.

We also performed calculations of the full vibrational spectrum of these compounds using supercells. Results for Ca and Ba are shown in Fig. 2. The results support our

previous conjecture about the effect of the alkaline earth filler on the phonon spectrum as related to thermal conductivity.

The importance of this is (1) alkaline earths are cheap and available as compared to rare earths and (2) Ni is substantially cheaper than Co, and furthermore only half as much of this element is needed to achieve the correct electron count as compared to Co (Co has one less valence electron than Ni). This allows the use of material with more Fe, which is a very inexpensive material. Based on the promising results obtained, we filed an invention disclosure covering thermoelectric application of these compositions. We are currently finalizing a technical report based on these results.

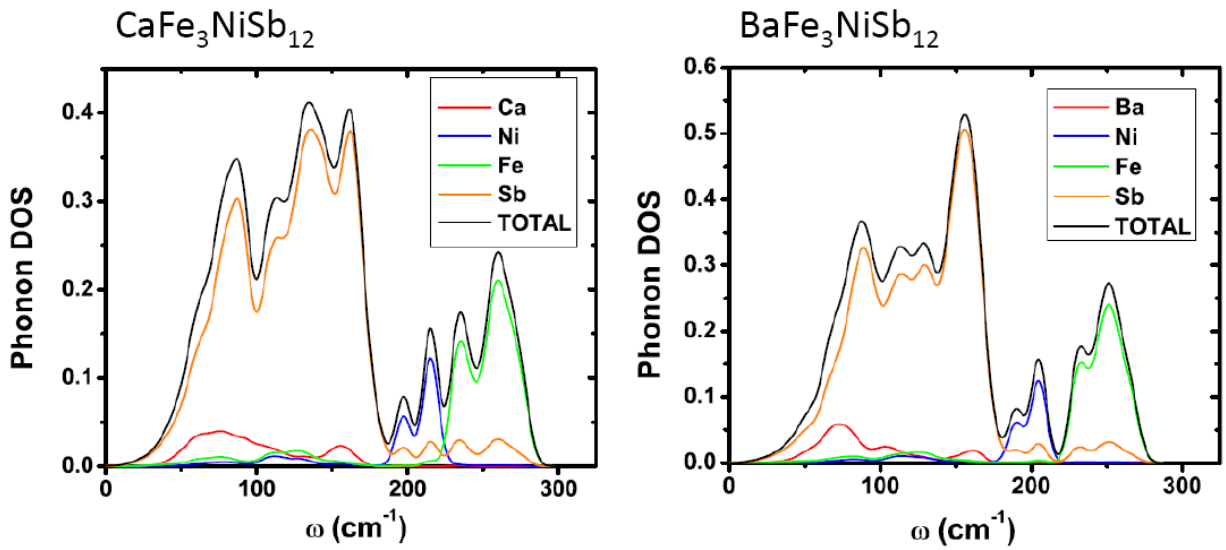

Fig. 2: Phonon densities of states for $CaFe_3NiSb_{12}$ and $BaFe_3NiSb_{12}$. Note the alkaline earth modes between 50 and 100 cm^{-1}, where they mix with heat carrying Sb phonons.

Skutterudites offer a number of advantages for automotive applications, particularly high performance and potentially low cost. Nonetheless, they are new materials and are less proven than PbTe and related chalcogenides. As such, even though Pb is undesirable in automotive applications and Te containing materials are potentially costly, there is automotive industry interest in PbTe, particularly new high performance versions of PbTe. These are the so-called “LAST” compounds (PbTe alloyed with $AgSbTe_2$) and PbTe:Tl (PbTe doped by approximately 1% Tl). PbTe:Tl is p-type with *ZT* values of approximately 1.3 but suffers from the major disadvantage of containing Tl, which is a highly toxic element. We investigated this material with first principles calculations, initially phonon calculations for PbTe in FY08 following a request from General Motors. This quarter we completed a series of transport calculations based on Boltzmann theory and the first principles relativistic electronic structure [2-3]. We found a rather unexpected result. In particular, we found that Tl is not essential for the high performance of PbTe:Tl but that other doping strategies could be used provided that sufficiently high carrier concentration could be obtained. A technical report on this was prepared and published [4] and these results were communicated at two meetings. The result was very recently confirmed experimentally by a group at Northwestern University [J. Androulakis, et al., preprint arXiv:1007.1637, dated July 9, 2010], who showed

ZT=1.3 at 700K in a sample of PbTe doped with Na and K. This shows that high *ZT* can be achieved in a thermodynamically stable doped PbTe without Tl. We plan to investigate some other simple chalcogenides without Pb and Te to determine whether this result applies strictly to PbTe or if it holds in a broader class of related compounds.

Status of FY 2010 Milestones

We are progressing towards our milestone of predicting new thermoelectric compositions. Strategies that will be used are to continue investigation of Cu containing materials, narrow band oxide materials, skutterudites and chalcogenides. The plans for Q4 are detailed investigation of skutterudite compositions related to those discussed above to provide theoretical guidance for optimization of carrier concentrations and filling fraction and investigation of Bi-Cu chalcogenides, since these are potentially very inexpensive thermoelectric materials. Depending on the results we will continue with those materials and/or investigate alternate narrow band oxides containing mixed-valent transition element ions and Zintl-phase materials.

Communications/Visits/Travel

D.J. Singh attended a workshop on Thermoelectric Transport Fundamentals in Hangzhou, China and gave an invited oral presentation. D. Parker attended the International Conference on Thermoelectrics in Shanghai, China. D.J. Singh and D. Parker attended the Annual Merit Review Meeting in Washington.

Problems Encountered

No significant problems encountered this quarter.

Publications/Presentations/Awards

D.J. Singh gave an invited talk, “Recent Theoretical Results on Thermoelectric Materials” at the workshop on “Thermoelectric Transport Fundamentals” in Hangzhou, China.

Refereed Papers:

N. Bernstein, J.L. Feldman and D.J. Singh, “Calculations of dynamical properties of skutterudites: Thermal conductivity, thermal expansivity and mean-square displacement”, Physical Review B **81**, 134301 (2010).

L. Zhang and D.J. Singh, “Electronic structure and thermoelectric properties: $PbBi_2Te_4$ and related intergrowth compounds”, Physical Review B **81**, 245119 (2010).

D.J. Singh, “Doping-dependent thermopower of PbTe from Boltzmann transport calculations”, Physical Review B **81**, 195217 (2010).

References

1. D.J. Singh, “Theoretical and Computational Approaches for Identifying and Optimizing Novel Thermoelectric Materials”, in “Semiconductors and Semimetals, Vol. 70: Thermoelectric Materials Research”, p. 125 (Academic Press, New York, 2000).
2. D.J. Singh and L. Nordstrom, Planewaves, “Pseudopotentials and the LAPW Method, 2nd Edition”, Springer, Berlin, 2006.

3. G.K.H. Madsen and D.J. Singh, “BoltzTraP: A code for calculating band-structure dependent quantities”, Computer Physics Commun. **175**, 67 (2006).
4. D.J. Singh, “Doping-dependent thermopower of PbTe from Boltzmann transport calculations”, Physical Review B **81**, 195217 (2010).

Agreement 17859: Durability of ACERT Engine Components

Hua-Tay Lin, T. Kirkland, and B. Armstrong
Oak Ridge National Laboratory

Mark Veliz and J. Jenson
Caterpillar, Inc.

Objective/Scope

There are four primary goals of this research agreement, which contribute toward successful design and implementation of advanced lightweight material components to achieve high-efficiency engine of 55% of heavy-duty diesel engines by 2018 as set under the 21st CT program: 1) the generation of a mechanical engineering database of candidate advanced lightweight materials before and after exposure to simulated engine environments; 2) the microstructural evolution and accompanied chemical changes during service in these advanced materials; 3) material selection, development, and design of complex-shaped components, and 4) application and verification of probabilistic life prediction methodology for advanced high-efficiency diesel engine components. The methodology implemented would also help to manufacture consistent mechanical reliability and performance of complex shaped components.

Technical Highlights

Technical conference call meeting was held among the CRADA participants (Caterpillar, ANL, and ORNL) to discuss the critical materials and components for property evaluation and engine testing. It is proposed that an exhaust manifold made from ferritic stainless steel and a set of intake and exhaust valves made from advanced alloys developed by ORNL would be installed for current Tier 2 ACERT engine testing. The set of valves have passed the bench rig test at Caterpillar and would be ready for engine evaluation at NTRC ORNL. On the other hand the exhaust manifold would be casted and fabricated by the material supplier. Thus, engine testing of advanced alloy valves would be initiated first and then followed by exhaust manifold evaluation.

Study of Al-oxide based environmental barrier coating (EBC) developed for the ductile ferritic Fe-steel substrate was continued in this quarterly reporting period. The goal of this EBC developmental study is to provide an alternative approach for an effective protection for the current production ferritic Fe-steel used for exhaust components in heavy-duty diesel (HDD) engine. The application of EBC would allow HDD OEMs to significantly reduce the heat rejection (and thus thermal stress generated) and also prevent the oxidation/corrosion-induced degradation process encountered in the current production materials. Consequently, it would allow the OEMs to avoid the use of the very high-cost stainless steel materials for the exhaust port and manifold components that could potentially lead up to USD $5M cost saving per year. More importantly this is one of the key enabling materials technologies that would allow end users to achieve 55% HDD engine efficiency and life greater than 1 million miles by 2018 as set under the 21st Century Truck Program.

Colloidal processing offers a low cost alternative processing technology for producing uniform coatings on complex-shaped components via a simple dip coating process (i.e.,

the ORNL slurry coating process) (1-2). Also, the oxide-based coating could be processed at lower temperature with much shorter times, thus preventing the interaction (chemical reaction) between the coating and Fe-based substrate. Control of the rheological behavior of the suspension by tailoring interparticle (or surface) forces is paramount to achieve a high quality and defect free coating. In aqueous-based suspensions long-range attractive van der Waals forces must be balanced by repulsive forces to tailor the desired degree of suspension stability. Typically, ionizable polymeric dispersants, or polyelectrolytes, are used to modify the surface of particles to impart repulsive electrosteric forces (3-4). Aluminum, (H10, Valimet Inc., Stockton, CA) was used as the metal powder in this study. The aluminum powder had an average particle size of ~ 13.19 μm and surface area of 0.4475 m2/g, determined using dynamic light scattering (Horiba, Inc., Kyoto, Japan) and B.E.T. (Autosorb-1, Quantachrome Instruments, Boynton Beach, FL), respectively. Polyacrylic acid (PAA, 450kg/mol, Aldrich Chemicals, Milwaukee, WI), an anionic polyelectrolyte, was used as the dispersant and PL001 (Polymer Innovations, Inc., Vista, CA) as the rheological modifier for the Al system. Water purity was measured using inductively coupled plasma mass spectroscopy (ICPMS, X Series 2, Thermo Fisher Scientific, Inc., Waltham, MA). The standards (QCS26, High Purity Standards, Charleston, SC) and the nitric acid matrix (Ultrex Pure, J.T. Baker, Phillipsburg, NJ) were used to calibrate the ICPMS. The Al-oxide based coating was employed via a dip or slurry based process. A post heat treatment at 750°C for 2 hrs in argon was carried out to covert the slurry coating into the oxide based coating.

A 500h thermal cycle between 300° and 760°C in air was carried out to evaluate the stability and durability of Al-based oxide coating during this reporting period. Figure 1 shows the polished cross section of Al-oxide based layer on the ferritic Fe steel alloy substrate after thermal cycle testing. The detailed SEM observations show that a very thin, but dense and coherent Al-oxide layer (~ 1 μm thick) formed on the surface, as confirmed by the EDAX elements map shown in Fig. 2. It is not clear why the Al-oxide coating became very thin after the thermal cycle testing. There is a very porous Al-oxide layer, which might be the remnants after the coating conversion, above the dense layer. In addition, there is also a dense layer with Al, Fe and Si elements underneath the thin Al-oxide layer, which could be a reaction product from the Fe steel substrate enriched with Si, formed after the heat and thermal cycle process (Fig. 1). Further studies of the heat treatment conditions (i.e., temperature and time) will be continued to determine an optimized window for an effective and durable protective coating layer for hot section components of HDD engines. On the other hand, the dense Al-oxide layer was not always observed in some regions of substrate and only the oxide layer with Fe-Al-Si was detected, as shown in Fig. 3. More thermal cycle testing needs to be carried out to confirm the observations and determine the oxide layer formation mechanisms.

Status of FY 2010 Milestones

Complete testing and analysis of a prototype ACERT exhaust component with advanced thermal barrier coating. **(09/10**) – On schedule.

Communications/Visits/Travel.
Conference calls with Dr. Mark Veliz of Caterpillar and Dr. JG Sun of ANL to discuss the potential ACERT engine components for property characterization and NDE.

Communications with Dr. Mike Kass at ORNL NTRC regarding the up-to-date status on verification test run of C15 ACERT engine.

Attend and present a poster at the 2010 DOE Merit Review, June 7-11, Washington D.C.

Problems Encountered
None.

Publications/Presentations/Awards
1. H. T. Lin, "Durability of ACERT Engine Components," poster presented at the 2010 DOE Merit Review, June 7-11, Washington D.C.

References
1. Armstrong, B., Kirby, G., Cooley, K., *Proceedings of The 29th International Technical Conference on Coal Utilization & Fuel Systems*, Clearwater, FL (2004).
2. Kirby, G., Cooley, K., and Armstrong, B., *Proceedings of GT2005 ASME Turbo Expo 2005: Power for Land, Sea, and Air*, Reno-Tahoe, NV (2005).
3. Cesarano, J. and Aksay, I., *J. Am. Ceram. Soc.*, 71 (4) 250-55 (1988).
4. Cesarano, J. and Aksay, I., *J. Am. Ceram. Soc.*, 71 (12) 1062-67 (1988).

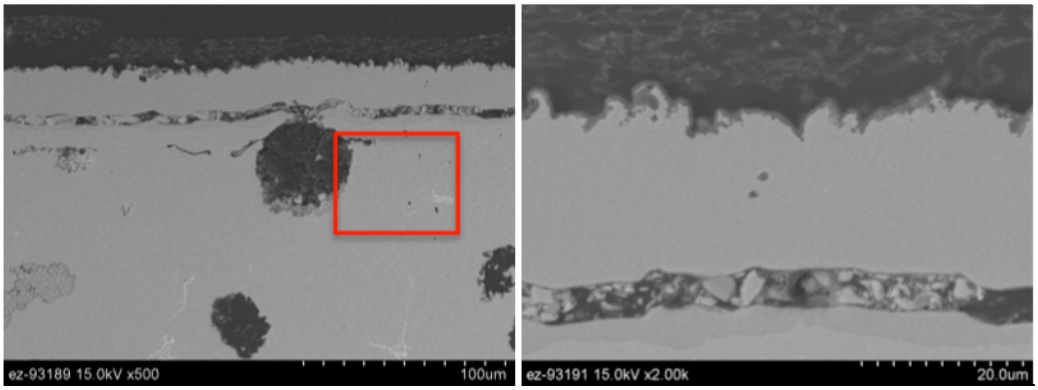

Figure 1. SEM micrographs showed the Al-oxide based coating processed via the low-cost aqueous processing method after the 500h thermal cycles between 300° and 760°C in air.

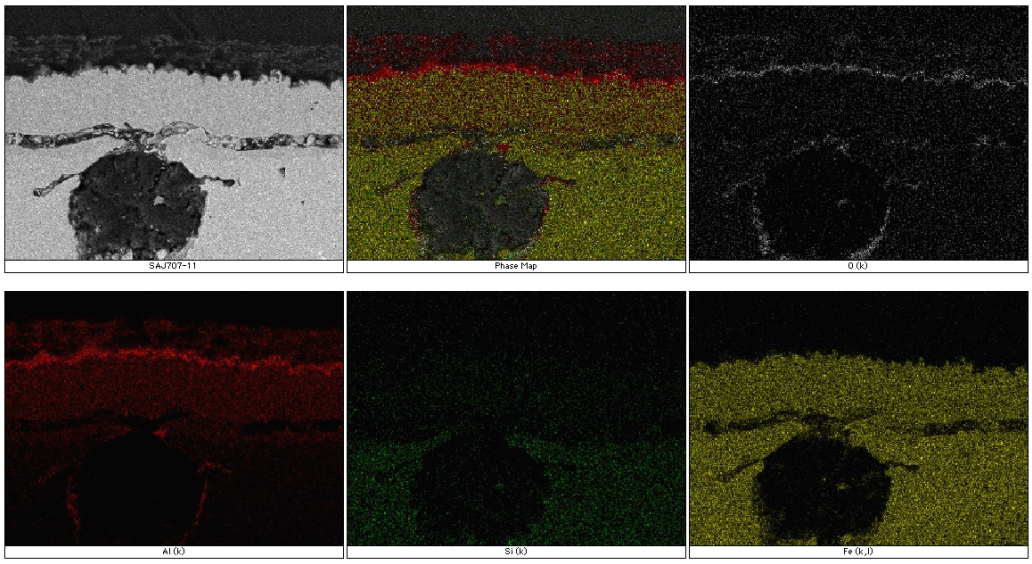

Figure 2. EDAX maps show the details of elements and distribution in the reaction and reaction surface layer on the ferritic Fe-steel substrate.

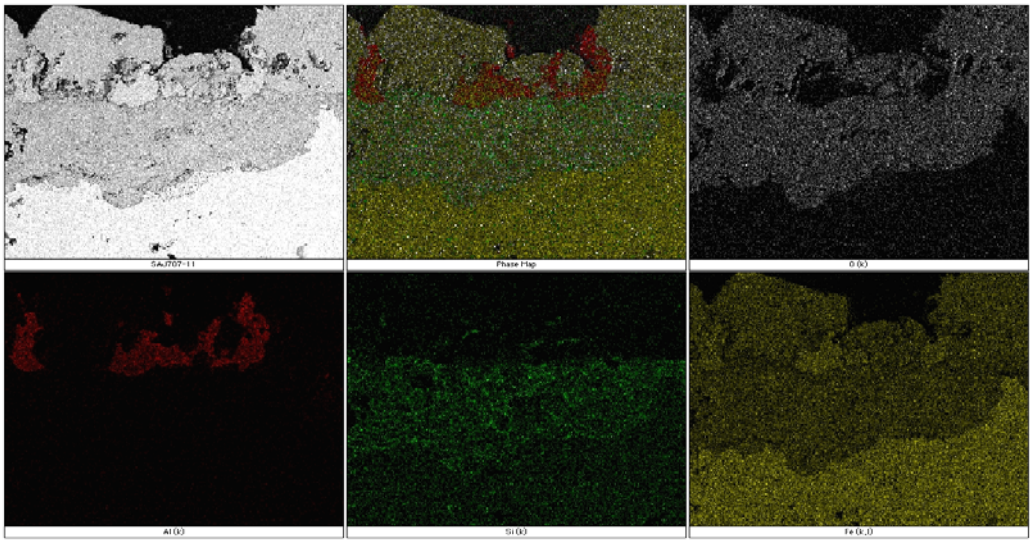

Figure 3. EDAX maps show the details of elements and distribution in the reaction and reaction surface layer on the ferritic Fe-steel substrate. The layer did not exhibit a dense Al-oxide layer.

Agreement 20370: Life Cycle Modeling of Propulsion Materials

Sujit Das
Oak Ridge National Laboratory

Objective/Scope

Perform a life cycle assessment of alternative lightweight light-duty engine designs for vehicle weight reduction and improved fuel economy. In addition, a life cycle energy analysis of CF8C+ cast austenitic stainless steel will be undertaken.

Technical Highlights

The life cycle assessment of alternative lightweight light-duty engine designs for vehicle weight reduction and improved fuel economy will be based on two alternative lightweight designs, comparing with the baseline Ford Duratec 3.0L, V6, 4-V, DOHC, d-VVY, NA, PFI engine with a power rating of 225 hp used in the recent light-duty technology cost analysis EPA study by FEV, Inc. A downsized 2.0L, I4, 4-V, DOHC, d-VVT, Turbo, GDI having the same power will be considered as one of the lightweight engine design options, whereas the other option includes the use of lightweight engine material. Magnesium will be considered as the lightweight engine replacement material for major engine components such as cylinder block, cylinder head, cylinder liner, structural oil pan, and front engine cover etc. compared to aluminum used for those parts in the baseline engine. The lightweight engine material data is based on the USAMP Magnesium Powertrain Cast Components project and the use of magnesium alloy based engine in some current BMW vehicle models. For the downsized engine, ten major components based on its relative weight and cost contributions to the overall engine were identified, compared to eight major components for the lightweight material engine and those will only be addressed in the life cycle analysis. Total engine weight difference between the baseline and the downsized engine is estimated to be 64 lbs, compared to only 26 lbs for the lightweight material engine. Life cycle engine data collection has been completed and fuel economy estimates for various lightweight engine options have been estimated based on a combination of previously published research, available data suitability of various engine types to appropriate vehicle classes, and expert opinions. The comparative life cycle analysis of alternative light-duty engine designs is currently in progress using the commercial LCA software SimaPro.

The life cycle energy analysis of CF8C+ cast austenitic stainless steel in automotive applications was initiated. Three potential market areas, i.e., automotive turbochargers and exhaust manifolds, gas turbines, and coal-fired power generation plants would be the analysis focus. Energy benefits estimates will be based not only on material production but also based on expected energy efficiency gained during the projected future material use.

Future Plans

Complete the life cycle assessment of alternative lightweight light-duty engine designs. A draft report will be submitted summarizing the results of the life cycle analysis before the end of Aug.'10. The other task on the life cycle energy analysis of CF8C+ cast

austenitic stainless steel in automotive applications will be completed by the end of Sept.'10.

Status of FY 2010 Milestones
On schedule.

Communications/Visits/Travel
Several communication exchanges were made with Greg Kolwich of FEV, Inc. in finalizing the composition and weights of baseline and downsized engines. Projected fuel efficiency data on the use of CF8C+ in turbochargers was obtained from Gerry LaRue of Honeywell, Inc.

Problems Encountered
None

Publications/Presentations
"Life Cycle Modeling of Propulsion Materials" – a poster presentation was made at the DOE Annual Merit Review Meeting held on June 10, '10, in Washington, DC.

References
None